2017

# Hydrologic controls on the natural drainage networks extracted from high-resolution topographic data

Milad Hooshyar
*University of Central Florida*

# HYDROLOGIC CONTROLS ON THE NATURAL DRAINAGE NETWORKS EXTRACTED FROM HIGH-RESOLUTION TOPOGRAPHIC DATA

by

MILAD HOOSHYAR
B.S Isfahan University of Technology, 2008
M.Sc Amrikabir University of Technology, 2011

A dissertation submitted in partial fulfillment of the requirements
for the degree of Doctor of Philosophy
in the Department of Civil, Environmental and Construction Engineering
in the College of Engineering and Computer Science
at the University of Central Florida
Orlando, Florida

Spring Term
2017

Major Professor: Dingbao Wang and Stephen C. Medeiros

# ABSTRACT

Drainage networks are important geomorphologic and hydrologic features which significantly control runoff generation. Drainage networks are composed of unchannelized valleys and channels. At valley heads, flow changes from unconfined sheet flow on the hillslope to confined flow in valley. Localized confined flow dominates in valleys as a result of convergent topography with positive curvature. Channels initiate at some distance down from the valley head, and the transition from unchannelized valley to channel is referred to as the channel head. Channel heads occur at a point where fluvial transport dominates over diffusive transport.

From the hydrologic perspective, channels are categorized as perennial, intermittent, and ephemeral streams based on the flow durations. Perennial streams flow for the most of the time during normal years and are maintained by groundwater discharge. Intermittent (i.e. seasonal) streams flow during certain times of the year receiving water from surface sources such as melting snow or from groundwater. Lastly, ephemeral streams flow only in direct response to precipitation without continuous surface flow.

In this dissertation, the hydrologic controls on the drainage networks extracted from high resolution Digital Elevation Models (DEMs) based on Light Detection and Ranging (LiDAR) are investigated. A method for automatic extraction of valley and channel networks from high-resolution DEMs is presented. This method utilizes both positive (i.e., convergent topography) and negative (i.e., divergent topography) curvature to delineate the valley

network. The valley and ridge skeletons are extracted using the pixels' curvature and the local terrain conditions. The valley network is generated by checking the terrain for the existence of at least one ridge between two intersecting valleys. The transition from unchannelized to channelized sections (i.e., channel head) in each 1st-order valley tributary is identified independently by categorizing the corresponding contours using an unsupervised approach based on K-means clustering. The method does not require a spatially constant channel initiation threshold (e.g., curvature or contributing area). Moreover, instead of a point attribute (e.g., curvature), the proposed clustering method utilizes the shape of contours, which reflects the entire cross-sectional profile including possible banks. The method was applied to three catchments: Indian Creek and Mid Bailey Run in Ohio, and Feather River in California. The accuracy of channel head extraction from the proposed method is comparable to state-of-the-art channel extraction methods.

Valleys extracted from DEMs may be wet (flowing) or dry at any given time depending on the hydrologic conditions. The temporal dynamics of flowing streams are vitally important for understanding hydrologic processes including surface water and groundwater interaction and hydrograph recession. However, observations of wet channel networks are limited, especially in headwater catchments. Near infrared LiDAR data provide an opportunity to map wet channel networks owing to the fine spatial resolution and strong absorption of light energy by water surfaces. A systematic method is developed to map wet channel networks by integrating elevation and signal intensity of ground returns. The signal intensity thresholds for identifying wet pixels are extracted from frequency distributions of intensity return within the convergent topography extent using a Gaussian mixture model.

Moreover, the concept of edge in digital image processing, defined based on the intensity gradient, is utilized to enhance detection of small wet channels. The developed method was applied to the Lake Tahoe area based on eight LiDAR acquisitions during recession periods in five watersheds. A power-law relationship between streamflow and wetted channel length during recession periods was derived, and the scaling exponent ($L \propto Q^{0.38}$) is within the range of reported values from fieldwork in other regions.

Several studies in the past focused on the relationship between drainage density (i.e., drainage length divided by drainage area) and long-term climate and reported a U-shape pattern. In this dissertation, this relationship was re-visited and the effect of drainage area on drainage density was investigated. Long-term climate was quantified by climate aridity indices which is the ratio between long-term potential evaporation and precipitation. 120 study sites across the United States with minimal human disturbance and a wide range of climate aridity index were selected based on the availability of LiDAR data. The drainage networks were delineated from LiDAR-based 1 m DEMs using the proposed curvature-based method. Despite the U-shaped relationship in the literature, our result shows a significant decreasing trend in the drainage density versus climate aridity index in arid regions; whereas no trend is observed in humid watersheds. This observation and its discrepancy with the reported pattern in the literature are justified considering the dynamics of the runoff erosive force and the resistance of vegetation and the climate controls on them. Our findings suggest that natural drainage networks in arid regions are more sensitive to the change in long-term climate conditions compared with drainage networks in humid climate. It was also found that drainage density has a decreasing trend with drainage area in arid

regions; however, no trend was observed in humid regions. In a broader sense, the findings influence our understanding of the formation of drainage networks and the response of hydrologic systems to climate change.

The formation and growth of river channels and their network evolution are governed by the erosional and depositional processes operating on the landscape due to movement of water. The branching angles, i.e., the angle between two adjoining channels, in drainage networks are important features related to the network topology and contain valuable information about the forming mechanisms of the landscape. Based on channel networks extracted from 1 m Digital Elevation Models of 120 catchments with minimal human impacts across the United States, we showed that the junction angles have two distinct modes with $\overline{\alpha_1} \approx 49.5°$ and $\overline{\alpha_2} \approx 75.0°$. The observed angles are physically explained as the optimal angles that result in minimum energy dissipation and are linked to the exponent characterizing slope-area curve. Our findings suggest that the flow regimes, debris-flow dominated or fluvial, have distinct characteristic angles which are functions of the scaling exponent of the slope-area curve. These findings enable us to understand the geomorphologic signature of hydrologic processes on drainage networks and develop more refined landscape evolution models.

To my lovely parents

For all your support and encouragements

# ACKNOWLEDGMENT

I would like to express the deepest appreciation to my committee chair and advisor Dr. Dingbao Wang, who has the attitude and the substance of a genius: he continually and convincingly conveyed a spirit of adventure regarding research and scholarship, and an excitement in regard to teaching. Without his guidance and persistent help this dissertation would not have been possible. I would like to thank my co-chair Dr. Stephen Medeiros and committee members Dr. Arvind Singh, Dr. John Weishampel, and Dr. Kelly Kibler for their help and support. I am also grateful to Dr. Scott Hagen for all his help throughout my doctorate research.

The research presented in this dissertation was funded in part by the Florida Space Institute (Award number: 2013-A UCF-led) and NASA Kennedy Space Center, Ecological Program, Climate Adaptation Science Investigators (CASI) project (Award number: IHA-SA-13-006).

I would like to thank my colleagues at CHAMPS lab who significantly contributed to my research in the past four years. I learnt a lot from them I am looking forward to work with them in the future. Most importantly, I am thankful of my lovely parents and brothers and Anahita Davoudi who supported me during this journey.

# TABLE OF CONTENTS

LIST OF FIGURES ..... xii
LIST OF TABLES ..... xxi
CHAPTER 1: VALLEY NETWORK EXTRACTION ..... 1
1.1 Filtering DEM and calculating curvature ..... 2
1.2 Determining flow directions ..... 3
1.3 Extracting valley and ridge skeletons ..... 6
1.4 Thinning and connecting valley network ..... 12
1.5 Results ..... 16
1.6 Conclusion ..... 18
CHAPTER 2: CHANNEL NETWORK EXTRACTION ..... 20
2.1 Cross-section profile and contours ..... 24
2.2 K-means clustering for channel head identification ..... 28
2.3 Results ..... 34
2.3.1 Sensitivity analysis ..... 37
2.3.2 Comparison to other methods ..... 39
2.3.3 Channel initiation ..... 41
2.4 Conclusions ..... 44
CHAPTER 3: WET CHANNEL EXTRACTION ..... 47

3.1 Study sites ..... 50

3.2 LiDAR and streamflow data ..... 53

3.3 Methodology and Demonstration ..... 55

3.3.1 Masking dense vegetation in intensity maps ..... 57

3.3.2 Extracting valley network and extent ..... 59

3.3.3 Decomposing composite PDF of intensity ..... 61

3.3.4 Detecting edges ..... 64

3.3.5 Identifying wet pixels ..... 66

3.3.6 Generating wet channel network ..... 67

3.4 Results ..... 70

3.4.1 Intensity thresholds ..... 70

3.4.2 Flowing channel network ..... 73

3.5 Discussion ..... 77

3.6 Conclusions ..... 80

CHAPTER 4: RE-VISITING THE DEPENDENCE OF DRAINAGE DENSITY ON CLIMATE AND DRAINAGE AREA BY LIDAR DATA ..... 83

4.1 Study Sites ..... 85

4.2 Methods ..... 87

4.2.1 Drainage network extraction ..... 87

4.2.2 Climate aridity index ..... 88

4.3 Results ..... 89

4.3.1 Drainage density and climate ..... 90

4.3.2 Drainage density and drainage area ..... 96

4.4 Discussion ..... 98

4.4.1 Drainage density and climate ..... 98

4.4.2 Drainage density and drainage area ..... 99

4.5 Conclusion ..... 100

CHAPTER 5: HYDROLOGIC CONTROLS ON CHANNEL JUNCTION ANGLE ..... 103

5.1 Data set ..... 105

5.2 Methods ..... 106

5.2.1 Valley network extraction ..... 106

5.2.2 Junction angle calculation ..... 107

5.3 Optimal junction angle ..... 108

5.4 Results and discussions ..... 113

5.4.1 Observations ..... 114

5.4.2 Explanation based on minimum energy dissipation ..... 117

5.5 Conclusion ..... 119

CONCLUSION ..... 121

REFERENCES ..... 125

# LIST OF FIGURES

Figure 1. Curvature-adjusted flow direction ($\alpha'$) for cases when (a) curvature in pixel 1 is higher than pixel 2, and (b) curvature in pixel 1 is lower than pixel 2. $\alpha$ represents the flow direction from the D∞. (c) and (d) demonstrate the valley path from the D∞ and the curvature-adjusted flow directions in two areas in Mid Bailey Run, OH. ..... 6

Figure 2. (a) Curvature along the 1-D transect shown in (b) and examples of patches. (c) The effect of increasing curvature threshold on the number of patches. The domain is separated into disconnection- and termination-dominated sections. (d) Convergent patches for two values of $\kappa_S$ (i.e., 0.01 and 0.005 $m^{-1}$). (d.1) shows a disconnection which causes a rise in the number of patches. (d.2) represents a termination, leading to a reduction in the number of patches. ..... 11

Figure 3. Procedure for extracting valley and ridge skeletons. (a) Curvature: bright colors indicate convergent areas and potential valleys. Dark colors indicate divergent surfaces and potential ridges. (b) & (c) Convergent and divergent patches, respectively. The color indicates the 95-percentile of absolute curvature in each patch, denoted by Kp. (d) Valley and ridge skeletons. . 12

Figure 4. Schematic of thinning and connecting steps. (a) No separating ridge in the enclosed area between I and II; therefore, the inferior valley is deleted. The upper bound of the enclosed area is formed by connecting the intersecting valleys at $L_{min} = \min(L_I, L_{II})$ measured from the intersection along the valleys. (b) Separating ridge inside the enclosed area between the intersecting valleys I and II; therefore, the unconfined section (downstream of ridge patch) of the inferior valley is filtered out. The unconfined area (with length denoted as $L_{un}$), corresponds to the maximum enclosed area in which there is no ridge. (c) Disconnected section that can potentially

be connected to the main network through a gap whose length along the possible valley is denoted by Lg. ..... 16

Figure 5. Valley and ridge skeleton delineations. (a), (b), and (c) show the number of patches (NP) versus the potential segmentation curvature threshold (κs) for Indian Creek, Mid Bailey Run, and a subcatchment in Feather River. All curves have easily detectable peaks denoted by κs and κs −. ..... 17

Figure 6. Number of (a) convergent and (b) divergent patches versus the potential segmentation threshold for different values of filtering parameter (TF) in Indian Creek. ..... 18

Figure 7. (a) Location of upslope (b), valley (c), and channel (d) cross-sections in the synthetic DEMs. (e), (f), and (g) Curvature and 1-m contours for synthetic DEMs. The numbers are the contour elevations in meters. The imposed channel cross-sections with well-defined banks resulted in sharp signatures in contours as highlighted by the dark background color (negative curvature). ..... 27

Figure 8. Examples of channelized and unchannelized contours in a natural landscape (Indian Creek, OH). ..... 28

Figure 9. Example of 1st-order valley with $NC$ equally-elevated contours created within the contributing extent. The upper bound of the contributing extent is constrained by the valley head elevation. The dissimilarity of contours is quantified based on their absolute orientation. For example, when comparing A and B, $A$ is reoriented toward B based on equation (12) forming the new contour $A'$. The dissimilarity index between $A$ and $B$ ($DSAB$) is calculated as the root-mean-square (RMS) difference between $A'$ and $B$ ..... 29

Figure 10. Normalized (by maximum) dissimilarity for estimates of the transition contour elevation for synthetic DEMs given in Figure 7f and Figure 7g. The minimum of these curves represents the transition from channelized to unchannelized section. ..... 34

Figure 11. Comparison of mapped and predicted channel heads: (a) delineated channel network and the mapped channel heads in Indian Creek; (b) a zoomed-in area including two mapped and predicted channels; (c) cross-section at A; (d) area with three unmapped channels where the contours clearly indicate strong crenulations; and (e) cross-section with well-defined banks at B. ..... 35

Figure 12. Distribution of error between the mapped and predicted channel heads in (a) Indian Creek (b) Mid Bailey Run, and (c) Feather River. $err$ and $\sigma$ refer to the average and standard deviation of distance error. The total number of mapped heads ($NM$), the number of mapped and predicted heads ($NMP$) are also reported. ..... 36

Figure 13. Example of mapped channelled heads located in the 2nd-order predicted valley in a subcatchment of Feather River. The presence of contour crenulations suggests the existence of channels upstream of the mapped head. ..... 36

Figure 14. Sensitivity of the proposed method in Indian Creek to (a) the time of forward diffusion ($TF$), (b) the connecting threshold ($CT$), and (c) the number of contours ($NC$) in terms of average and standard deviation of distance error. The number of heads that were mapped and predicted are shown for each parameter value. ..... 38

Figure 15. Distribution of standard deviation of distance error ($\sigma err$) at individual heads, which represents the change in predicted head location caused by alteration of $Nc$ in Indian Creek..... 39

Figure 16. Distribution of curvature at the mapped and predicted channel heads in (a) Indian Creek (b) Mid Bailey Run, and (c) Feather River. The average and the coefficient of variation (CV) for each distribution are given. ..... 43

Figure 17. Curvature at the mapped versus predicted channel heads. The data points were binned along the horizontal axis using a 0.005 $m^{-1}$ bin size and the 25, 50, and 75 percentiles at each bin are presented. The dashed black line represents the linear fit in the range of 0.03-0.09 $m^{-1}$ which indicates a strong linear correlation with $R2 = 0.73$..... 44

Figure 18. Map for the study sites. (a) Five study watersheds around Lake Tahoe. (b) Six streamflow gages and the spatial coverage of LiDAR data sets. ..... 52

Figure 19. Rainfall and hydrograph for Blackwood Creek, and the LiDAR acquisition periods during (a) 8/20/2010-8/23/2010 and (b) 6/20/2012-6/21/2012..... 55

Figure 20. LiDAR intensity for a headwater catchment in the Blackwood Creek watershed during (a) 2010 and (b) 2012 surveys. The wet channel heads (i.e., upstream limits of wet channels) are identified visually and marked by green dots. ..... 56

Figure 21. The intensity of returns from (a) the top of canopy and (b) the ground surface in the Blackwood Creek watershed based on 2012 LiDAR survey. ..... 58

Figure 22. (a) The extent of dense vegetation, identified at the locations where the elevation difference between the top of canopy and the ground surface is more than 2 m. (b) The modified LiDAR intensity map after masking dense vegetated areas (Blackwood Creek watershed using 2012 LiDAR survey)..... 59

Figure 23. (a) Contour curvature and the visually detectable drainage path by blue segments. (b) The intensity returns within the valley boundary determined by the curvature threshold ($\kappa v$) of $0.025\ m-1$ in the Blackwood Creek watershed based on 2012 LiDAR survey. ..... 61
Figure 24. (a) A schematic representation of the composite and the individual PDFs of intensity return along with the wet ($IW$) and dry ($ID$) thresholds. (b) The membership probability of each mode. (c) The uncertainty of wet mode cluster visualized as hatched areas. ..... 64
Figure 25. Extracting wet pixels in the Blackwood Creek watershed based on 2012 LiDAR survey. (a) The original intensity map where the wet channels are visually detectable as dark and narrow segments with detectable edges (i.e., abrupt transition from wet to dry in the channel banks). (b) The detected edges in the intensity return map. ..... 66
Figure 26. The identified wet pixels based on intensity thresholds for wet and dry pixels from decomposed intensity PDFs, and the detected edges for 2012 LiDAR survey in the Blackwood Creek watershed. ..... 67
Figure 27. Overlay of intensity map and valley network extracted from LiDAR-based DEM for 2012 LiDAR survey in the Blackwood Creek watershed. Some valley segments are not exactly located within the wet channel boundary. ..... 69
Figure 28. Extracting wet channel network in the Blackwood Creek watershed. (a) The base valley network extracted from topographic data, and the wet cells identified based on LiDAR intensity. (b) The connected wet channel network along with the base valley network after processing wet channel segments. ..... 70
Figure 29. The multimodal PDF of intensity returns and the decomposed individual distributions representing wet, transitional and dry modes along with the wet ($Iw$) and dry ($Id$) transitions, (a)

& (b) for the Blackwood Creek watershed based in 2010 and 2012, (c) & (d) for the Ward Creek watershed in 2010 and 2012, (e) for the General Creek watershed in 2010, (f) for the Trout Creek watershed in 2010, and (g) for the Incline Creek watershed in 2010. ..... 72

Figure 30. Connected wet channel (after deleting isolated wet channel segments) and valley network based on LiDAR data for Blackwood Creek watershed in 2010 (a) and 2012 (b), Ward Creek watershed in 2010 (c) and 2012 (d), General Creek watershed in 2010 (e), Trout..... 76

Figure 31. (a) Identified wetted channel length and measured streamflow in the Blackwood Creek watershed (red triangle) and Ward Creek watershed (black circle). (b) Relationship between wetted channel length and streamflow across all the study watersheds. ..... 78

Figure 32. (a) The locations of the study sites and the LiDAR data availability across United States; and (b) the cumulative probability distribution of the climate aridity index ($EP/P$) in the study sites. ..... 86

Figure 33. The relationship between PE index and climate aridity index ($EP/P$) using the data provided by *Wang and Wu* [2013b] after removing the outliers. ..... 86

Figure 34. (a) The contour curvature computed from the filtered DEM; and (b) the extracted valley network from 1 m and 30 m DEMs in the Isleta Drain watershed located in New Mexico..... 88

Figure 35. The relationship between drainage density ($Dd$) and climate aridity index ($EP/P$); (a) the data from Melton [1957], Madduma Bandara [1974], and this study. (b) The correlation analysis of drainage density and climate aridity index in the study watersheds. The least-squares regression line, slope ($m$), R-squared ($R2$), and p-value ($p$) are shown. For $EP/P > 1$ (arid regions), a significant increasing trend is observed; whereas, the trend in humid regions ($EP/P \geq 1$) is not significant. ..... 92

Figure 36. Drainage density ($Dd$) derived from LiDAR-based 1 m DEMs compared with (a) the resampled 30 m DEMs and Melton [1957]'s data; and (b) the resampled 15 m DEMs and Madduma Bandara [1974]'s data. The least-squares regression line to data from resampled DEMS and the corresponding slope (m), R-squared (R2), and p-value (p) are shown. ..... 93
Figure 37. Drainage density ($D_d$) versus mean annual precipitation ($P$) after dividing the data into arid and humid based on (a) $P$ with $PT = 1050mmyr$, and (b) climate aridity index ($EP/P$). The least-squares regression lines, slopes ($m$), R-squared ($R2$), and p-value ($p$) are shown. ..... 95
Figure 38. The relationship between drainage density ($Dd$) and drainage area for (a) arid and (b) humid watersheds in this study, (c) watersheds in the arid climate from Melton [1957] , and (c) watersheds in the humid climate from Madduma Bandara [1974]. The least-squares regression line, slope ($m$), R-squared ($R2$), and p-value ($p$) are shown. ..... 97
Figure 39. The relationship between drainage density ($D_d$) and climate aridity index ($EP/P$): (a) Average, minimum and maximum of drainage density from subwatersheds with different drainage area in the selected 30 study sites; and (b) The standard deviation of drainage density ($\sigma Dd$) of subwatersheds in each study site versus climate aridity index. ..... 100
Figure 40. The locations of the 120 study catchments in the United Sates. ..... 106
Figure 41. Junction examples in a catchment located in northern Georgia. The junctions are marked by red dots and the dashed-blue lines represent the fitted lines. The length ($Lf*$) of the fitted line with the highest $R2$ and the calculated angle at each junction are shown in blue and red texts, respectively. ..... 108
Figure 42. (a) A symmetric junction with the vertical and horizontal dimensions denoted by $X$ and $Y$. (b) The contributing area and the length of the upstream ($Au$ and $Lu$) and downstream reaches

($Ad$ and $Ld$). The junction angle is denoted as $\alpha$, and $\beta$ represents the junction angle between downstream link and the channel within the neighbouring tributary. ..... 110

Figure 43. (a) The optimal junction angle $\alpha$ for various values of $\gamma$ and $r$; (b) The optimal angle ($\alpha$) and the downstream angle ($\beta$) when $\gamma = 0.75$. Two curves intersect at $\alpha = \beta \approx 65.3°$. The intersection is denoted by $\alpha s$. This indicates that if $\gamma = 0.75$, the stable branching angle would be $\alpha s = 65.3°$. ..... 112

Figure 44. $\alpha s$ for different values of $m = 1 - \gamma$, where $m$ is the exponent of slope-area relationship ($S \propto A - m$). The crosses represent the characteristic angles for debris-flow dominated and fluvial regimes based on the observations in the study catchments. The vertical line at each point correspond to the range of the characteristic angles quantified using different approaches (GMM, angle-area curve and slope-area curve; see section 4.1) and reflects the uncertainty..... 113

Figure 45. The valley network and the junction angles for a drainage network located in northern Georgia, United States. ..... 114

Figure 46. (a) The PDF of the observed junction angle ($\alpha obs$) using a bin size of 5°. (b) The decomposed PDFs from (a) using the Expectation-Maximization algorithm. The extracted modes exhibit the averages of $47.0°$ and $76.6°$ with the standard deviations of $24.5°$ and $22.4°$, respectively. ..... 115

Figure 47. The observed junction angle ($\alpha obs$) versus the contributing area ($A$). The curves represent 25$^{th}$ , 50$^{th}$ and 75$^{th}$ percentiles, respectively. The junction angle starts from $54.0°$ (the average of the 50$^{th}$ percentile for $2.5 \leq Log(A) \leq 3.9$) for small contributing area and approaches

to 75.8° (the average of the 50$^{th}$ percentile for $5.5 \leq \mathrm{Log(A)} \leq 6.4$), where the transitions are visually identified..... 116

Figure 48. (a) The slope-area curve for the study sites. The curve exhibits log-log linear relationships with the exponents $m1 = 0.15$ and $m2 = 0.37$. The transition occurs at $AT = 103.9$ m$^2$. (b) The junction angle distributions for $A < AT$ and $A \geq AT$. ..... 117

# LIST OF TABLES

Table 1. Performance of DrEICH, GeoNet, Pelletier and the proposed method in terms of the average error ($err$), standard deviation of error ($\sigma$), reliability ($r$), sensitivity ($s$), and percentage error of mapped and predicted channel densities ($\varepsilon D$) in Indian Creek and Mid Bailey Run. ..... 41

Table 2. USGS gage identification number, drainage area, streamflow and its exceedance probability during the LiDAR surveys for the study watersheds. ..... 52

Table 3. Thresholds for identifying wet and dry channels for the study watersheds..... 71

Table 4. Trend analysis based on the Mann-Kendall test for arid and humid watersheds. ..... 91

Table 5. The slope ($m$) and p-value ($p$) of the least-squares regression line fitted to the data points with $P > PT$ for different values of $PT$ ..... 95

Table 6. The characteristic angles extracted from three methods..... 118

# CHAPTER 1: VALLEY NETWORK EXTRACTION

Valleys and channels are important geomorphologic and hydrologic features. Valleys are generally associated with convergent topography in the landscape [*Montgomery and Foufoula-Georgiou*, 1993; *Howard*, 1994], and channels are the sections of valleys constrained by well-defined banks [Montgomery and Dietrich, 1989]. Channels initiate at some distance down from the valley head, and the transition from unchannelized valley to channel is referred to as the channel head [*Montgomery and Foufoula-Georgiou*, 1993]. Channel heads occur at a point where fluvial transport dominates over diffusive transport [Dietrich et al., 1987; Tarboton et al., 1992].

A curvature-based approach is developed to delineate the valley network by utilizing both positive (i.e., convergent topography) and negative (i.e., divergent topography) curvature. The resulting valley skeleton is then thinned by keeping the valleys that are separated by one ridge (i.e., negative curvature patch). The resulting valley skeleton is then thinned by keeping the valleys that are separated by one ridge (i.e., negative curvature patch). The procedure for extracting valley network uses the location of valleys and ridges, which are defined as convergent and divergent topography, respectively. Ridges correspond to the flow separation lines that define the boundaries of subcatchments and separate surface runoff between neighboring valleys.

## 1.1 Filtering DEM and calculating curvature

Curvature-based valley network extraction requires smoothing the DEM [*Lashermes et al.*, 2007; *Passalacqua et al.*, 2010b]. The Gaussian filter [Lashermes et al., 2007], Perona-Malik filter [*Passalacqua et al.*, 2010b] and optimal Wiener filter [Pelletier, 2013] have been previously used for this purpose. The optimal Wiener filter converts the original DEM into frequency space using Fourier transforms and filters out the frequencies representing noise [Press et al., 2007]. The Perona-Malik filter is a nonlinear diffusive filter that utilizes an edge-stopping function to remove the noise while enhancing the edges. The proposed method uses the Perona-Malik filter due to its robust performance [*Passalacqua et al.*, 2010b; *Passalacqua et al.*, 2010a; *Passalacqua and Foufoula-Georgiou*, 2015]. The Perona-Malik filter employs a parameter referred to as "time of forward diffusion" and denoted by $T_F$ [Passalacqua and Foufoula-Georgiou, 2015]. $T_F$ is the number of iterations for the numerical representation of derivatives for smoothing. The derivatives are approximated using standard finite differences with one pixel spacing as suggested by Weickert and Benhamouda [1997]. More information regarding the numerical approximations for nonlinear filters can be found in Weickert [1997]. $T_F$ was set to 50 for the results presented in this chapter and the sensitivity of results to this parameter is presented in Section 3.3.

The curvature of a surface includes profile curvature in the gradient direction (direction of steepest slope) and contour curvature perpendicular to the gradient direction. Profile curvature reflects the change in the slope angle in the gradient direction; whereas, contour curvature represents the change in the aspect angle and reflects the convergence/divergence of the surface [*Mitasova and Hofierka*, 1993]. Positive contour

curvature implies flow convergence and indicates a valley candidate. Contour curvature is computed as [*Mitasova and Hofierka*, 1993]:

$$\kappa = \frac{z_{xx}z_y{}^2 - 2z_{xy}z_xz_y + z_{yy}z_x{}^2}{(z_x{}^2 + z_y{}^2)\sqrt{1 + z_x{}^2 + z_y{}^2}} \quad (1)$$

where, x and y are the global DEM coordinates. $z_x$ and $z_{xx}$ ($z_y$ and $z_{yy}$) represent the first and second derivatives of elevation (z) with respect to x (y). $z_{xy}$ is the first derivative of $z_x$ with respect to y. In order to robustly calculate contour curvature (simply referred to as curvature hereafter) for each pixel, a fourth-order polynomial function (equation 2) is fitted to each 3 × 3 moving window:

$$z = Ax^2y^2 + Bx^2y + Cxy^2 + Dx^2 + Ey^2 + Fxy + Gx + Hy + I \quad (2)$$

This leads to the following equation for computing curvature based on the coefficients of the polynomial function in equation (2):

$$\kappa = \frac{2GE^2 - 2FGH + 2EG^2}{(G^2 + H^2)\sqrt{1 + G^2 + H^2}} \quad (3)$$

## 1.2 Determining flow directions

Flow directions are typically determined after iteratively removing all sinks in the filtered DEM as suggested by *O'callaghan and Mark* [1984b]. Several algorithms (e.g., MFD [Quinn et al., 1991] and $D_\infty$ [*Tarboton*, 1997b]) have been proposed to determine flow directions based on elevation. However, other topographic attributes, including curvature [*Passalacqua et al.*, 2010b] and downslope gradient [Qin et al., 2007], have been shown to be important in local flow partitioning and channel path extraction. Here, flow directions are determined by considering both the flow toward the steepest downward slope and the flow

perpendicular to it. The former relates to the response of flow to the profile slope as considered in traditional methods for determining flow directions such as the $D_\infty$. The latter, referred to as the cross-sectional flow, is attributed to the flow response to the cross-sectional slope and is directed toward the flow concentration point (or potential channel centerline). The curvature in equation (1) represents the slope gradient perpendicular to the steepest downward slope and represents the average cross-sectional slope. Since the cross-sectional slope and curvature increase moving toward the channel's centerline, the cross-sectional flow is from low to high curvature pixels.

Based on the $D_\infty$ concept, flow direction is toward two neighboring pixels located in the steepest downward slope direction [*Tarboton*, 1997b]. These two downstream pixels are marked as 1 and 2 counterclockwise in Figure 1a and Figure 1b. $\kappa_1$ and $\kappa_2$ denote the curvature of pixels 1 and 2, respectively. Given the flow direction from the $D_\infty$, denoted by $\alpha$ and shown by the dashed arrow in Figure 1a and Figure 1b, a modified flow direction, denoted by $\alpha'$ and shown by the solid arrow, is defined by rotating the flow direction toward the pixel with higher curvature based on equation (4.1):

$$\alpha' = \hat{\alpha} + (\alpha - \hat{\alpha}) r_\kappa \tag{4.1}$$

where $\hat{\alpha}$ and $r_\kappa$ are defined as below and $\alpha$ is the flow direction from the $D_\infty$:

$$\hat{\alpha} = \begin{cases} \frac{\pi}{4}\left\lfloor \alpha \left(\frac{\pi}{4}\right)^{-1} \right\rfloor & \kappa_1 > \kappa_2 \\ \frac{\pi}{4}\left\lceil \alpha \left(\frac{\pi}{4}\right)^{-1} \right\rceil & \kappa_2 > \kappa_1 \end{cases} \tag{4.2}$$

$$r_\kappa = \begin{cases} \frac{\kappa_2}{\kappa_1} & \kappa_1 > \kappa_2 \\ \frac{\kappa_1}{\kappa_2} & \kappa_2 > \kappa_1 \end{cases} \tag{4.3}$$

In equations (4.2), the symbols ⌊ ⌋ and ⌈ ⌉ represent floor and ceiling functions that map a real number to the largest previous integer and the smallest following integer, respectively. When $\kappa_1$ or $\kappa_2$ is negative, no modification to the flow direction is performed. Based on equation 4, the adjusted flow directions are determined first by finding the two downstream pixels utilizing slope, then adjusting them based on curvature. Therefore, slope is the first order control on the adjusted flow directions and the curvature is the second order factor. After obtaining the flow directions, the upslope area grid is calculated by performing the flow accumulation algorithm proposed by *Tarboton* [1997b].

Figure 1c and Figure 1d illustrate the one-pixel-wide flow path from the $D_\infty$ and the adjusted flow directions using curvature in two zoomed-in areas located in Mid Bailey Run, OH. The flow path is extracted as the local maximums of the flow accumulation grid along the flow direction. The paths predicted by the $D_\infty$ clearly pass through the ridges (divergent contours). The adjusted flow directions consider both flow toward the steepest downward slope and the cross-sectional flow toward the concentration points by incorporating the curvature; therefore, the flow path shifts slightly toward the contour crenulations.

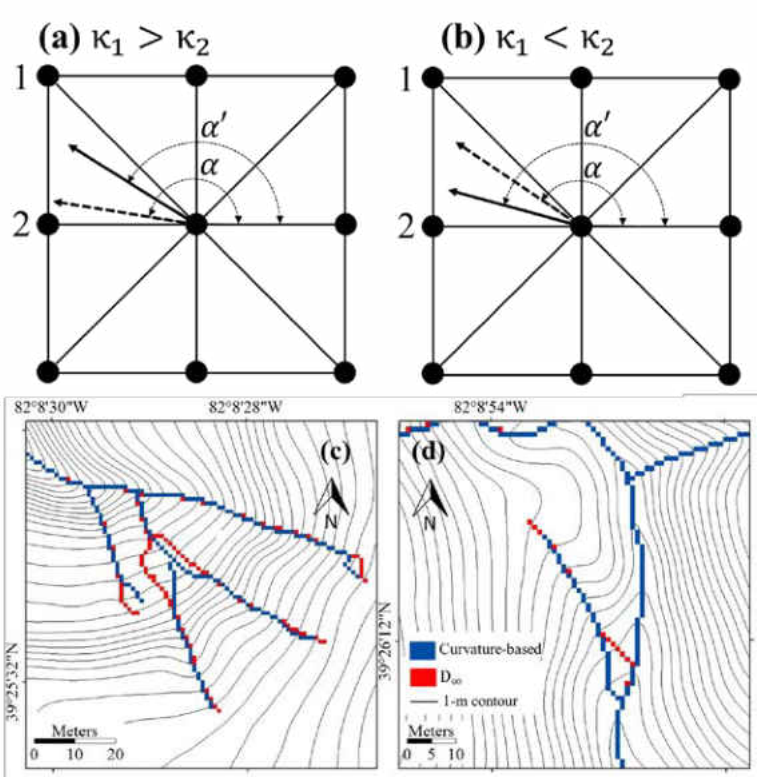


Figure 1. Curvature-adjusted flow direction ($\alpha'$) for cases when (a) curvature in pixel 1 is higher than pixel 2, and (b) curvature in pixel 1 is lower than pixel 2. $\alpha$ represents the flow direction from the $D_\infty$. (c) and (d) demonstrate the valley path from the $D_\infty$ and the curvature-adjusted flow directions in two areas in Mid Bailey Run, OH.

### 1.3 Extracting valley and ridge skeletons

Delineating drainage networks from high-resolution DEMs often requires extracting the valley skeleton as the potential extent of the valley network. In curvature-based methods, the valley skeleton is usually extracted by imposing a curvature threshold. Based on the difference of curvature distribution between hillslope and valley, Lashermes et al. [2007] extracted the threshold from the curvature q-q plot. *Passalacqua et al.* [2010b] and Sofia et al. [2011] utilized a similar approach; and Sofia et al. [2011] additionally used an openness

threshold from the corresponding q-q plot. The existing methods for extracting skeletons were developed based on the curvature of individual pixels. A pixel with a curvature that exceeds a threshold is considered part of the skeleton regardless of local terrain conditions. Occasionally, the curvature values at the upper sections of valleys and hillslopes may coincide. A pixel with a relatively small positive curvature may be a part of the valley skeleton or hillslope, and it is impossible to differentiate this based only on the curvature of the pixel. Therefore, it is necessary to consider local terrain conditions when extracting the skeleton.

In this chapter, a systematic approach is proposed to extract valley and ridge skeletons considering curvature and local terrain conditions. The following explanation is focused on the valley skeleton; a similar procedure applies to ridge skeleton extraction.

In this context, a terrain consists of patches and their surrounding area. Patches are defined as local maximums in the curvature grid. For demonstration, the curvature and patches along a 1D transect are shown in Figure 2a and Figure 2b; in reality patches exist in the 2D plane. Some patches belong to the valley skeleton and are referred to as valley patches; the rest are isolated convergent surfaces on hillslopes and referred to as non-valley patches. The valley patches generally have confined flow with active channel incisions in some locations. This process tends to increase the convergence of the channelized sections of valley patches, and consequently the maximum curvatures within the valley patches are higher than those in the non-valley patches where the incision process does not occur. Therefore, a statistically higher peak curvature within valley patches is expected compared with non-valley patches.

In this case, before extracting the valley skeleton, it is necessary to identify patches by imposing a segmentation curvature threshold ($\kappa_s$). $\kappa_s$ is the lower bound of the convergence curvature threshold, i.e., any pixel with $\kappa < \kappa_s$ is not part of the valley skeleton; however, pixels with $\kappa \geq \kappa_s$ may be part of the valley skeleton depending on the patch they are attached to. For any estimate of $\kappa_s$, denoted by $\widehat{\kappa_s}$, patches are identified as the set of contiguous pixels with $\kappa \geq \widehat{\kappa_s}$ by performing connected-component labeling [Suzuki et al., 2003] using eight-neighbor connectivity. The ideal segmentation threshold satisfies the following criteria: (1) all potential non-valley patches are detached; and (2) all potential valley patches are kept. It is computationally expensive, if not practically impossible, to determine such an ideal segmentation threshold; however, a reasonable estimation of the threshold can be obtained by investigating the total number of patches ($N_P$) as a function of $\widehat{\kappa_s}$. As $\widehat{\kappa_s}$ increases from 0, $N_P$ changes as the result of two main processes: disconnection and termination. Through the disconnection process a patch splits into two or more, leading to an upsurge in $N_P$ (Figure 2d.1). Alternatively, the termination process describes the disappearance of a patch as $\widehat{\kappa_s}$ increases, causing $N_P$ to decrease (Figure 2d.2).

As shown in Figure 3c, with the increase of $\widehat{\kappa_s}$, $N_P$ increases initially indicating the domination of the disconnection process, and then decreases due to the domination of the termination process. Based on the definition of the ideal segmentation threshold, disconnection is desirable since non-valley patches, through the disconnection process, are likely to be detached from valley patches. However, the termination process can lead to an erroneous valley skeleton as potential valley patches may disappear. Consequently, the

transition from the disconnection-dominated phase to the termination-dominated phase (i.e., $\widehat{\kappa_s}$ that creates maximum $N_P$) is a reasonable choice for the segmentation threshold.

After identifying the patches, the valley skeleton can be extracted by removing non-valley patches. As mentioned earlier, valley patches are expected to have higher peak curvature compared with non-valley patches. This property facilitates identification of the valley patches. To minimize the effect of point-scale erroneous peaks, the 95-percentile of curvature in each patch p (denoted by $K_p$) is used to represent the peak curvature (Figure 3b). The problem of valley skeleton extraction is transformed into the task of identifying a peak curvature threshold, denoted by $K_T$, so that p is a valley patch if $K_p \geq K_T$. As suggested by Otsu [1975], a reasonable choice for $K_T$ is the value which maximizes the variance of $K_p$ between valley and non-valley patches (i.e., the inter-class variance). Mathematically, this can be presented as the following optimization problem:

$$K_T = \underset{x}{\operatorname{argmax}}\, N_v(x)N_{nv}(x)[\overline{K}_v(x) - \overline{K}_{nv}(x)]^2 \tag{5.1}$$

where,

$$N_v(x) = \sum_{i=1}^{N_P}\{1|K_p^i \geq x\} \tag{5.2}$$

$$\overline{K}_v(x) = \frac{\sum_{i=1}^{N_P}\{K_p^i|K_p^i \geq x\}}{N_v(x)} \tag{5.3}$$

$$N_{nv}(x) = \sum_{i=1}^{N_P}\{1|K_p^i < x\} \tag{5.4}$$

$$\overline{K}_{nv}(x) = \frac{\sum_{i=1}^{N_P}\{K_p^i|K_p^i < x\}}{N_{nv}(x)} \tag{5.5}$$

where $K_p^i$ represents $K_p$ of the patch i; $N_v$ and $N_{nv}$ are the number of valley and non-valley patches, respectively; and $\overline{K}_v$ and $\overline{K}_{nv}$ denote average $K_p$ values for valley and non-valley patches, respectively.

The ridge skeleton can be extracted by applying the same procedure to the additive inverse of the curvature grid; i.e., the curvature multiplied by -1 (Figure 3c and Figure 3d). In this case, the patches consist of ridge and non-ridge patches. The ridge patches are adjacent to the valley patches with confined flow and channel incision; therefore, they are expected to be relatively more divergent with smaller peak curvature. Although the ridge and valley skeletons are extracted using the same method, the procedures are independent.

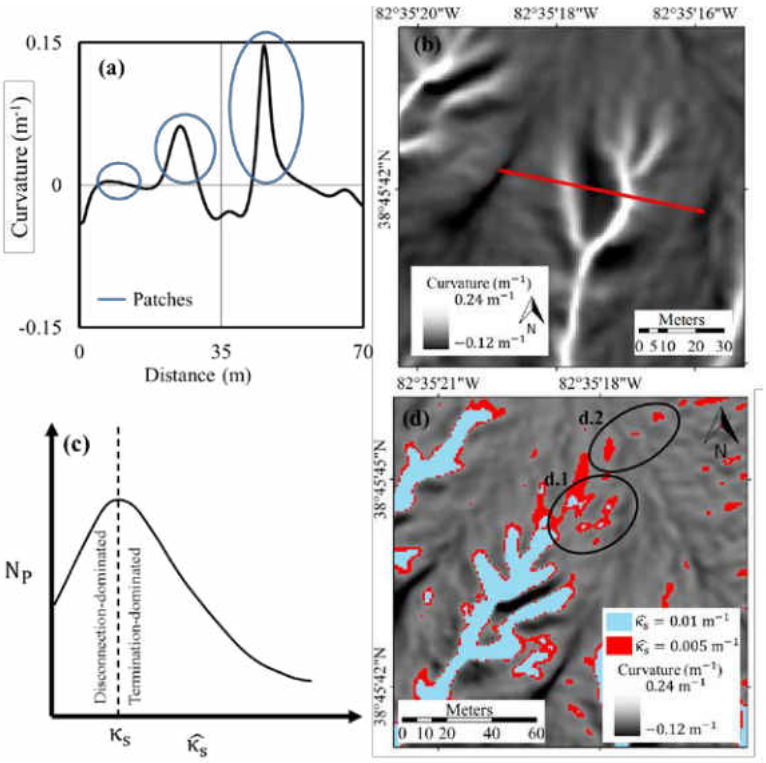


Figure 2. (a) Curvature along the 1-D transect shown in (b) and examples of patches. (c) The effect of increasing curvature threshold on the number of patches. The domain is separated into disconnection- and termination-dominated sections. (d) Convergent patches for two values of $\hat{\kappa}_s$ (i.e., 0.01 and 0.005 $m^{-1}$). (d.1) shows a disconnection which causes a rise in the number of patches. (d.2) represents a termination, leading to a reduction in the number of patches.

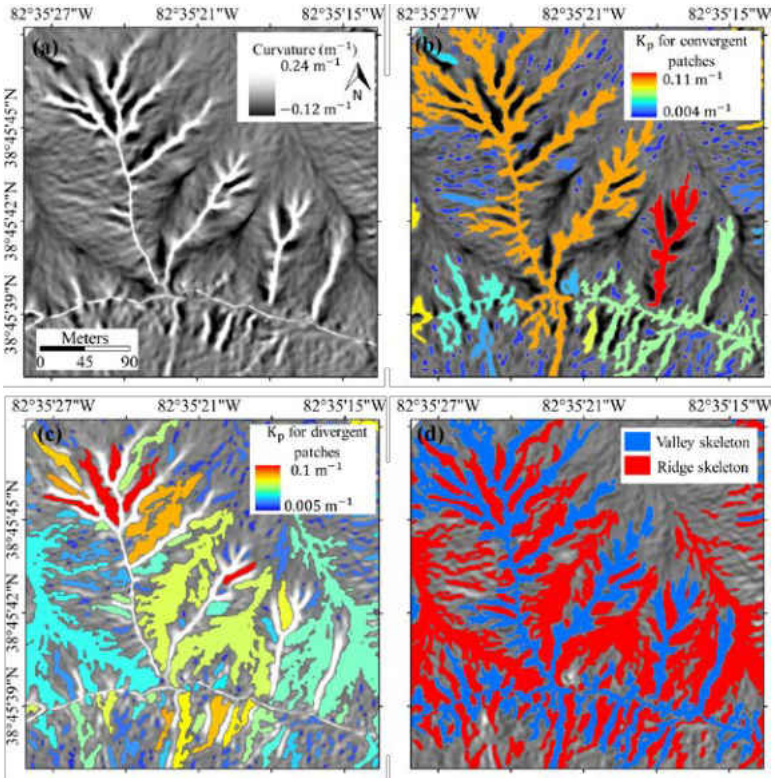


Figure 3. Procedure for extracting valley and ridge skeletons. (a) Curvature: bright colors indicate convergent areas and potential valleys. Dark colors indicate divergent surfaces and potential ridges. (b) & (c) Convergent and divergent patches, respectively. The color indicates the 95-percentile of absolute curvature in each patch, denoted by $K_p$. (d) Valley and ridge skeletons.

### 1.4 Thinning and connecting valley network

After extracting the valley and ridge skeletons, an initial valley network is created within the valley skeleton as line segments. The details regarding the delineation of the initial valley network is presented at the end of this section. The initial valley network is often unrealistically dense and disconnected; therefore, it usually must undergo post-processing phase including thinning and connecting.

In the thinning step, each pair of intersecting valleys is checked for the existence of a separating ridge. If a ridge is not detected between the valleys, one of them is selected as the inferior valley and filtered out. If the two valleys are in different Strahler orders, the one with the smaller order is selected as the inferior valley; otherwise, the one with a lower average curvature along the valley is selected as the inferior one since the true valleys lay on the contour crenulations where the curvature is relatively high. Figure 4a.1 shows a schematic example of this process when comparing intersecting valleys marked as I and II. Initially the enclosed area is searched for a ridge. The upper bound of the enclosed area is formed by connecting the intersecting valleys at $L_{min} = \min(L_I, L_{II})$, where $L_I$ and $L_{II}$ are distances measured from the intersection along the valleys. Since there is no separating ridge inside the enclosed area, the inferior valley is filtered out as shown in Figure 4a.2.

In some cases, there is a relatively small ridge, compared to the valley length, between a pair of intersecting valleys. These small patches typically correspond to the elevated bed within a single valley cross-section and cannot be considered as separating ridges. To address this issue, when a ridge patch is detected, the section of the inferior valley located downstream of the ridge, referred to as the unconfined section, is filtered out and the upstream part is kept. This process is illustrated in Figure 4b for the intersecting valleys marked as I and II. The unconfined area (with length denoted by $L_{un}$) corresponds to the maximum enclosed area in which there is no ridge. In this case, the unconfined section of the inferior valley is filtered as shown in Figure 4b.2. This creates a disconnection in the valley network, shown by the dashed line, which is processed in the connecting step.

The disconnections in the valley network are due to either erroneous filtering of valley patches or the thinning step as discussed previously. Valleys located upstream of each gap should generate enough flow to pass through the gap and connect to the downstream network. Here, it is assumed that discharge from groundwater along the entire network contributes to streamflow. From Darcy's law and assuming spatially uniform hydraulic conductivity, the flow per unit length of valley (q) is proportional to the water table slope ($\omega$). Assuming that the water table is parallel to the land surface [Beven and Kirkby, 1979], $\omega$ can be approximated as the cross-sectional slope. In order to avoid the complexity of calculating the cross-sectional slope, it is assumed to be linearly proportional to the local curvature; i.e., $\omega \propto \kappa$. This assumption is reasonable since the curvature in equation (1) represents the slope gradient perpendicular to the steepest downward slope, which is proportional to the average cross-sectional slope. Therefore, the total flow from any connected segment of valley network is:

$$Q \propto \sum_{i \epsilon V_d} \Delta l_i \times \kappa_i \qquad (6)$$

where $\kappa_i$ and $\Delta l_i$ are the curvature and length (along the flow direction) of pixel $i$, respectively; and $V_d$ denotes the set of pixels in the disconnected segment. Q from equation (6) should be high enough to pass through the downstream gap, the length of which is measured along the potential connection and denoted by $L_g$. The upstream part is connected if:

$$L_g < C_T \sum_{i \epsilon V_d} \Delta l_i \times \kappa_i \qquad (7)$$

where $C_T$ is a watershed specific parameter referred to as the "connecting threshold" and is controlled mainly by the topographic features such as the shape of channelized cross-

sections (width and area) and the geometry of the gaps. $C_T$ was set to 20 m for the results presented in this chapter. The sensitivity of the results to $C_T$ is presented in Section 3.3.

As mentioned earlier, an initial valley network within the valley skeleton as line segments are created before the thinning and connecting steps. The initial valleys are originated when upslope pixels create sufficient flow to pass through the next pixel. The length of the pixel along the flow path is approximated by the DEM resolution, denoted by $\Delta$. From equation (7) and using $L_g = \Delta$, pixel c is an initiation point if $\sum_{i \epsilon U_c} \kappa_i > \Delta \times {C_T}^{-1}$, where $U_c$ represents all of the pixels within the valley skeleton and located upstream of c. The final valley network is extracted by performing the connecting and thinning steps on the initial network.

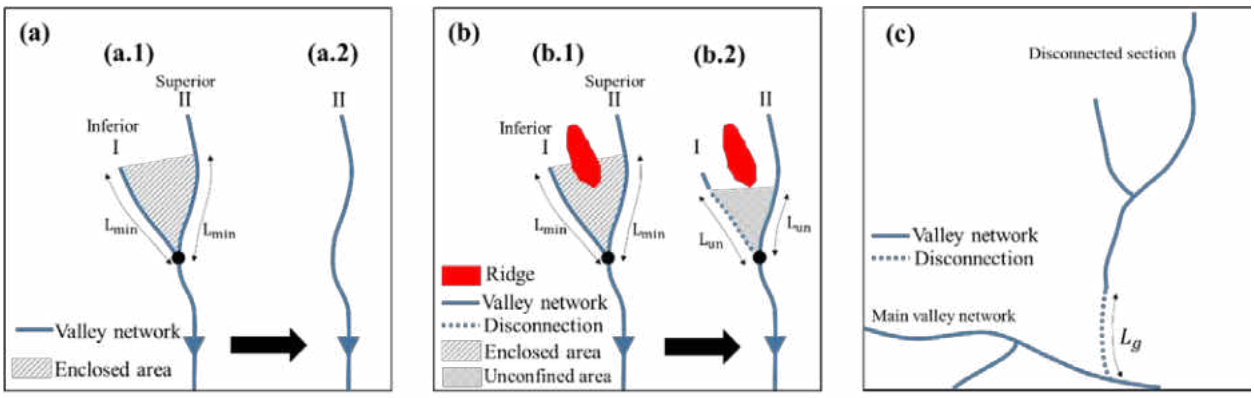


Figure 4. Schematic of thinning and connecting steps. (a) No separating ridge in the enclosed area between I and II; therefore, the inferior valley is deleted. The upper bound of the enclosed area is formed by connecting the intersecting valleys at $L_{min} = \min(L_I, L_{II})$ measured from the intersection along the valleys. (b) Separating ridge inside the enclosed area between the intersecting valleys I and II; therefore, the unconfined section (downstream of ridge patch) of the inferior valley is filtered out. The unconfined area (with length denoted as $L_{un}$), corresponds to the maximum enclosed area in which there is no ridge. (c) Disconnected section that can potentially be connected to the main network through a gap whose length along the possible valley is denoted by $L_g$.

## 1.5 Results

To evaluate the performance of the proposed method, the valley and channel networks were extracted in three catchments with channel heads mapped in the field by Clubb et al. [2014]: Feather River in California, Mid Bailey Run and Indian Creek in Ohio. Clubb et al. [2014] used the same catchments to evaluate the performance of three state-of-the-art methods for channel network extraction proposed by *Passalacqua et al.* [2010b], Pelletier [2013], and Clubb et al. [2014].

For the three study catchments, the valley networks were extracted from LiDAR-based 1-m bare earth DEMs. Initially, the DEMs were smoothed using a Perona-Malik filter with $T_F = 50$ (see Section 2.1.1). The curvature was then calculated from the smoothed DEM using equation (1). $N_P$ (i.e., the number of patches) versus the potential segmentation threshold ($\widehat{\kappa_s}$) in Indian Creek, Mid Bailey Run, and a subcatchment in Feather River are shown in Figure 5. Although all curves contain easily detectable peaks, the magnitudes of segmentation thresholds are noticeably different and location-specific. The valley skeleton was extracted by imposing the derived threshold ($\kappa_s$) and filtering any patch with $K_p < K_T$, where $K_p$ is the 95-percentile of curvature within each patch and $K_T$ was calculated from equation (5). The ridge skeleton was extracted following the same procedure on the additive inverse of the curvature grid. The segmentation threshold for the ridge skeleton is denoted by $\widehat{\kappa_{s-}}$ in Figure 5. An initial valley network was created within the valley skeleton then connected and thinned using $C_T = 20$ m following the procedure explained in Section 2.1.4.

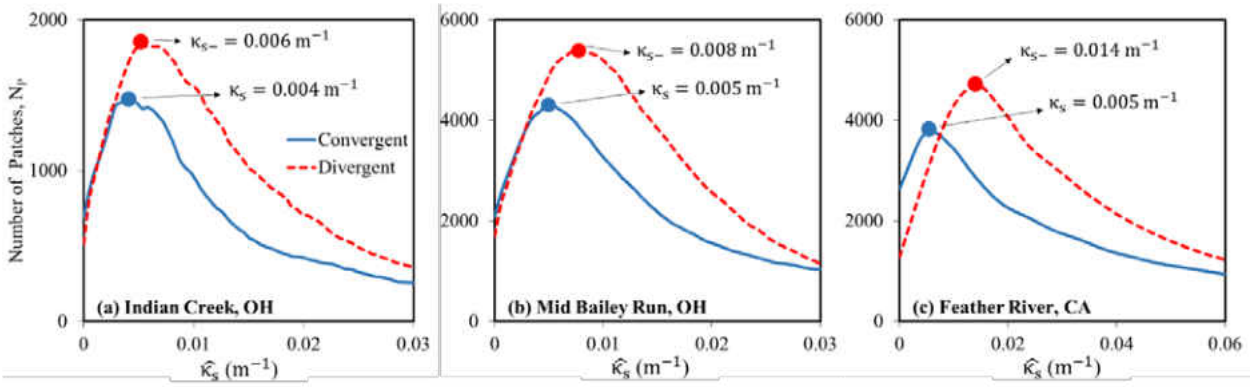


Figure 5. Valley and ridge skeleton delineations. (a), (b), and (c) show the number of patches ($N_P$) versus the potential segmentation curvature threshold ($\widehat{\kappa_s}$) for Indian Creek, Mid Bailey Run, and a subcatchment in Feather River. All curves have easily detectable peaks denoted by $\kappa_s$ and $\kappa_{s-}$.

The segmentation of terrain under different values of the filtering parameter ($T_F$) was also investigated. Higher values of $T_F$ produce rougher contours at channels and ridges, but reduce the noise and eliminate small features. Therefore, the number of convergent and divergent patches decreases with increasing $T_F$ as shown in Figure 6. Despite this trend, for any value of $T_F$ the curves in Figure 6 display easily-detectable peaks. The curvature at the peaks, which correspond to the segmentation thresholds, increases with decreasing $T_F$.

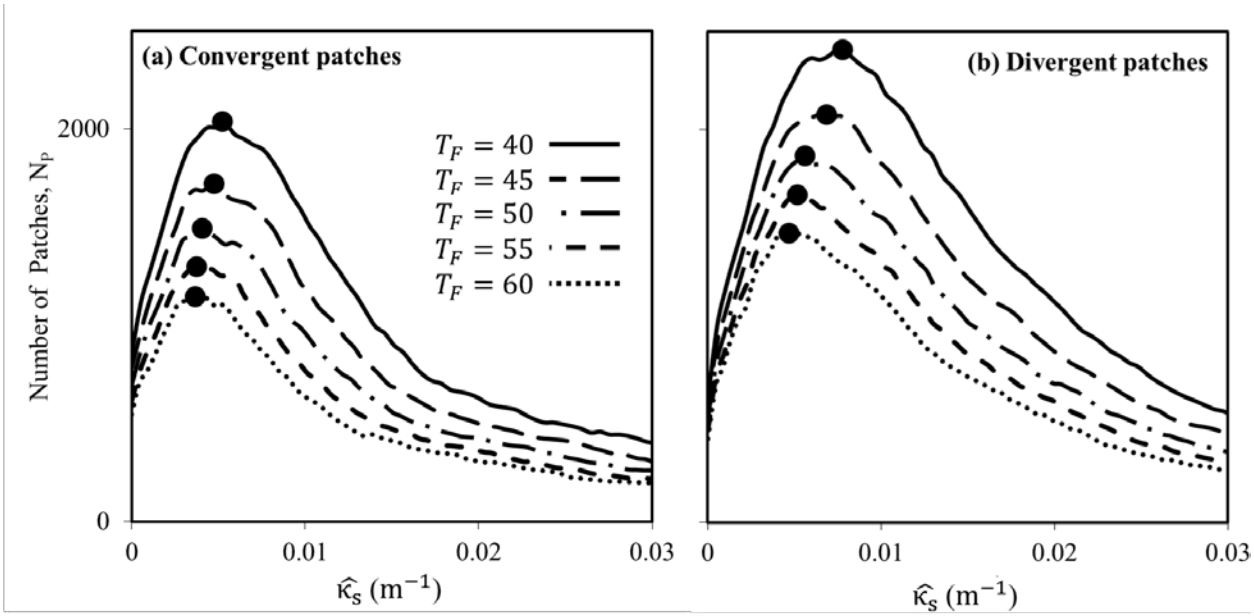


Figure 6. Number of (a) convergent and (b) divergent patches versus the potential segmentation threshold for different values of filtering parameter ($T_F$) in Indian Creek.

## 1.6 Conclusion

Valleys are defined as convergent topography in the landscape, and the convergence is naturally associated with positive contour curvature. Delineating drainage networks from high-resolution DEMs often requires extracting the valley skeleton as the potential extent of

the valley network. In curvature-based methods, the valley skeleton is usually extracted by imposing a curvature threshold. Based on the difference of curvature distribution between hillslope and valley, Lashermes et al. [2007] extracted the threshold from the curvature q-q plot. *Passalacqua et al.* [2010b] and Sofia et al. [2011] utilized a similar approach; and Sofia et al. [2011] additionally used an openness threshold from the corresponding q-q plot. The existing methods for extracting skeletons were developed based on the curvature of individual pixels. A pixel with a curvature that exceeds a threshold is considered part of the skeleton regardless of local terrain conditions. Occasionally, the curvature values at the upper sections of valleys and hillslopes may coincide. A pixel with a relatively small positive curvature may be a part of the valley skeleton or hillslope, and it is impossible to differentiate this based only on the curvature of the pixel. Therefore, it is necessary to consider local terrain conditions when extracting the skeleton. In this chapter, a systematic approach is proposed to extract valley and ridge skeletons considering curvature and local terrain conditions.

# CHAPTER 2: CHANNEL NETWORK EXTRACTION

Several methods have been proposed to delineate channel network from Digital Elevation Models (DEMs). These methods often require a channel initiation threshold such as contributing area [*O'callaghan and Mark*, 1984b; *Band*, 1986; *Tarboton et al.*, 1991], slope-area [*Montgomery and Dietrich*, 1988; *Willgoose et al.*, 1991; *Dietrich et al.*, 1992b; *Dietrich et al.*, 1993a; *Ijjasz-Vasquez and Bras*, 1995], or the Strahler's [1952] order [Peckham, 1995]. In methods based on contributing area, all pixels with upslope area greater than a pre-defined threshold are labeled as channelized. The upslope area is computed by flow directions from the D8 [*O'callaghan and Mark*, 1984b], the $D_\infty$ [*Tarboton*, 1997b], or the MDF [Quinn et al., 1991] algorithms. Methods based on slope-area utilize a threshold for a function of upslope area (A) and local slope (S) (e.g., $\beta A^m S^n$ where $\beta$, m and n are constants) to delineate channel network. Alternatively, using order as the channel initiation threshold, a section with a Strahler's order higher than a pre-defined threshold is identified as channelized. Orlandini et al. [2011] assessed these three types of channel initiation thresholds and concluded that their performance depends on the resolution of the DEM as well as catchment geology, topography and morphology.

Recently, the availability of high resolution DEMs (i.e., $\leq$ 3m) has paved the way towards another class of methods that utilize topographic attributes such as curvature [*Lashermes et al.*, 2007; *Passalacqua et al.*, 2010b; *Sofia et al.*, 2011; *Pelletier*, 2013], openness [Sofia et al., 2011], and slope direction [Lashermes et al., 2007] to extract channel network. The idea of using curvature in channel delineation originates from the traditional

contour crenulation method [Strahler, 1953; Morisawa, 1957; Pelletier, 2013]. The general procedure used by these methods includes the following four steps: 1) filter the DEM; 2) calculate the topographic features (e.g., curvature) from the filtered DEM; 3) extract the channel skeleton by applying either a user-defined or automatically-derived threshold for the topographic feature; and 4) identify and connect the channel heads to generate the channel network.

In particular, after computing the slope and curvature on a Gaussian-filtered DEM [Mallat, 1989], Lashermes et al. [2007] extracted the valley network based on a spatially constant curvature threshold, defined as the deviation point from a normal distribution in the curvature q-q plot. Similarly, a slope direction change threshold was also obtained from its corresponding q-q plot to delineate the channel network.

*Passalacqua et al.* [2010b] developed GeoNet by filtering the DEM using the Perona-Malik nonlinear diffusion filter, identifying a curvature threshold for the transition from hillslope to valley at the deviation point of the curvature q-q plot from a normal distribution, and constructing the valley skeleton. Subsequently, the channel skeleton was defined as the pixels in valley skeleton with an upslope area more than a user-defined contributing area threshold called "skeleton thinning parameter". The channel heads were detected and connected to the outlet following the minimum geodesic distance defined as the inverse of the weighted summation of upslope area and curvature. Passalacqua et al. [2012] studied the performance of GeoNet when extracting channel networks in flat and human-impacted landscapes and suggested using Laplacian rather than geometric curvature in those areas. GeoNet requires three user-defined parameters including the time of forward diffusion (i.e.,

the number of iterations) for filtering the DEM, the contributing area threshold for thinning the skeleton, and the size of the search box for identifying channel heads [Passalacqua and Foufoula-Georgiou, 2015]. *Sangireddy et al.* [2016a] eliminated the size of the search box by setting it equal to the median hillslope length and suggested using 50 iterations for smoothing the DEM.

Based on the statistical analysis of minimum curvature [Evans, 1979] and openness [Yokoyama et al., 2002], Sofia et al. [2011] determined the optimal kernel size for filtering DEMs. The openness and minimum curvature were normalized using thresholds derived from their corresponding q-q plots. The upslope area from the MFD algorithm was weighted by the normalized curvature and openness to enhance the contributing area of the convergent pixels. Channelized pixels were defined as those with an upslope area greater than the average value.

Applying the optimal Wiener filter [Press et al., 2007] for smoothing the DEM, Pelletier [2013] extracted the channel skeleton and channel heads by a user-defined curvature threshold. Instead of geometric or Laplacian curvature, Pelletier [2013] used contour curvature to quantify the surface convergence. The channel network was extracted by routing a unit discharge from the channel heads and then deleting discontinuous patches using a parameter that specifies the minimum flow in each pixel.

More recently, Clubb et al. [2014] developed the DrEICH method for locating channel heads based on the longitudinal profile of channels and hillslopes after extracting the initial network using a curvature threshold (i.e., 0.1 $m^{-1}$).

Existing methods for locating channel heads utilize various types of thresholds which are usually treated as spatially constant in a catchment, although they may vary due to the spatial heterogeneity of topography, soil and vegetation [Orlandini et al., 2011]. The developed method for mapping channel heads in this chapter is based on the fact that channels and valleys have fundamental geomorphologic differences. Channels have V or U-shaped cross-sections with well-defined banks [Montgomery and Dietrich, 1989], while cross-sections in unchannelized valleys are wide with no confining banks.

This extracted valley network in pervious chapter is used to spatially constrain the search for channel heads. Channel heads are extracted for each 1$^{st}$-order valley based on the shape of the contours, which reflects the signature of the corresponding cross-sections including the banks. An unsupervised algorithm based on K-means clustering [Macqueen, 1967] is used to classify the contours of each tributary as channelized or unchannelized based on the similarity of their shapes. The transition point from unchannelized to channelized contours is interpreted as the channel head. The proposed clustering approach has two main advantages: 1) instead of a point attribute (e.g., curvature), the entire cross-section from bank to bank is utilized to detect channel heads; and 2) the channel head identification is performed independently for each tributary using an unsupervised clustering approach; therefore, the method does not require a spatially constant channel initiation threshold (e.g., curvature or contributing area).

## 2.1 Cross-section profile and contours

The signatures of channel and valley cross-sections are reflected in the contours. This is demonstrated in a synthetic landscape (Figure 7) constructed for specified cross-sections of upslope, valley and channel. The upslope cross-section (i.e., $z_u$) is defined as a constant elevation (i.e., $H_u$). The valley cross-section is generated by a quadratic function represented in equation (8):

$$z_v(x) = \frac{4d_v}{B^2}x^2 - d_v \tag{8}$$

where $d_v$ and $B$ are the depth and width (i.e., equivalent to the width of the region) of valley, respectively (see Figure 7c). The channel cross-section is defined as a differentiable piecewise quartic function shown in equation (9):

$$z_c(x) = \begin{cases} -\frac{164d_c}{{w_c}^4}x^4 + \frac{8d_c}{{w_c}^2}x^2 - (d_c - h_b) & |x| \le \frac{w_c}{2} \\ -\frac{164h_b}{(B-w_c)^4}\left(\frac{B}{2} - |x|\right)^4 + \frac{8h_b}{(B-w_c)^2}\left(\frac{B}{2} - |x|\right)^2 & |x| > \frac{w_c}{2} \end{cases} \tag{9}$$

The first statement of equation (9) describes the cross-section of channel within the banks and the second statement represents the cross-section from the peak of the banks to the edges. In equation (9), $w_c$ and $d_c$ are the width and depth of the channel, respectively. $h_b$ represents the height of the channel banks relative to the elevation at the edge (see Figure 7d).

As shown in Figure 7a, the span of the domain along the y-axis is $L$ and consists of three sub-regions: downstream, transition, and upstream with lengths of $L_d$, $L_t$, and $L_u$, respectively. Starting from the top, the upslope cross-section evolves linearly in space into the valley cross-section moving from the upper edge (i.e., $y = L$) toward $y = L - L_u$.

Similarly, the cross-section in the transition changes gradually to the channel cross-section moving from $y = L - L_u$ to $y = L_d$. The downstream part represents the strongly channelized section in which the shape of cross-section is constant.

Having the upslope (i.e., $z_u$), valley (i.e., $z_v$), and channel (i.e., $z_c$) cross-sections, the elevation at any location $(x, y)$ is calculated as the weighted average of the elevations in the three cross-sections (equation 10.1). The weight coefficients are computed based on the distance (along the y-axes) of each point from two surrounding cross-sections (equation 10.2-4):

$$z(x,y) = w_u(y)z_u(x) + w_v(y)z_v(x) + w_c(y)z_c(x) + H_u - S(L-y) \tag{10.1}$$

$$w_u(y) = \begin{cases} \frac{L_u - L + y}{L_u} & y \geq L - L_u \\ 0 & Otherwise \end{cases} \tag{10.2}$$

$$w_v(y) = \begin{cases} \frac{L-y}{L_u} & y \geq L - L_u \\ \frac{y - L_d}{L_t} & L_d \leq y < L - L_u \\ 0 & Otherwise \end{cases} \tag{10.3}$$

$$w_c(y) = \begin{cases} \frac{L_t + L_d - y}{L_t} & L_d \leq y < L - L_u \\ 1 & y < L_d \\ 0 & Otherwise \end{cases} \tag{10.4}$$

where $S$ is the slope along the y-axes; $z_u$, $z_v$, and $z_c$ refer to the elevations of upslope, valley and channel cross-sections, respectively.

To investigate the signature of cross-sections on the contours, three synthetic 1-m DEMs were generated using different channel cross-sections and fixed upslope and valley cross-sections. The parameters that describe upslope and valley cross-sections were set to $B = 100\,m$, $L = 200\,m$, $L_u = 50\,m$, $H_u = 100\,m$, $d_v = 0.5\,m$, and $S = 0.1$, and were kept

constant in all generated DEMs to isolate their effects on the contours. In the first DEM, a channel was added using $d_c = 1\ m$, $w_c = 40\ m$, and $h_b = 0$ m. In this case, the transition length $L_t = 150\ m$ was used. The corresponding contours in Figure 7e show a slight signature of the channel banks, which are highlighted as the dark color in the curvature color map representing negative values. Using the same transition length ($150\ m$) and adding a sharper channel by setting $d_c = 2\ m$, $w_c = 40\ m$, and $h_b = 1\ m$ (Figure 7c), the change of the contours is enhanced as shown in Figure 7f. Figure 7g shows the contours using a similar setup for the channel cross-section and smaller transition length ($L_t = 50\ m$).

This synthetic example demonstrates how the contours change from valley to channel sections. Channelized contours have positive curvature at the channel's centerline and negative curvature at the banks. In contrast, unchannelized contours have small positive curvature with no detectable negative curvature due to the absence of banks. Figure 8 shows the difference in the shapes of channelized and unchannelized contours in a natural landscape located at Indian Creek, OH.

In the next section, an unsupervised algorithm based on K-means clustering is proposed to classify the contours in each tributary as either channelized or unchannelized. The transition from the unchannelized to channelized contours is identified as the channel head.

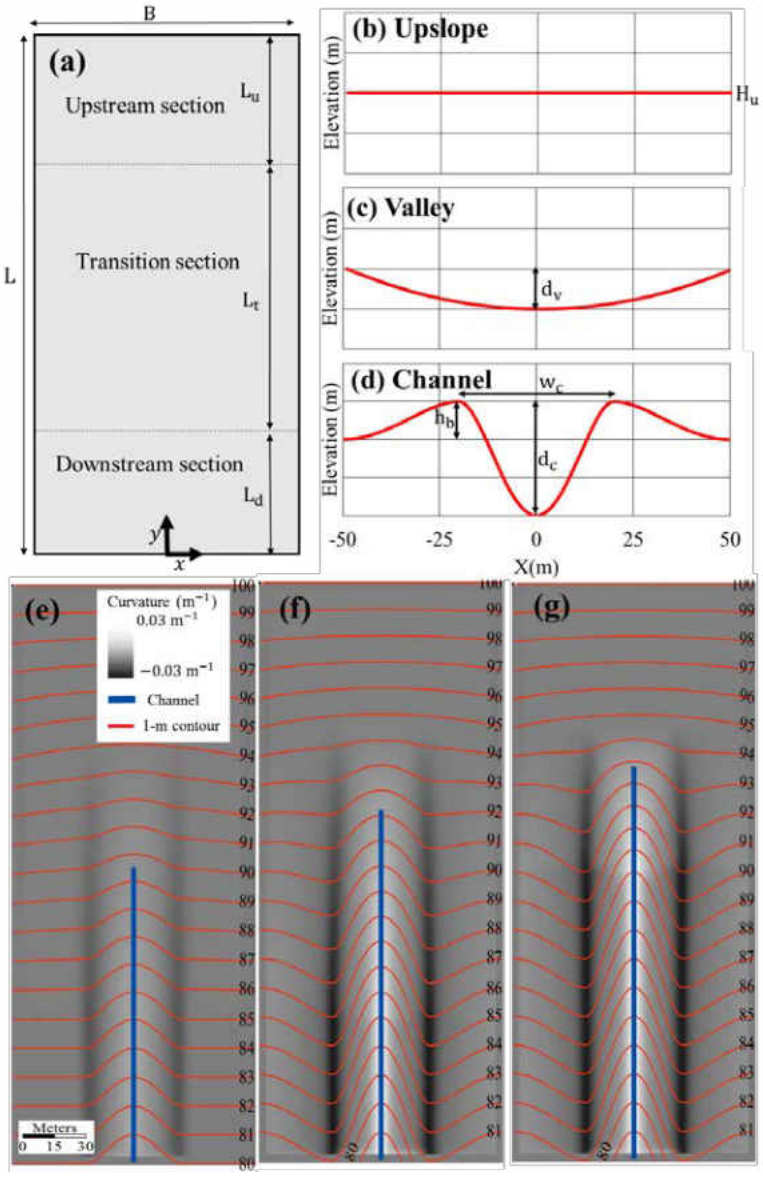


Figure 7. (a) Location of upslope (b), valley (c), and channel (d) cross-sections in the synthetic DEMs. (e), (f), and (g) Curvature and 1-m contours for synthetic DEMs. The numbers are the contour elevations in meters. The imposed channel cross-sections with well-defined banks resulted in sharp signatures in contours as highlighted by the dark background color (negative curvature).

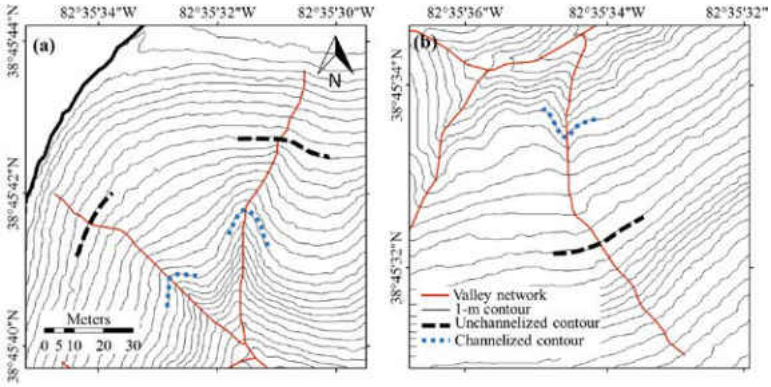


Figure 8. Examples of channelized and unchannelized contours in a natural landscape (Indian Creek, OH).

## 2.2 K-means clustering for channel head identification

K-means clustering [Macqueen, 1967] is an unsupervised classification algorithm to solve a clustering problem given as the minimization of the overall distance between points and the centroid of their corresponding clusters:

$$Min \sum_{j=1}^{J} \sum_{i=1}^{N^j} \left\| p_i^j - c_j \right\| \tag{11}$$

where $J$ is the number of clusters; $N^j$ is number of points in cluster j; and $p_i^j$ is the $i^{th}$ member of cluster $j$ and $c_j$ is its centroid. Traditional K-means clustering is initiated by randomly assigning each point to one of the clusters. Afterwards, the centroid of each cluster is calculated as the average location of all the points in that specific cluster. Then, all the data points are reassigned to the closest centroid and the centroids of all clusters are updated. This procedure is followed until the clusters converge.

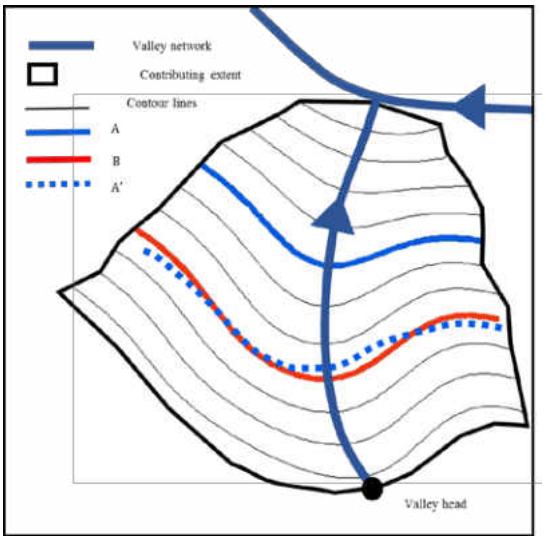


Figure 9. Example of 1st-order valley with $N_C$ equally-elevated contours created within the contributing extent. The upper bound of the contributing extent is constrained by the valley head elevation. The dissimilarity of contours is quantified based on their absolute orientation. For example, when comparing A and B, $A$ is reoriented toward B based on equation (12) forming the new contour $A'$. The dissimilarity index between $A$ and $B$ ($DS_{AB}$) is calculated as the root-mean-square (RMS) difference between $A$' and $B$.

Typically, the K-means method deals with points and clustering is done based on the distance between points. In this chapter, the contours in a tributary are classified into two clusters (channelized and unchannelized) based on their shapes. The dissimilarity ($DS$) of two contours is defined as the minimum root-mean-square (RMS) difference of one's best orientation relative to the other. Figure 9 shows an example of computing the dissimilarity index (i.e., $DS_{AB}$) between contours $A$ and $B$. Each contour is represented by a $2 \times M$ matrix containing $M$ equally-distanced $(x, y)$ pairs (i.e., points). The best orientation of A to B, denoted as $A'$, is obtained by translating, rotating and scaling $A$ so that the RMS difference between $A'$ and $B$ (i.e., $\|B - A'\|$) is minimized:

$$\begin{aligned} &Min\ \|B - A'\| \\ &st.\ A' = s \times R \times A + T \times U \end{aligned} \tag{12}$$

where $s$ is the scale factor; $R_{2\times2}$ is the rotation matrix; $T_{2\times1}$ is the translation vector; and $U_{1\times M}$ is the unit (i.e., all-ones) matrix. $A'$ represents the scaled, rotated and translated $A$. Horn [1987] developed a closed-form solution for the absolute orientation by solving this least-squares problem. In this solution, rotation is represented by quaternions and is similar to a rotation matrix in plane space. Translation represents the distance between the centers of $B$ and the scaled and rotated $A$. The scale is given by the ratio of RMS deviation (i.e., which is an indicator of the length) of A and B from their centers. The RMS difference obtained from equation (12) is interpreted as the dissimilarity between A and B ($DS_{AB}$).

Based on traditional K-means clustering and using the best orientation approach to quantify the dissimilarity of contours, the following clustering method is developed. The presented algorithm minimizes the dissimilarity index of contours in each cluster. The outcome of this algorithm is a transition contour (i.e., equivalently the elevation of the transition contour) that delineates the boundary between channelized and unchannelized sections. Therefore, the contours with elevation lower than or equal to the transition contour belong to the channelized cluster and the rest are unchannelized.

For each valley tributary, the total contributing extent is extracted using the adjusted flow directions. The upper bound of the extent is constrained by the valley head elevation as shown in Figure 9. $N_C$ equally-elevated contours are then generated within the contributing extent. Therefore, the contour interval would be $\frac{\Delta E}{N_C - 1}$, where $\Delta E$ is the relief in the

contributing extent. Higher values of $N_C$ indicate a more detailed representation of the terrain and higher computational load.

To initiate the clustering, a contour ($l$) with elevation $E_l$ is selected randomly as the transition contour. All contours having elevation less than or equal to $E_l$ are initially assigned to the channelized (C) cluster (equation 13.1) and all contours with elevation higher than $E_l$ are considered unchannelized (UC) (equation 13.2):

$$C = [j | E_j \leq E_l] \tag{13.1}$$

$$UC = [j | E_j > E_l] \tag{13.2}$$

The centroids of the two clusters are calculated by averaging the coordinates of all contours in each cluster:

$$X^C{}_i = \frac{\sum_{j \epsilon C} X_j}{|C|} \quad i = 1 \dots M \tag{14.1}$$

$$Y^C{}_i = \frac{\sum_{j \epsilon C} Y_j}{|C|} \quad i = 1 \dots M \tag{14.2}$$

$$X^{UC}{}_i = \frac{\sum_{j \epsilon UC} X_j}{|UC|} \quad i = 1 \dots M \tag{14.3}$$

$$Y^{UC}{}_i = \frac{\sum_{j \epsilon UC} Y_j}{|UC|} \quad i = 1 \dots M \tag{14.4}$$

where M is the number of points in each contour; $|C|$ ($|UC|$) is the number of channelized (unchannelized) contours. ($X^C{}_i$ , $Y^C{}_i$) and ($X^{UC}{}_i$, $Y^{UC}{}_i$) are the coordinates of the i$^{th}$ point of the average contour (i.e., centroid) representing channelized and unchannelized clusters, respectively.

For any contour $j$ located at the border of two clusters, the dissimilarity index of contour $j$ to the centroid of each cluster is calculated using equation (12). Contour $j$ is said

to be located at the border of the two clusters if it belongs to the channelized cluster and its elevation is the maximum among all channelized contours; or it belongs to the unchannelized cluster and its elevation is the minimum among all unchannelized contours. The contour $j$ is then assigned to the cluster with the smaller dissimilarity index. The process of identifying cluster centroids (equation 14) and reassigning the bordering contours is repeated until no change occurs in the clusters' membership. The transition contour ($\mathcal{J}$) is determined to be a member of the channelized cluster with the maximum elevation denoted by $E_{\mathcal{J}}$.

Since the outcome of the clustering process is sensitive to the random initial guess, the clustering is repeated $I$ times. This yields the vector $V_{1\times \mathrm{I}}$ that represents the number of times (out of $I$ iterations) the clustering converges to any contour. Finally, the transition elevation from an unchannelized to channelized section ($E^*$) is calculated as the weighted average of contour elevations using $V$ as the weight. The contours that have been selected as the transition contour for less than $0.1 \times I$ times are discarded in this calculation:

$$E^* = \frac{\sum_{j|V_j>0.1\times I} V_j E_j}{\sum_{j|V_j>0.1\times I} V_j} \tag{15}$$

It should be noted that the relative orientation of contours affects the centroid contours in equation (14). However, any effects caused by the contour orientations (i.e., translation, scale and rotation) is compensated for in the dissimilarity step. The only parameter used in channel network extraction is the number of contours in each valley tributary ($N_C$). $N_C = 30$ was used for the results presented in this chapter; however, the sensitivity to $N_C$ is presented in Section 3.3.

The presented clustering algorithm was applied to the synthetic DEMs in Figure 7, and the extracted channels are shown by blue lines. To better demonstrate the performance of the clustering, the dissimilarity curves for the synthetic DEMs in Figure 7f and 6g are also shown in Figure 10. The dissimilarity curves represent the summation of dissimilarity within channelized and unchannelized clusters for any estimate of channel head elevation. Based on the proposed methodology, the minimum of this curve, identified by the clustering method, corresponds to the elevation of the channel head. As mentioned earlier, the channelized cross-section transitioned to unchannelized within 150 m for the DEM in Figure 7f. For the DEM in Figure 7g, this transition occurred within 50 m. The dissimilarity curves clearly reflect the difference between transition lengths. The dissimilarity curve for $L_t = 50\ m$ is relatively sharper around the minimum compared to the case when $L_t = 150\ m$. In the latter case, the quality of the DEM and the filtering parameters would have more impact on the clustering performance resulting in higher uncertainty in channel head location prediction.

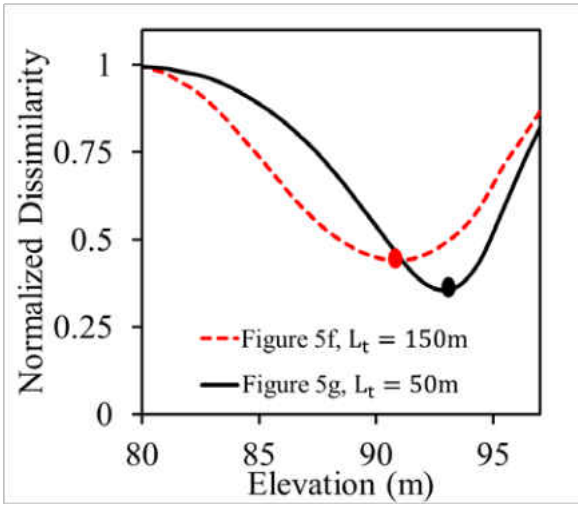


Figure 10. Normalized (by maximum) dissimilarity for estimates of the transition contour elevation for synthetic DEMs given in Figure 7f and Figure 7g. The minimum of these curves represents the transition from channelized to unchannelized section.

## 2.3 Results

After delineating the valley network, the contour clustering was performed for all 1st-order valleys (see Section 2.2.2) to locate the transition from unchannelized to channelized sections. The number of contours ($N_C$) was set to 30 for all catchments throughout this study. The extracted channel network and the location of mapped channel heads (reported in Clubb et al. [2014]) in Indian Creek are shown in Figure 11. The distributions of horizontal distance error between the mapped and predicted channel heads for three study catchments are presented in Figure 12. The distance error is negative if the mapped head is located downstream of the predicted one. The average error or net bias ($\overline{err}$), the standard deviation of error ($\sigma$), the number of heads that are mapped and predicted ($N_{MP}$), and the total number of mapped heads ($N_M$) are also reported for each case. Generally, the results in Indian Creek

and Mid Bailey Run are comparable to those reported in Clubb et al. [2014]. However, the extracted channel heads for Feather River are mainly located upstream of those found in the field and some of the mapped channels originate in the predicted 2nd-order valleys (Figure 13). Since the clustering was performed on the 1st-order valleys located upstream of the mapped heads, a relatively high negative error in channel heads' locations is observed in Feather River.

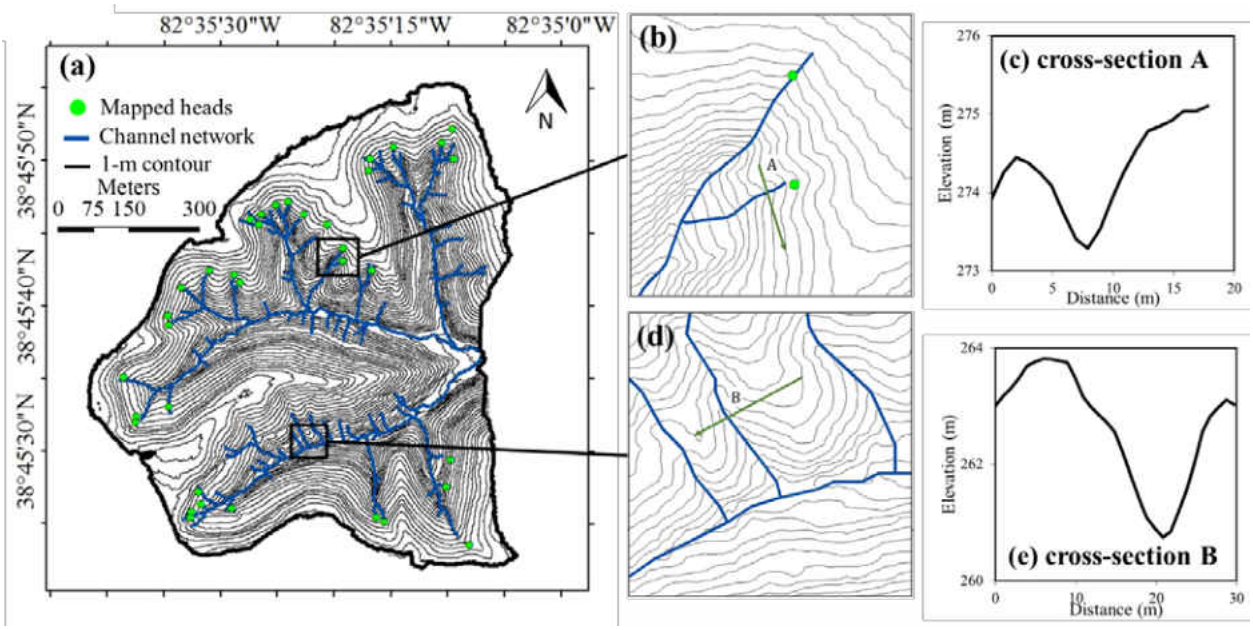


Figure 11. Comparison of mapped and predicted channel heads: (a) delineated channel network and the mapped channel heads in Indian Creek; (b) a zoomed-in area including two mapped and predicted channels; (c) cross-section at A; (d) area with three unmapped channels where the contours clearly indicate strong crenulations; and (e) cross-section with well-defined banks at B.

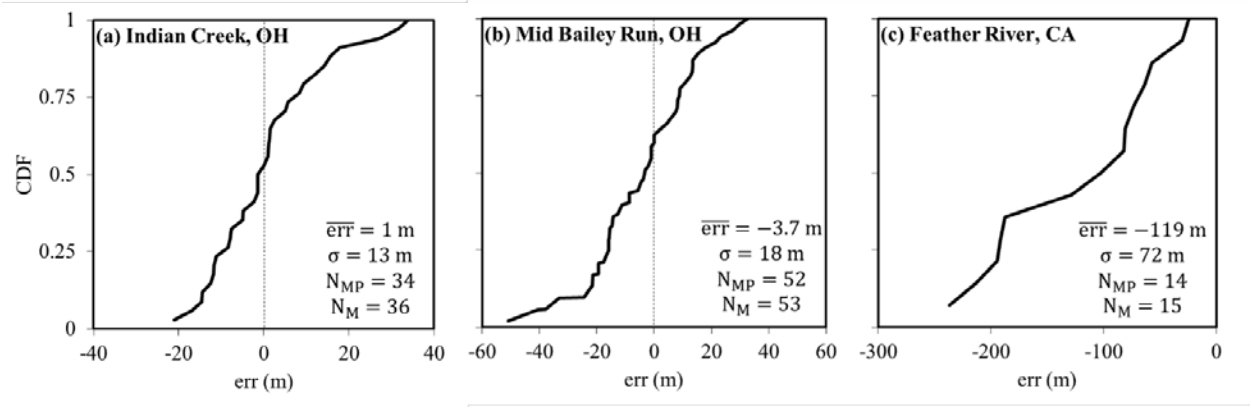


Figure 12. Distribution of error between the mapped and predicted channel heads in (a) Indian Creek (b) Mid Bailey Run, and (c) Feather River. $\overline{err}$ and $\sigma$ refer to the average and standard deviation of distance error. The total number of mapped heads ($N_M$), the number of mapped and predicted heads ($N_{MP}$) are also reported.

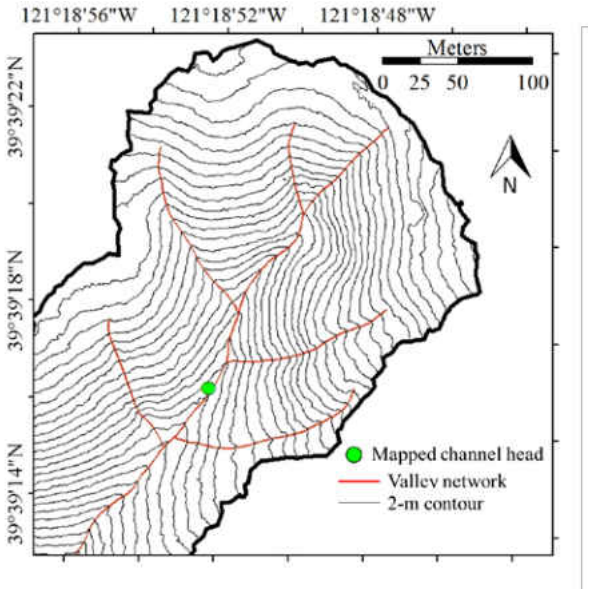


Figure 13. Example of mapped channelled heads located in the 2nd-order predicted valley in a subcatchment of Feather River. The presence of contour crenulations suggests the existence of channels upstream of the mapped head.

### 2.3.1 Sensitivity analysis

The sensitivity of the presented method to the parameters for extracting valley and channel networks was assessed for the Indian Creek catchment. In total, the proposed method includes parameters for filtering the DEM (time of forward diffusion, $T_F$), valley network extraction (connecting threshold, $C_T$), and channel head extraction (number of contours, $N_C$).

As shown in Figure 14a, Figure 14b, and Figure 14c, the proposed method performed robustly for various values of the parameters. In 13 out of 15 sensitivity tests, the distance error remained under 2 m and the standard deviation of error did not exceed 15 m. None of the parameters systematically altered the location of predicted channel heads; whereas, when using a user-defined curvature (as in Pelletier [2013]) or contributing area threshold for skeleton thinning (as in *Passalacqua et al.* [2010b]), the parameter systematically moves the predicted channel heads upstream or downstream as shown by the sensitivity analysis in Clubb et al. [2014].

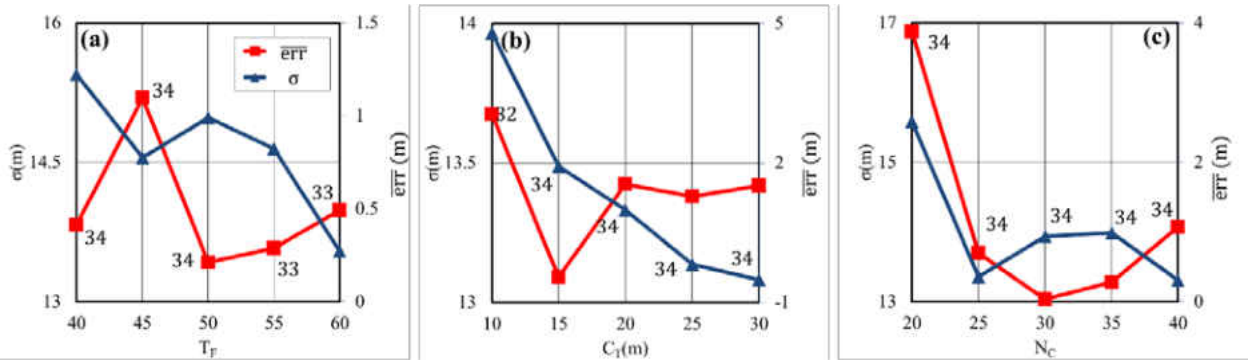


Figure 14. Sensitivity of the proposed method in Indian Creek to (a) the time of forward diffusion ($T_F$), (b) the connecting threshold ($C_T$), and (c) the number of contours ($N_C$) in terms of average and standard deviation of distance error. The number of heads that were mapped and predicted are shown for each parameter value.

The only parameter related to the channel head prediction is the number of contours ($N_C$). As shown in Figure 14c, increasing the number of contours does not necessarily enhance the performance of the method with respect to the average and the standard deviation of error. To better understand the sensitivity of the method to $N_C$, the standard deviation of distance error ($\sigma_{err}$) at each channel head was studied. For each pair of mapped and predicted channel heads, $\sigma_{err}$ is the standard deviation of four values of distance errors, each of which corresponds to one value of $N_C$. As shown in Figure 15, for more than 85% of the heads $\sigma_{err}$ was less than 3.5 m, indicating only minor alteration of the predicted channel head location for various values of $N_C$.

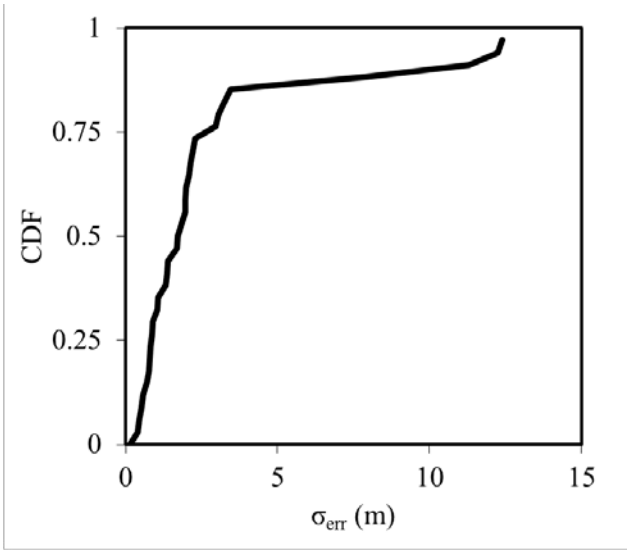


Figure 15. Distribution of standard deviation of distance error ($\sigma_{err}$) at individual heads, which represents the change in predicted head location caused by alteration of $N_c$ in Indian Creek.

### 2.3.2 Comparison to other methods

Clubb et al. [2014] studied three state-of-the-art channel delineation methods in the same catchments used here. These methods include GeoNet proposed by *Passalacqua et al.* [2010b], Pelletier proposed by Pelletier [2013], and DrEICH proposed by Clubb et al. [2014]. Since all the channel heads were mapped only in Indian Creek and Mid Bailey Run, the discussions here focus on these two study sites. The average distance error ($\overline{err}$), standard deviation of distance error ($\sigma$), reliability ($r$), sensitivity ($s$), and percentage error of mapped and predicted channel densities ($\varepsilon_D$) were used to compare the performance of the methods [Orlandini et al., 2011; Clubb et al., 2014].

$$r = \frac{\sum TP}{\sum TP + \sum FP} \tag{16.1}$$

$$s = \frac{\sum TP}{\sum TP + \sum FN} \tag{16.2}$$

$$\varepsilon_D = 100\frac{D_M - D_P}{D_M} \quad (16.3)$$

where true positive (TP) heads are both predicted and mapped; false positive (FP) heads are predicted but not mapped; and false negative (FN) heads are mapped but not predicted in the same 1st-order basin. $\sum TP$, $\sum FP$, and $\sum FN$ represent the number of heads in each class. $D_M$ and $D_P$ are the mapped and predicted channel densities.

Table 1 summarizes the performance of DrEICH, GeoNet, Pelletier, and the proposed method in Indian Creek and Mid Bailey Run. The results for DrEICH and Pelletier methods were taken from Clubb et al. [2014], and the indices for GeoNet were measured using parameters suggested by Passalacqua and Foufoula-Georgiou [2015] (i.e., skeleton thinning parameter of 200 $m^2$ with Laplacian curvature).

The proposed method had equal or better performance compared to the best of the existing methods in three indices for Indian Creek and one index for Mid Bailey Run. In addition, two indices ($\overline{err}$ and $\sigma$) in Mid Bailey Run were comparable to the best performance achieved by existing methods. Considering the sensitivity analysis (Figure 14) and the results presented in Table 1, the proposed method performed well in terms of $\overline{\text{err}}$, σ, and s; however, it resulted in negative $\varepsilon_D$, as other methods did, and smaller $r$ which implies overestimation of channel network. Although some predicted heads were not mapped in the field, they often satisfy the basic definition used to delineate channels, i.e., convergent surface confined by well-defined banks. Figure 11d shows a zoomed-in area in Indian Creek with three unmapped channels. The contours clearly show strong crenulations and the cross-section at B, shown in Figure 11e, is channelized with well-defined banks. For comparison, contours and cross-section in a mapped channel are shown in Figure 11b and Figure 11c.

Table 1. Performance of DrEICH, GeoNet, Pelletier and the proposed method in terms of the average error ($\overline{err}$), standard deviation of error ($\sigma$), reliability ($r$), sensitivity ($s$), and percentage error of mapped and predicted channel densities ($\varepsilon_D$) in Indian Creek and Mid Bailey Run.

| | Method | Indian Creek | Mid Bailey Run |
|---|---|---|---|
| $\overline{err}$ (m) | DrEICH* | 12 | 3 |
| | GeoNet** | -9 | 8 |
| | Pelletier* | 5 | -7 |
| | Proposed | 1 | -4 |
| $\sigma$ (m) | DrEICH* | 21 | 22 |
| | GeoNet** | 13 | 16 |
| | Pelletier* | 13 | 17 |
| | Proposed | 13 | 18 |
| $r$ | DrEICH* | 0.51 | 0.49 |
| | GeoNet** | 0.15 | 0.31 |
| | Pelletier* | 0.53 | 0.52 |
| | Proposed | 0.34 | 0.34 |
| s | DrEICH* | 0.75 | 0.83 |
| | GeoNet** | 0.58 | 0.77 |
| | Pelletier* | 0.72 | 0.74 |
| | Proposed | 0.91 | 0.77 |
| $\varepsilon_D$ | DrEICH* | -17% | -48% |
| | GeoNet** | -34% | -40% |
| | Pelletier* | -26% | -38% |
| | Proposed | -35% | -34% |

* These results are from Clubb et al. [2014]
** Using thinning parameter of 200 $m^2$ with Laplacian curvature as suggested in Passalacqua and Foufoula-Georgiou [2015]

### 2.3.3 Channel initiation

The advantage of the proposed method over the existing curvature-based approaches is that the channel head prediction is performed separately for each tributary. The channel head is identified based on the shape of the contours; therefore, no spatially constant

curvature threshold is required. Channel initiation criteria such as upslope area, slope-area, order, and curvature were observed to be spatially variable within a catchment [Tarolli and Dalla Fontana, 2009; Orlandini et al., 2011; Clubb et al., 2014]. In addition, the magnitude of curvature is sensitive to the filtering method and the DEM resolution [Tarolli and Dalla Fontana, 2009], which makes it difficult to propose a single curvature threshold that works well across various landscapes. To avoid this, channel (or valley) initiation curvature thresholds based on the curvature statistics have been proposed [Lashermes et al., 2007; Tarolli and Dalla Fontana, 2009]. Although these thresholds vary from one catchment to another, they are constant within a single catchment.

Figure 16 shows the CDF of mapped and predicted channel head curvature in the study sites. Despite the relatively small size of the catchments, the curvature at the mapped channel heads varied considerably. For instance, the curvature at Indian Creek, the smallest catchment in this study, ranges from 0.006 to 0.1 $m^{-1}$ with an average of 0.053 $m^{-1}$ and a coefficient of variation (CV) of 54%. Therefore, it is a challenge to define a spatially constant curvature threshold for channel head identification.

The distribution of the curvature at the predicted channel heads along with their statistics are also shown in Figure 16. In Feather River, the curvature at the predicted channel heads is smaller compared to the mapped heads. This is consistent with the negative distance error of predicted channel heads (Figure 12) since the curvature usually decreases moving upstream in the valleys.

To further analyze the capability of the proposed method to capture the spatial variation of curvature at channel heads, the relationship between curvature at the mapped

and predicted heads in Indian Creek and Mid Bailey Run is shown in Figure 17. The data points were binned along the horizontal axis using a 0.005 $m^{-1}$ bin size and the 25, 50, and 75 percentiles at each bin are presented. Figure 17 indicates relatively good agreement between the curvature at mapped and predicted heads, especially for mapped heads with curvature values between 0.03-0.09 $m^{-1}$.

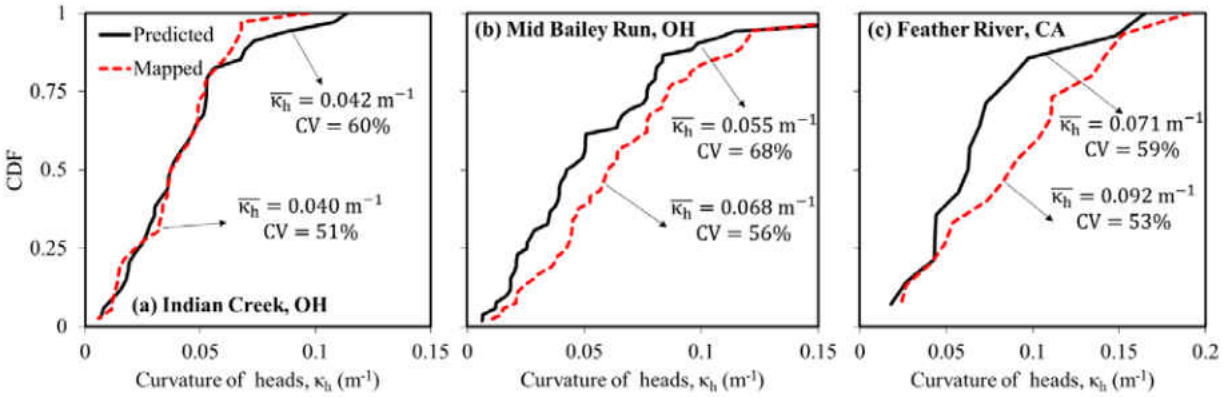


Figure 16. Distribution of curvature at the mapped and predicted channel heads in (a) Indian Creek (b) Mid Bailey Run, and (c) Feather River. The average and the coefficient of variation (CV) for each distribution are given.

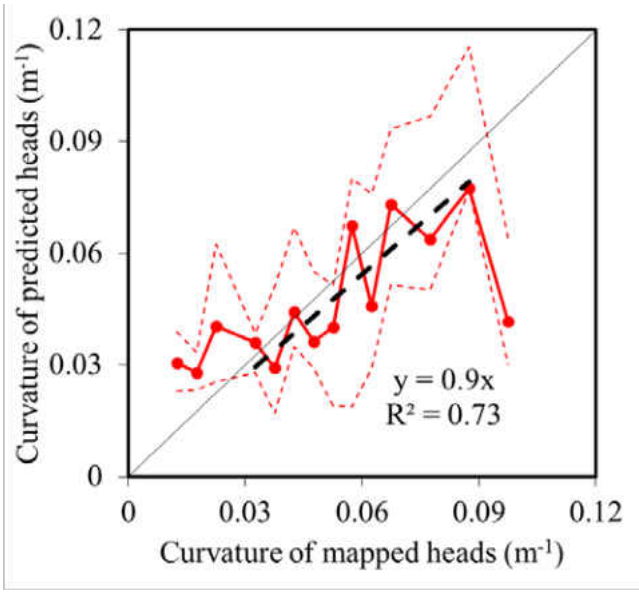


Figure 17. Curvature at the mapped versus predicted channel heads. The data points were binned along the horizontal axis using a 0.005 $m^{-1}$ bin size and the 25, 50, and 75 percentiles at each bin are presented. The dashed black line represents the linear fit in the range of 0.03-0.09 $m^{-1}$ which indicates a strong linear correlation with $R^2 = 0.73$.

## 2.4 Conclusions

Valley and channel networks are important geomorphologic features of catchments. Recently developed channel extraction methods utilize local curvature as the initiator of channels, i.e., the channel begins when the landscape is convergent enough and the convergence is measured by curvature. The channel initiation curvature threshold is assumed to be spatially constant; however, it has been shown to be unrealistic even in small catchments.

The basic definitions of channels and valleys were used to identify them in high-resolution DEMs. Channels are generally surrounded by well-defined banks that have a distinct signature in the contours. A new method was proposed to automatically extract

channel heads based on the clustering of contours, utilizing the information derived from the entire cross-section. The similarity-based clustering method eliminates the need for a spatially constant channel initiation threshold. The proposed method was able to capture the spatial variation of channel initiation curvature threshold.

The proposed method was applied to three study sites and performed well in terms of identifying small channels. 34 and 52 (out of 36 and 53) channel heads were identified in Indian Creek and Mid Bailey Run, respectively. The average and standard deviation of distance error between mapped and predicted channel heads were better or comparable to existing methods. None of the three parameters associated with the proposed method systematically altered the location of predicted channel heads; whereas, in the case of using spatially constant user-defined curvature (as used in Pelletier's method) or thinning contributing area (as used in GeoNet) thresholds, the parameter systematically moves the heads upstream or downstream.

The proposed method was also able to detect small-scale tributaries, but it overestimated the number of channel heads. In most cases, the predicted and unmapped channel heads satisfied the basic definition used to delineate channels, i.e., convergent surfaces confined by well-defined banks.

Some components of the proposed method (e.g., terrain segmentation and channel head identification) are more complex and computationally expensive compared to existing approaches. However, the complexity is acceptable in terms of producing a robust and physically-based method for automatic drainage network delineation. In particular, despite its solid physical foundations and robust performance, the contour clustering requires

greater computational effort compared to methods that employ spatially constant curvature thresholds.

The proposed method was developed for landscapes with minimal human impacts where there is a well-defined distinctions between unchannelized valleys and channels reflected in their corresponding cross-sections. The applicability of the proposed method to catchments with anthropogenic features and topographic gradients at the upper and lower ends of the spectrum will be investigated in future work.

Lastly, although the valley network extracted using the proposed method was used to delineate the channel network, the two steps are independent. Therefore, the valley network extracted from any of the existing methods can be used as the basis for channel network extraction using the proposed clustering approach. Alternatively, the extracted valley network from the proposed method can also serve as the basis for channel head identification using process-based techniques. Collectively, this presents an opportunity for the development of additional hybrid approaches that may be suitable for particular terrains.

# CHAPTER 3: WET CHANNEL EXTRACTION

Flowing channel networks expand in response to rainfall events and contract during streamflow recession periods. The temporal and spatial dynamics of wet channel networks are one of the key features for revealing the links between hydrology and geomorphology driven by climate mechanisms [*Abrahams*, 1984; *Wang and Wu*, 2013a] on hydrologic processes [Biswal and Marani, 2010], stream ecosystem expansion and contraction [Stanley et al., 1997], and spatial variability in stream chemistry [Zimmer et al., 2013; Mcguire et al., 2014]. Perennial streams, by definition, have continuous flow during years of normal rainfall [Meinzer, 1923]; whereas, temporary streams, including intermittent and ephemeral streams, cease flowing at one or more points in space and time along their course. Temporary streams support high biodiversity and important ecosystem processes [Acuña et al., 2014]. Studying the temporal dynamics of wet channels is also beneficial to advance surface-subsurface models [Kollet and Maxwell, 2006; Camporese et al., 2010], since it provides efficient means to validate the internal exchanges at the land surface interface. The ability of surface-subsurface models to reproduce the complex process of wet channel formation is important for long-term simulations under climate change scenarios. Therefore, understanding and monitoring these short-term changes in wet channel networks will benefit both hydrology and aquatic ecology. However, the data availability on the wetting and drying dynamics of temporary streams is limited. Streamflow gauges operated by United States Geological Survey (USGS) are generally sited on relatively large perennial streams and rivers.

Remotely sensed images from satellites have been used to identify the open water bodies and large rivers. Near-infrared (NIR) radiation is absorbed by water but reflected by vegetation and dry soil. This characteristic of NIR has been utilized to identify ponds and lakes [Work Jr and Gilmer, 1976]. Based on the reflectance of water and vegetation to NIR and green light, the normalized difference water index (NDWI) has been developed and used for differentiating water surface features from soil and vegetation [Mcfeeters, 1996; Xu, 2006]. Beeson et al. [2011] used night/day temperatures, as a proxy for soil moisture, from advanced spaceborne thermal emission and reflection radiometer (ASTER) images with 15 meter resolution to identify ephemeral and perennial stream reaches. Since headwater streams are typically narrower, shallower, and heavily vegetated, it is challenging to use satellite imagery to detect the water surface.

Airborne light detection and ranging (LiDAR) provides an opportunity to map wet channel networks. LiDAR has become an important technique to acquire topographic data at sub-meter resolution and accuracy [Marks and Bates, 2000; Bowen and Waltermire, 2002] and has been utilized to extract flow direction [*Tarboton*, 1997b; *Orlandini and Moretti*, 2009], channel networks [*Lashermes et al.*, 2007; *Orlandini and Moretti*, 2009; *Passalacqua et al.*, 2010b; *Orlandini et al.*, 2011; *Sofia et al.*, 2011; *Pelletier*, 2013; *Clubb et al.*, 2014], and topographic depressions [Le and Kumar, 2014] in the past. LiDAR has also been used to retrieve water surface information including flood inundation extent [Genc et al., 2005] and water levels and gradients [Magirl et al., 2005; Hopkinson et al., 2011]. As an active remote sensing technique, the airborne LiDAR sensor emits NIR laser pulses with a wavelength of 1064 nm that almost entirely absorbed by water. The infrared laser light is effectively

absorbed in the water column or reflected specularly away from the field view of the discrete echo recording system [Wolfe and Zissis, 1985; Brzank et al., 2008]. Recently, the green laser with a wavelength of 532 nm from a bathymetric airborne LiDAR sensor has shown the capability of penetrating the water surface to directly measure water depths in clear water environments [Höfle et al., 2009]. A key element of the LiDAR data stream is the signal intensity, which is a relative strength measurement of the return pulse by the LiDAR sensor. The signal intensity is lower from the water surface compared with land areas. The intensity characteristics of water surface have previously been used to derive water-land boundaries in river segments [Höfle et al., 2009]. With high airborne LiDAR acquisition altitudes and incidence angles, the intensities of water surface returns arriving at the receiver are too small to be detected. Therefore, laser shot dropouts may occur and the point density is typically lower on water surfaces [Höfle et al., 2009]. Even though bathymetric LiDAR in the green and infrared spectral bands have the ability to generate returns at water surfaces, point densities are lower than those of topographic LiDAR, affecting the minimum detectable size of water body systems [Hilldale and Raff, 2008; Mallet and Bretar, 2009].

Intensity information from single wavelength topographic LiDAR (i.e., NIR) systems has been used to map many types of water surfaces including rivers, wetlands, ponds, and lakes [Höfle et al., 2009; Smeeckaert et al., 2013; Wu et al., 2013]. Antonarakis et al. [2008] identified a water surface in a river segment when the height range of the returns is less than 0.5 m and an average intensity value in a local domain is less than 55 DN (digital number). Lang and Mccarty [2009] demonstrated the ability of LiDAR intensity data for mapping inundated areas beneath a forest canopy. Brzank et al. [2008] developed a supervised

classification method for identifying laser points on the water surface of the Wadden Sea using elevation, intensity, and 2D point density. These studies are successful in delineating water-land boundaries of large continuous water areas (i.e., geometrical assessment of water bodies).

The objective of this chapter is to extract wet channel networks at sub-meter resolution using the elevation and intensity information from the point cloud generated by topographic LiDAR systems which are now available to the public in many areas [Stoker et al., 2006]. Given the valley network delineated from LiDAR topographic data, the wet sections of the network are extracted based on signal intensity of ground returns. Wet pixels are identified along the valley network based on the frequency distribution and the gradient of intensity returns. Solely based on the intensity distribution, it is quite challenging to detect narrow and shallow streams since their intensity returns have relatively high variation. This challenge is addressed by utilizing the gradient of intensity to locate the transition from wet to dry pixels in the bank of small wet channels. The Lake Tahoe area is used as the case study due to the availability of high resolution LiDAR data with intensity information and two data acquisitions, separated by approximately two years, in some watersheds. The developed method provides an opportunity to map wet channel networks.

## 3.1 Study sites

Lake Tahoe is located in the high mountain area at the state border of California and Nevada. The lake covers 496 $km^2$ with a total drainage area of 1,310 $km^2$ [Dettinger, 2013]. The Lake Tahoe drainage basin is formed by geologic uplift that created the Carson Range on

the east and the Sierra Nevada on the west with an average surface elevation of 1,897 m above mean sea level. The area has cold and wet winters with an average temperature of -1 $^{o}$C in January and warm and dry summers with an average temperature of 18 $^{o}$C in June [Taylor and Beaty, 2005]. Mean annual precipitation on the west and east sides of the lake are 1400 mm and 670 mm, respectively. Precipitation mainly occurs as snow from November to April, and most runoff occurs during the spring snowmelt period from April to June [Coats and Goldman, 2001].

This study focused on five watersheds around Lake Tahoe as shown in Figure 18a. Four watersheds, including Blackwood Creek, Ward Creek, General Creek, and Trout Creek, are located in California; Incline Creek, where there are two streamflow gages, is located in Nevada. The human impacts and urbanization are minimal in these watersheds. The drainage area of the six USGS gages varies from 7.4 km$^2$ to 28.9 km$^2$ (Table 2). The climate aridity index, defined as the ratio of potential evaporation to precipitation, varies from 0.99 to 1.61 in these watersheds. They are covered by intact forest and shrub area; as an example, the forest and shrub land area in the Blackwood Creek watershed is 70% and 28%, respectively.

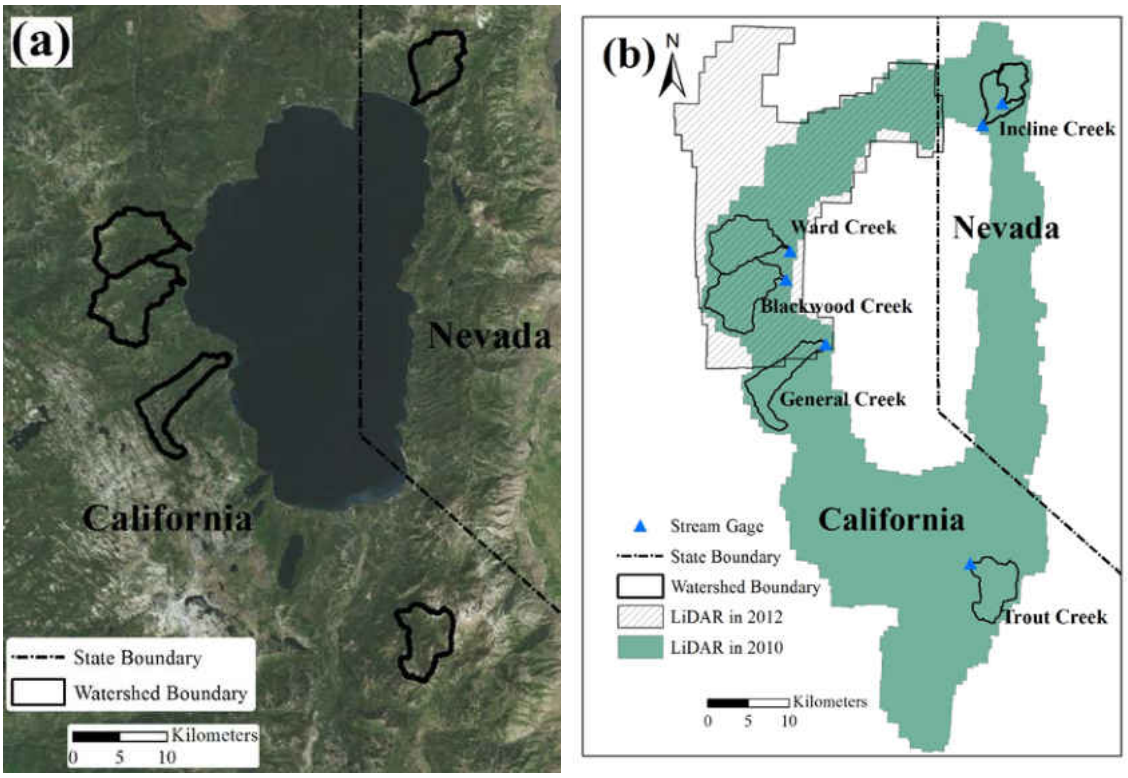


Figure 18. Map for the study sites. (a) Five study watersheds around Lake Tahoe. (b) Six streamflow gages and the spatial coverage of LiDAR data sets.

Table 2. USGS gage identification number, drainage area, streamflow and its exceedance probability during the LiDAR surveys for the study watersheds.

| Watershed | Gage Number | Drainage Area [km$^2$] | LiDAR Acquisition Date | Streamflow [m$^3$/s] | Streamflow Exceedance Probability [%] |
|---|---|---|---|---|---|
| **Blackwood Creek, CA** | 10336660 | 28.9 | 8/20/2010-8/23/2010 | 0.10±0.01 | 73 |
| | | | 6/20/2012-6/21/2012 | 0.52±0.01 | 40 |
| **Ward Creek, CA** | 10336676 | 24.9 | 8/14/2010 | 0.06 | 72 |
| | | | 6/20/2012-6/21/2012 | 0.27±0.01 | 43 |
| **General Creek, CA** | 10336645 | 19.2 | 8/20/2010-8/23/2010 | 0.02 | 95 |
| **Trout Creek, CA** | 10336770 | 19.1 | 8/23/2010 | 0.16 | 54 |
| **Incline Creek, NV** | 10336700 | 17.3 | 8/12/2010 | 0.10 | 66 |
| **Incline Creek, NV** | 103366993 | 7.4 | 8/12/2010 | 0.04 | 74 |

## 3.2 LiDAR and streamflow data

These watersheds are selected for this study based on the availability of streamflow observations and LiDAR data. Streamflow observations at the gages (Figure 18b) are obtained from the USGS National Water Information System. The USGS Center for LiDAR Information, Coordination and Knowledge (CLICK) provides LiDAR data tiled by USGS Quarter Quadrangles in LAS and ASCII format [Stoker et al., 2006]. The LiDAR data are obtained through the CLICK website (http://lidar.cr.usgs.gov, Last Accessed July 15, 2014). The ground returns of LiDAR data, in which vegetation and buildings are filtered out by the data provider, are used in this study.

As shown in Figure 18b, two sets of LiDAR data are available, one flown in 2010 and the other in 2012. The LiDAR data in 2010 (from August 11 to August 24) are acquired using a Leica ALS50-II LiDAR System. Each return (data point) includes a Global Positioning System (GPS) time stamp, spatial coordinates (X, Y, Z), intensity representing the strength of the reflected signal, flight line, scan angle, and return number (first/last return). The data are collected from an altitude of approximately 900~1300 m. The average spacing and average point density of irregularly-spaced LiDAR points for ground returns are 0.67 m and 2.26 points/$m^2$, respectively.

The LiDAR data in 2012 (from March 25 to June 29) are acquired using an Optech ALTM Gemini LiDAR system. The data are collected from an altitude of approximately 915 m. The average spacing and average point density of irregularly-spaced LiDAR points for ground return are 0.72 m and 1.94 points/$m^2$, respectively. The range of scan angle is $\pm$ 19°

and the vertical accuracy is 18 cm. The point cloud data are processed to derive the intensity map and the land surface topography using the QCoherent software LP360 for ArcGIS.

There is an overlap between two LiDAR data sets for Blackwood Creek and Ward Creek watersheds. Therefore, two snapshots of LiDAR data are available for these two watersheds and they are used to identify wet channel networks in 2010 and 2012 as described below. The LiDAR acquisition date(s) for each watershed are listed in Table 2. The acquisition dates cover four consecutive days for Blackwood Creek and General Creek watersheds in 2010 and one or two days for the others.

The streamflow and its associated exceedance probability during the LiDAR acquisition dates are listed in Table 2. All LiDAR data are acquired during hydrograph recession periods. For example, the rainfall and hydrograph for Blackwood Creek during the LiDAR acquisition periods are plotted in Figure 19. Streamflow declines during the recession period from June to September. The LiDAR surveys are performed at the recession stages in August 2010 (Figure 19a) and June 2012 (Figure 19b). Based on 53 years of daily streamflow records for Blackwood Creek, the exceedance probabilities during the LiDAR surveys are 73% in 2010 and 40% in 2012, respectively. As shown in Table 2, the exceedance probability of streamflow for all the snapshots is more than 40%. In particular, the exceedance probability for General Creek is 95%, indicating a low flow condition in which dry channels are expected.

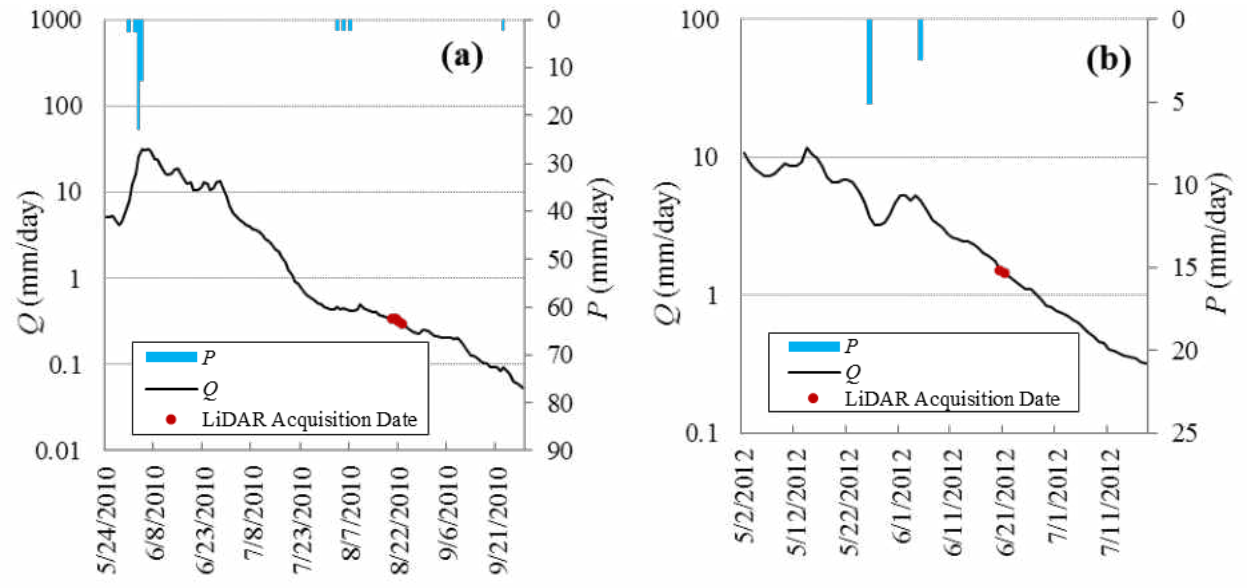


Figure 19. Rainfall and hydrograph for Blackwood Creek, and the LiDAR acquisition periods during (a) 8/20/2010-8/23/2010 and (b) 6/20/2012-6/21/2012.

### 3.3 Methodology and Demonstration

The signal intensity of ground returns is the main information used for identifying wet and dry channels. Intensity is usually represented in DN (digital number) units that are a digitized form of the amount of electromagnetic radiation received from a point on a surface. LiDAR intensity returns from water surfaces are usually lower than the intensity from the dry land because of the strong absorption of light energy by water. The point cloud returns for water surface are usually associated with low signal intensity, dropouts, and a high relative variation of intensity [Höfle et al., 2009]. The specular reflection from the water surface also contributes to low intensity of the signal. When the signal intensity is lower than a threshold, the data point is dropout processed by the data acquisition provider, leading to reduction in point density on the water surface. Figure 20a shows the 2010 intensity image

for a headwater catchment in the Blackwood Creek watershed; Figure 20b shows the 2012 intensity image in the same area. The intensity value varies from 1 DN to 215 DN for 2010 LiDAR and from 1 DN to 803 DN for 2012 LiDAR. As shown in Figure 20, the intensity in the wet channels is significantly lower than that on hillslopes and dry channels. The wet channel heads (i.e., upstream limits of wet channels) are identified visually and marked by green dots.

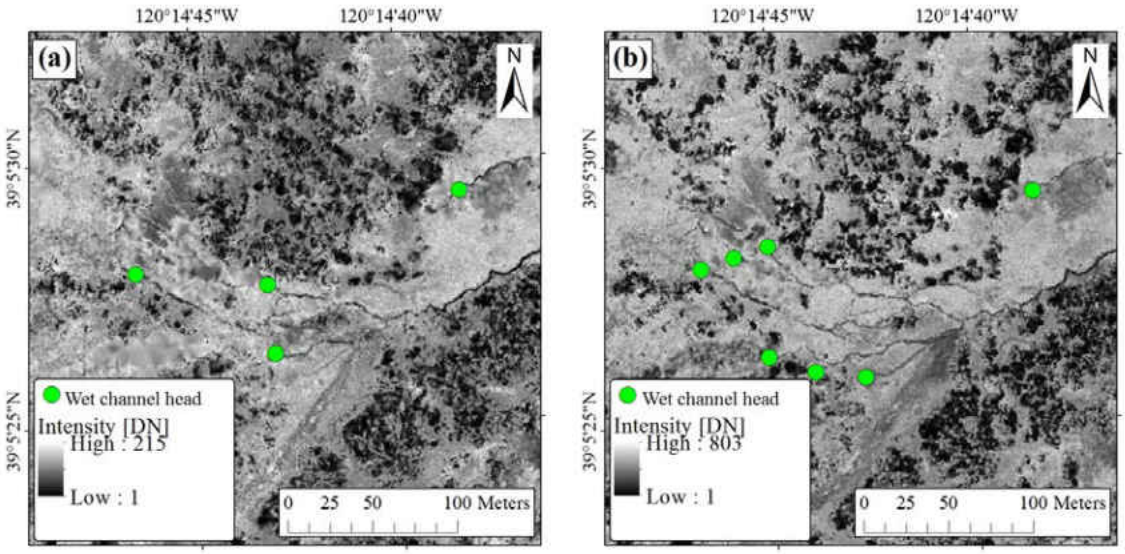


Figure 20. LiDAR intensity for a headwater catchment in the Blackwood Creek watershed during (a) 2010 and (b) 2012 surveys. The wet channel heads (i.e., upstream limits of wet channels) are identified visually and marked by green dots.

In this chapter, a systematic method is developed to extract wet channel networks based on both LiDAR intensity and the digital elevation model (DEM). The proposed method consists of the following six major steps: 1) masking dense vegetation in intensity maps based on elevations of ground surface and canopy (Section 3.1); 2) extracting valley extents from the LiDAR-based DEM (Section 3.2); 3) decomposing composite probability

distribution function (PDF) of intensity (Section 3.3); 4) detecting edges (i.e., high gradient pixels in intensity map) based on the local gradient of intensity (Section 3.4); 5) identifying wet pixels based on the thresholds determined from the decomposed PDFs and detected edges (Section 3.5); and 6) generating the wet channel network (Section 3.6). The step-by-step procedure of the proposed method is described below. The figures used to illustrate the method are based on the 2012 LiDAR from the Blackwood Creek watershed.

### 3.3.1 Masking dense vegetation in intensity maps

LiDAR point cloud data contains intensity returns from surfaces with different elevations. For instance, the LiDAR data in a vegetated area provides intensity from top of the canopy (Figure 21a) and the ground surface (Figure 21b). In order to identify wet channels, it is essential to use the return intensity from ground surface. As shown in Figure 21b, the intensity under canopy is relatively low and in the same range of those from wet surface, due to energy absorption by vegetation. This can be misleading for identifying wet channels, since some vegetated areas may be erroneously classified as wet surfaces. Here, to enhance the performance of wet channel identification, densely vegetated areas are masked from the intensity map. Similar to the intensity returns, the LiDAR data provided elevations at top of the canopy and the ground surface. The densely vegetated areas are identified as the locations where the canopy elevation ($h_c$) is significantly higher than the ground elevation ($h_g$). In other words, a pixel $p$ is marked as densely vegetated if the condition given in equation (17) is satisfied:

$$h_c(p) \geq h_g(p) + h_T \tag{17}$$

where $h_T$ is a parameter indicating the minimum height of canopy and is set to 2 m for the results presented here. Figure 22 shows the identified densely vegetated area in the Blackwood Creek watershed. The areas marked as densely vegetated are masked out from the intensity map and omitted for extraction of wet channels.

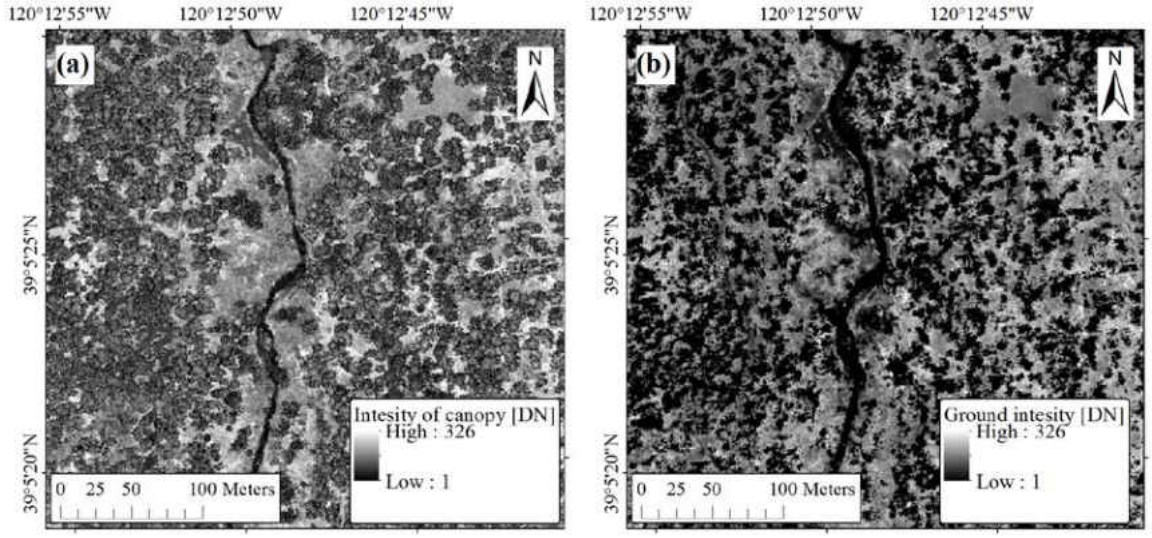


Figure 21. The intensity of returns from (a) the top of canopy and (b) the ground surface in the Blackwood Creek watershed based on 2012 LiDAR survey.

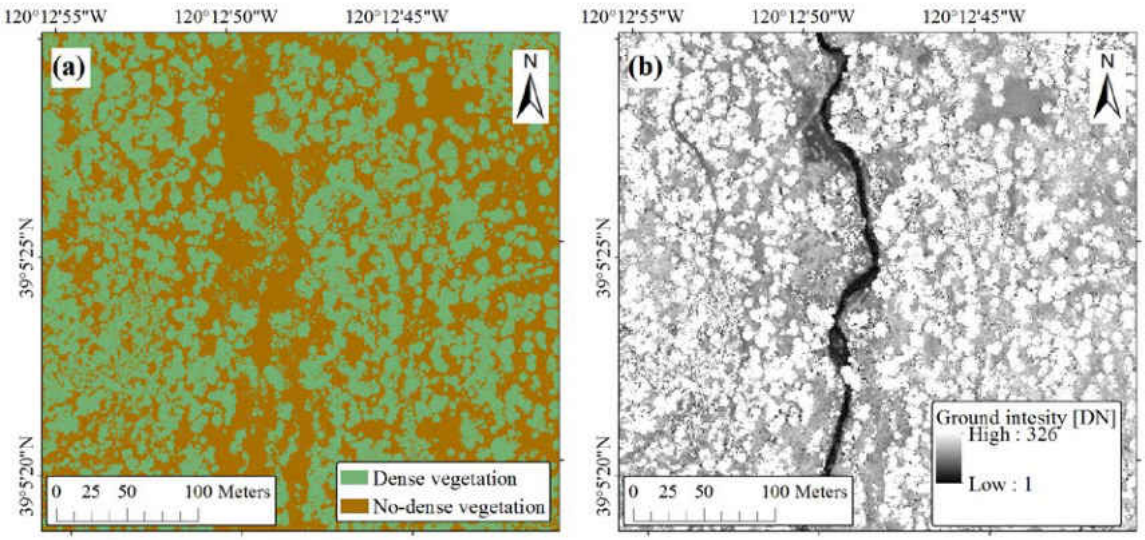


Figure 22. (a) The extent of dense vegetation, identified at the locations where the elevation difference between the top of canopy and the ground surface is more than 2 m. (b) The modified LiDAR intensity map after masking dense vegetated areas (Blackwood Creek watershed using 2012 LiDAR survey).

### 3.3.2 Extracting valley network and extent

Channels, wet or dry, have geomorphologic characteristics that differentiate them from other features in the landscape. Potential wet channels lie within topographically convergent regions referred to as valley and are associated with positive contour curvature [*Howard*, 1994]. Therefore, wet channel identification can be spatially constrained to the valley extent rather than the entire watershed. This will enhance the performance of wet channel identification in terms of accuracy and computational time.

In order to extract the valley extent, the DEM is smoothed to reduce noise and eliminate insignificant features. Several filtering methods have been applied to smooth DEMs for extracting valley or channel networks, including the Optimal Wiener filter [Pelletier,

2013], Perona-Malik filter [*Passalacqua et al.*, 2010b], and Gaussian filter [Lashermes et al., 2007]. Here, Perona-Malik filter [*Perona and Malik*, 1990], a nonlinear diffusive filter used in GeoNet2.0 [*Passalacqua et al.*, 2010b], is utilized to smooth the DEM. Afterwards, the contour curvature ($\kappa$) for each pixel is computed using equation (1). Figure 23a shows the contour curvature map in a subcatchment of Blackwood Creek watershed.

The valley extent is generated by imposing a relatively small positive curvature threshold ($\kappa_v$) to the curvature map. Figure 23b shows the intensity return within the identified valley extent with curvature greater than or equal to $\kappa_v = 0.025\ \mathrm{m}^{-1}$. The valley network is delineated within the valley extent by imposing a small upslope area threshold (i.e., 25 $m^2$). The flow direction grid, used to calculate upslope area, is generated using the Dinf method [*Tarboton*, 1997b]. The final valley network is generated by eliminating the 1st-order valley segments with length less than 25 m. This procedure may miss possible wet channels located in small 1st-order valleys. However, this error is negligible considering that the wet channels are usually located far downstream of valley heads and in higher order valleys. In addition, the relatively small curvature threshold of 0.025 $m^{-1}$, compared to 0.1 $m^{-1}$ which has been used previously for identifying valley heads [Clubb et al., 2014], further reduces the error since the extracted valley network extends upstream.

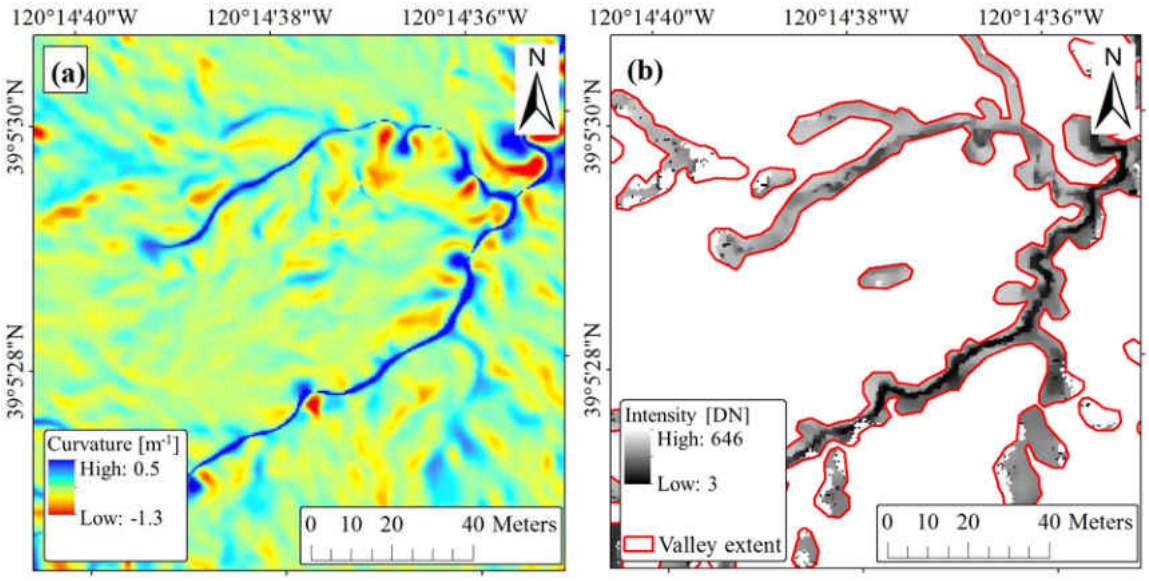


Figure 23. (a) Contour curvature and the visually detectable drainage path by blue segments. (b) The intensity returns within the valley boundary determined by the curvature threshold ($\kappa_v$) of $0.025\ m^{-1}$ in the Blackwood Creek watershed based on 2012 LiDAR survey.

### 3.3.3 Decomposing composite PDF of intensity

LiDAR return intensity varies significantly with the surface characteristics. As stated previously, wet surfaces have relatively low intensity compared to those from dry surfaces. The probability distribution of intensity reflects the variation of intensity over land surface. Assuming the intensity from a single type of surface follows a Gaussian distribution (i.e., normally distributed variation or error in the observations [*Hooshyar et al.*, 2016a]), the overall PDF of intensity has a multimodal distribution constructed from a combination of several Gaussian distributions. Each mode of this PDF represents a category of ground surface (e.g., wet or dry). Having the PDF of intensity, extracted by performing frequency analysis on the intensity map, the underlying modes can be represented by a Gaussian

mixture model (GMM). GMM is a generative model that describes the distribution of the data points generated from a mixture of a finite number of individual Gaussian distributions. GMM with $N$ components (i.e., modes) is given as equation (18) [Rasmussen, 1999]:

$$f(x|\mu_1, \dots, \mu_N, \sigma_1, \dots, \sigma_N, w_1, \dots, w_N\ ) = \sum_{i=1}^{N} w_i \times \mathcal{G}(x|\mu_i, \sigma_i) \quad (18)$$

where $f$ is the Gaussian mixture distribution; $\mathcal{G}(\mu_i, \sigma_i)$ is an individual Gaussian distribution for the mode $i$ with mean $\mu_i$ and standard deviation $\sigma_i$; and $w_i$ represents its corresponding weight or proportion of the mixture distribution. $w_i$ sums to unity for all values of $i$.

Prior to decomposing the composite PDF into individual Gaussian distributions, the number of modes contained in the composite PDF and the corresponding types of ground surface have to be determined. A small number of modes leads to erroneous clustering results by ignoring potential classes of ground surface; but a high number of modes may lead to an overfitted model [Smyth, 2000]. The infinite Gaussian mixture model [Rasmussen, 1999] and cross-validated likelihood [Smyth, 2000] are suggested in literature to find the realistic number of modes in mixture models to avoid overfitting. However, the representative number of modes in intensity return distribution can be identified based on the nature of the problem. Since the goal is to detect wet channels, there should be at least two modes representing wet and dry surfaces. An additional mode, called transition, is also considered to describe moderately saturated areas, shallow streams and possible snow covered areas. Since these three clusters have physical meanings, the overfitting due to a high number of clusters is not an issue in this case.

The mean, standard deviation and weight corresponding to each mode are estimated using the Expectation–Maximization (EM) algorithm [*Moon*, 1996a]. The EM algorithm is an

iterative process of subsequent expectation (E-step) and a maximization (M-step). In the E-step, the expectation function of log-likelihood is computed using the current estimate of the parameters. The parameters of the probability distribution are then updated through maximization of the log-likelihood [Do and Batzoglou, 2008]. The EM algorithm is capable of estimating the parameters of mixture models with hidden variables or latent factors (i.e., the individual mode that creates each sample). The number of iterations and tolerance of the EM algorithm are set to $1.5 \times 10^4$ and $1 \times 10^{-8}$, respectively.

After extracting the decomposed intensity PDFs, two thresholds, $I_W$ for wet pixels and $I_D$ for dry pixels, are extracted to differentiate wet, transition, and dry surfaces. In other words, a discriminative model is developed based on the generative model represented by GMM. $I_W$ is defined as the intensity at the intersect of the wet and transition PDFs. Similarly, the intensity at the intersect of the transition and dry PDFs are considered as $I_D$. In Figure 24a the individual PDFs and the wet and dry thresholds are shown schematically. Having the individual PDF of each mode from EM algorithm, the membership probability is quantified based on equation (19):

$$P(c \in k|I_c) = \frac{w_k \times \mathcal{G}(x|\mu_k,\sigma_k)}{\sum_{i=W,T,D} w_i \times \mathcal{G}(\mu_i,\sigma_i)}, k = W, T, D \quad (19)$$

where $P(c \in k|I_c)$ is the probability of pixel $c$ with intensity value $I_c$ being a member of mode (i.e., cluster) k. k can be either of wet (W), transition (T) or dry (D) modes. Figure 24b schematically shows the membership probabilities of the three modes. Pixels with intensity values less than or equal to $I_W$ are most probably wet. Although the probability of being dry or transition is low in this case, it produced uncertainty in extracting wet pixels. Figure 24c

shows the probability of misclassification of wet pixels when $I \leq I_w$, denoted by $P(c \notin W|I \leq I_w)$. Moreover, pixels with intensity higher than $I_W$ can be wet, but they are most probably transition or dry. When $I > I_w$, the corresponding uncertainty is denoted by $P(c \in W|I > I_w)$ and is shown in Figure 24c. The overall uncertainty of wet pixel identification is the summation of these two misclassification probabilities.

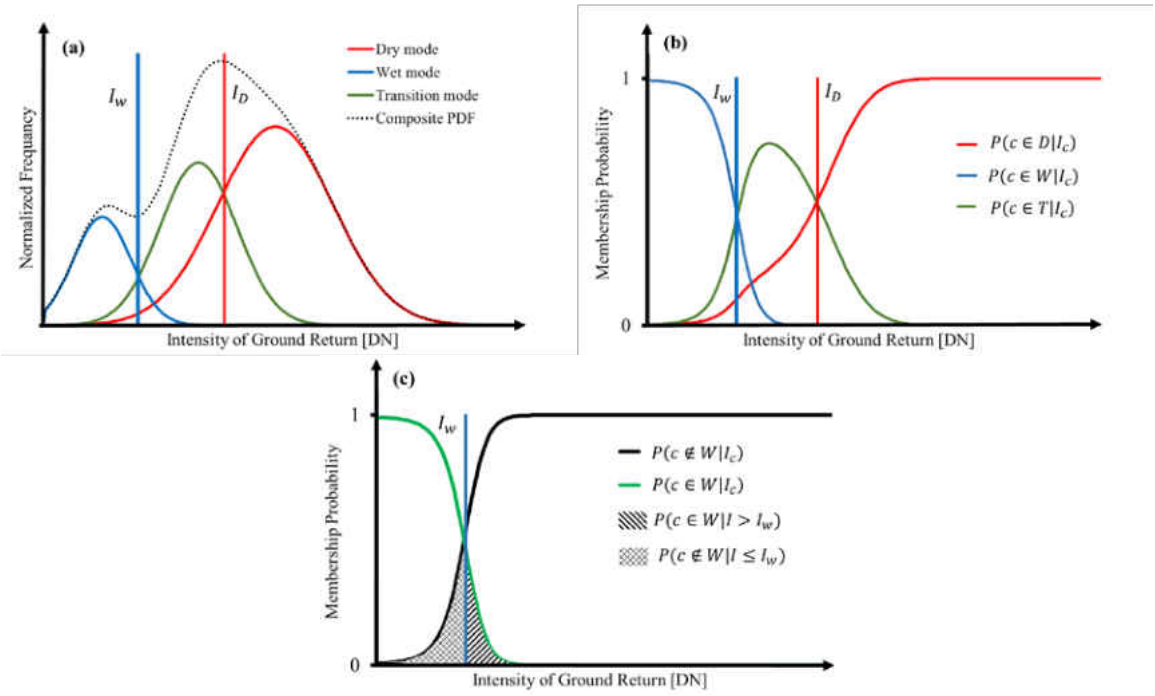


Figure 24. (a) A schematic representation of the composite and the individual PDFs of intensity return along with the wet ($I_W$) and dry ($I_D$) thresholds. (b) The membership probability of each mode. (c) The uncertainty of wet mode cluster visualized as hatched areas.

### 3.3.4 Detecting edges

As stated previously, water surfaces have low intensity values compared to their surrounding dry surface, leading to formation of edges (high gradient pixels) in the

boundary of wet channels. As an example, Figure 25a shows the visually detectable edges at the border of wet channels in the intensity return map of the Blackwood Creek watershed.

Here, the Canny method [Canny, 1986] is used to detect edges based on the gradient of intensity returns. The Canny method originally utilizes a Gaussian filter to remove the noise and robustly calculate the gradient of an image, but the linear Gaussian filter performs spatially constant smoothing throughout the image, causing distortion of meaningful edges. Perona-Malik filter [*Perona and Malik*, 1990; *Perona et al.*, 1994] is a locally adaptive diffusive filter which can smooth the image while simultaneously sharpening the edges. Therefore the Perona-Malik filter is used to enhance the signature of the edges in the intensity map. After smoothing the intensity map, the magnitude of gradient and its direction are computed using equations (20) and (21):

$$dI = \sqrt{{I_x}^2 + {I_y}^2} \tag{20}$$

$$\theta = tan^{-1}\frac{I_y}{I_x} \tag{21}$$

where $I_x$ and $I_y$ represent the local intensity gradients in the horizontal and vertical directions. Incorporating the direction ($\theta$) and magnitude ($dI$) of gradient, the local maximums of gradient are identified and marked as potential edges. After identifying all potential edges, lower ($dI_{min}$) and upper ($dI_{max}$) gradient thresholds are employed to filter out weak edges. All potential edge pixels with gradient less than $dI_{min}$ are deleted, while those with higher gradient than $dI_{max}$ are marked as strong edges. Potential edges with gradient between $dI_{min}$ and $dI_{max}$ are deleted if they are not connected to a strong edge.

Figure 25b shows the detected edges by setting lower and upper thresholds to 60 DN and 80 DN, respectively, after trial and error.

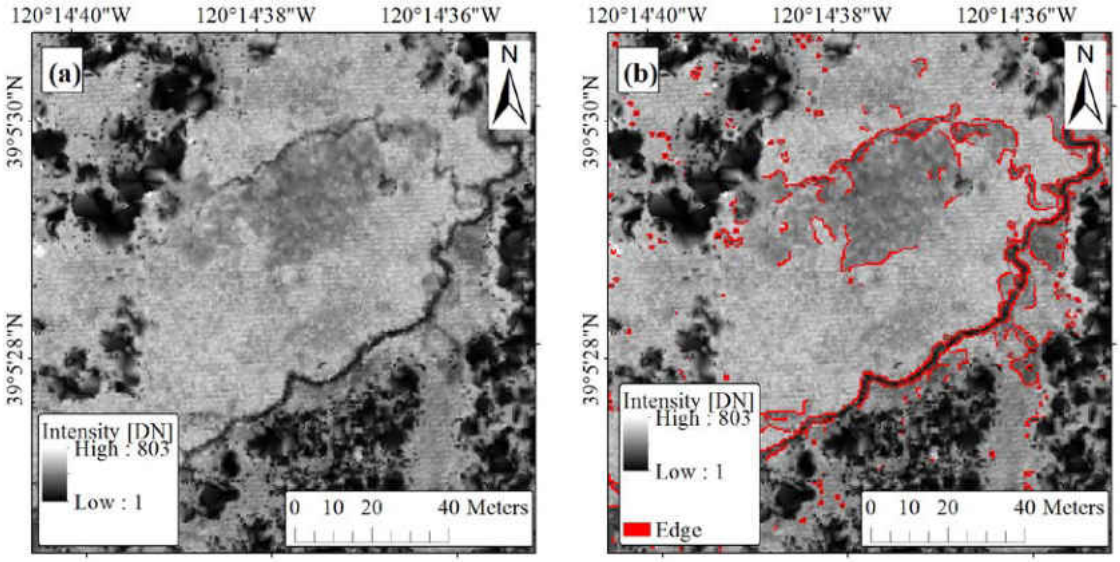


Figure 25. Extracting wet pixels in the Blackwood Creek watershed based on 2012 LiDAR survey. (a) The original intensity map where the wet channels are visually detectable as dark and narrow segments with detectable edges (i.e., abrupt transition from wet to dry in the channel banks). (b) The detected edges in the intensity return map.

### 3.3.5 Identifying wet pixels

Wet pixels are identified based on the decomposed intensity PDFs and the detected edges. All pixels with intensity value equal or lower than $I_W$ are marked as wet and all pixels with intensity higher than $I_D$ are classified as dry. For pixels within the range of $[I_W, I_D]$, if edges (i.e., abrupt transition from wet to dry in the channel banks) are detected nearby in the intensity map, the pixels are also classified as wet. Therefore, the following criteria are used to extract wet pixels: 1) pixels with intensity less than or equal to $I_W$; and 2) pixels with

intensity higher than $I_W$ and less than $I_D$ and edges are detected within 1 m . Any pixel that satisfied one of these two criteria is marked as wet. The identified wet pixels for the subcatchment in the Blackwood Creek watershed are shown in Figure 26.

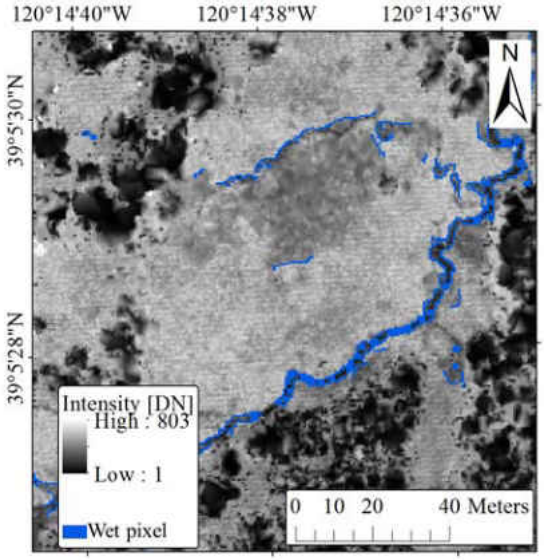


Figure 26. The identified wet pixels based on intensity thresholds for wet and dry pixels from decomposed intensity PDFs, and the detected edges for 2012 LiDAR survey in the Blackwood Creek watershed.

### 3.3.6 Generating wet channel network

The initial wet channel segments are extracted by overlaying the identified wet pixels onto the existing valley network (delineated from the DEM). The generated network may be disconnected for several reasons. Some wet channels are naturally disconnected from the main network however, the disconnection may be erroneous due to the mismatch between the valley network and the intensity map. A small offset between the valley network and the wet pixels may exist in some locations, mainly due to distortion of the DEM through the

filtering procedure or error in the DEM itself (Figure 27). Moreover, low quality and missing intensity data can also lead to disconnection in wet channel network.

To mitigate the error regarding mismatch between the valley network and the intensity map, a 1-m buffer zone is added to the wet pixels. In other words, for any valley pixel, it is marked as wet if there is a wet pixel within 1 m (Figure 28a). To resolve the disconnection caused by missing intensity data and vegetation coverage, for any 400-m-long valley section starting from point $p$ heading to downstream, if at least 50% of the section's length is classified as wet, the point $p$ is considered as a part of the wet channel network. This procedure led to an overestimated initial wet channel network which is further processed by eliminating any 1$^{st}$-order wet channel that had less than 20% of its length initially identified as wet pixels. The resulting wet channel network is further processed manually to connect the segments which are isolated due to missing intensity data. Figure 28b shows an example of the valley and wet channel in the Blackwood Creek watershed.

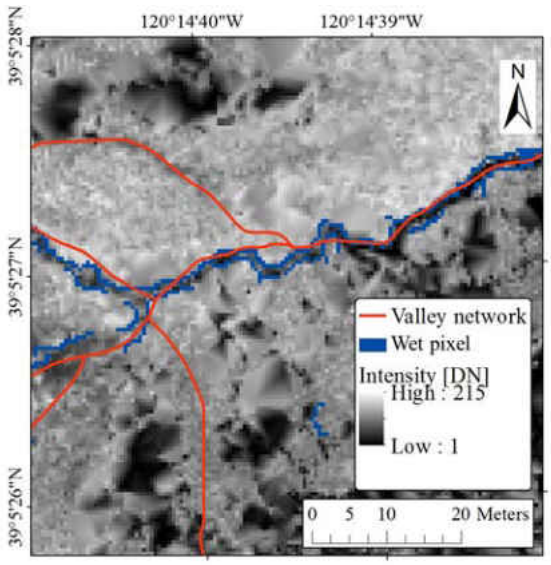


Figure 27. Overlay of intensity map and valley network extracted from LiDAR-based DEM for 2012 LiDAR survey in the Blackwood Creek watershed. Some valley segments are not exactly located within the wet channel boundary.

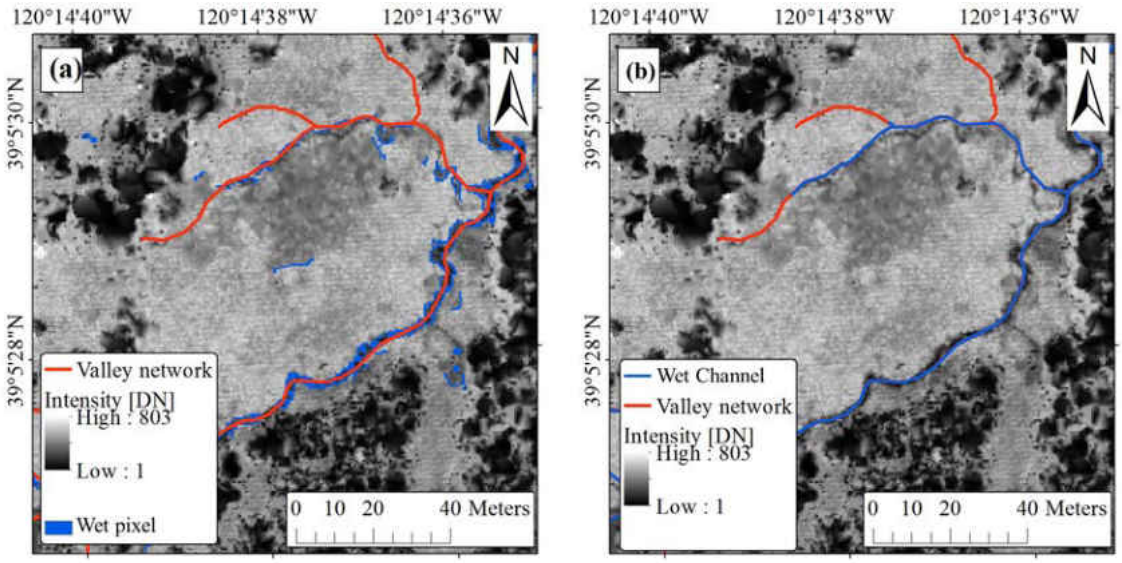


Figure 28. Extracting wet channel network in the Blackwood Creek watershed. (a) The base valley network extracted from topographic data, and the wet cells identified based on LiDAR intensity. (b) The connected wet channel network along with the base valley network after processing wet channel segments.

## 3.4 Results

### 3.4.1 Intensity thresholds

The methodology described above is then applied to LiDAR surveys for five study watersheds shown in Table 2. In the Blackwood Creek and Ward Creek watersheds, the LiDAR scans are performed both in 2010 and 2012; whereas, the LiDAR data for the other three watersheds are only available for 2010. The PDFs of intensity along with the extracted modes (i.e., wet, transition and dry) are shown in Figure 29. Table 3 shows the identified wet ($I_W$) and dry ($I_D$) thresholds for the study watersheds, derived from the PDFs of the intensity. The thresholds varies both temporally and spatially. For instance, wet threshold in the Ward Creek watershed is identified as 46 DN in 2010 and 72 DN in 2012, respectively.

The discrepancy in the thresholds between two surveys in the same watershed can be potentially attributed to the differences of LiDAR sensors, variations in path length resulting from the altitude changes, scan angle, surface specularity, atmospheric conditions, and the soil moisture conditions.

Table 3. Thresholds for identifying wet and dry channels for the study watersheds.

| **Watershed** | **Year** | **Thresholds [DN]** | | **Wetted Channel Length [km]** |
|---|---|---|---|---|
| | | $I_w$ | $I_d$ | |
| **Blackwood Creek, CA** | 2010 | 23 | 84 | 30.3 |
| | 2012 | 42 | 165 | 51.0 |
| **Ward Creek, CA** | 2010 | 22 | 77 | 27.3 |
| | 2012 | 62 | 174 | 53.9 |
| **General Creek, CA** | 2010 | 25 | 89 | 13.6 |
| **Trout Creek, CA** | 2010 | 36 | 104 | 22.8 |
| **Incline Creek, NV** | 2010 | 60 | 110 | 27.7 |
| **Incline Creek, NV (Upstream)** | | | | 14.8 |

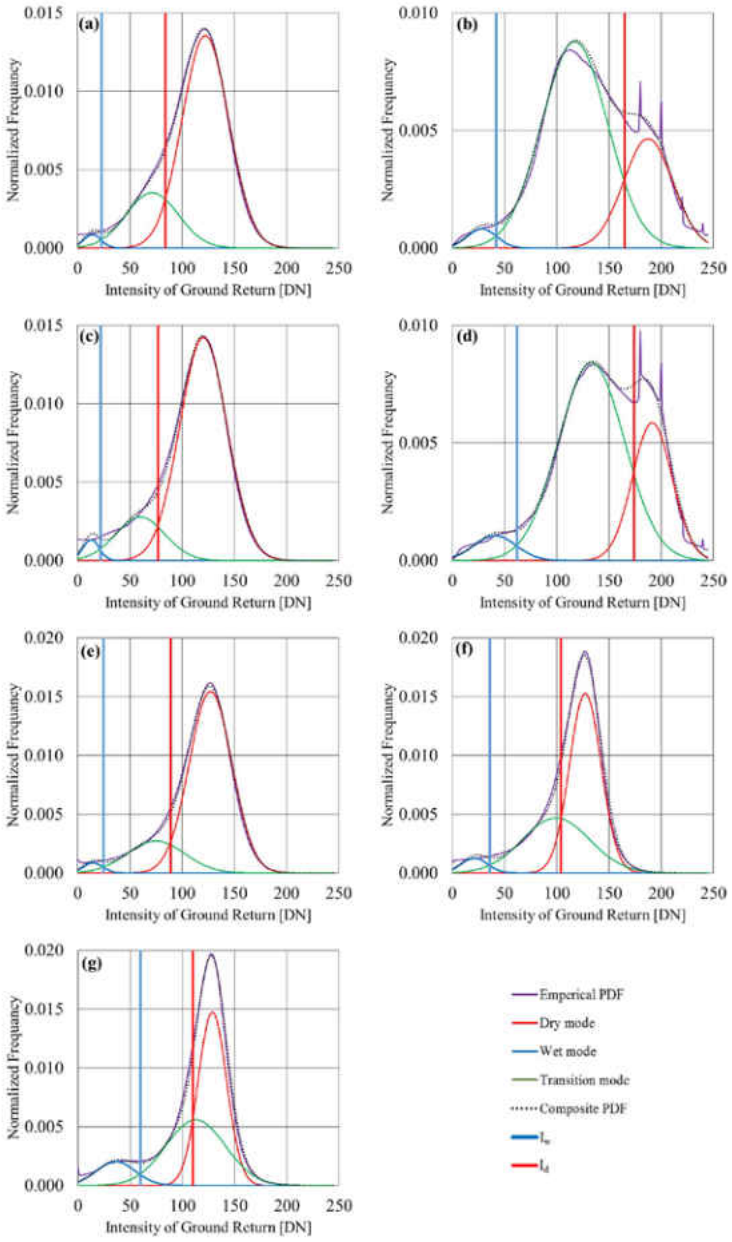


Figure 29. The multimodal PDF of intensity returns and the decomposed individual distributions representing wet, transitional and dry modes along with the wet ($I_w$) and dry ($I_d$) transitions, (a) & (b) for the Blackwood Creek watershed based in 2010 and 2012, (c) & (d) for the Ward Creek watershed in 2010 and 2012, (e) for the General Creek watershed in 2010, (f) for the Trout Creek watershed in 2010, and (g) for the Incline Creek watershed in 2010.

### 3.4.2 Flowing channel network

Wet surfaces are identified within valley extent based on the thresholds extracted from the intensity PDF and the edges in intensity map as described in Section 3. Intensity images and DEMs for the study watersheds are generated with a spatial resolution of 0.5 m. Following the procedure explained in Section 3.6, the wet channel networks are delineated by combining the classified intensity image and LiDAR-based valley network.

Two snapshots (two points in time) of identified wet channel network are compared in the Blackwood Creek (Figure 30a and Figure 30b) and the Ward Creek watersheds (Figure 30c and Figure 30d). The wet channel networks in Figure 30 are the connected part of the wet channels that contribute to the streamflow in the outlet. In both watersheds, there are more wet channels during the 2012 survey than the 2010 survey. In the Blackwood Creek, the total wetted channel length is 51.5 km during the 2012 survey and 26.3 km during the 2010 survey; the corresponding wet channel density, which is defined as the ratio of wetted channel length to total drainage area, is 1.78 km/km$^2$ and 0.91 km/km$^2$, respectively. The total wetted channel length in the 2012 survey is almost twice of that in the 2010 survey. As shown in Table 2, the streamflow during the 2012 survey (0.52 m$^3$/s) is significantly higher than that during the 2010 survey (0.10 m$^3$/s); and the streamflow exceedance probability is 40% and 73% during the 2012 and 2010 LiDAR scans, respectively. It should be noted that the streamflow during the 2012 survey is about 5 times of that during the 2010 survey. This indicated a nonlinear relationship between streamflow and wetted channel length. Similarly for the Ward Creek watershed, the identified wetted channel length during the 2012 survey (51.8 km) is twice that of 2010 survey (29.3 km). Correspondingly, the streamflow during

the 2012 survey is about 4.5 times the streamflow during the 2010 survey (Table 2). The calculated wetted channel length involved a level of uncertainty due to low quality and missing intensity data. Generally, it is difficult to quantify the exact uncertainty regarding the flowing channel length. However, the percentage of manually added length (described in Section 3.6) to the total length of the wet channel network can be a proxy for the uncertainty in the results. In the Blackwood Creek watershed the ratio of manually added length to the total length for 2010 and 2012 are 8% and 13%, respectively; and the ratio in the Ward Creek watershed for 2010 and 2012 are 13% and 15%, respectively. This indicated that the missing data in the LiDAR intensity maps introduced an uncertainty of approximately 15% into the total length of wet channels.

The identified wet channels for the other three watersheds during the 2010 survey are presented in Figure 30: e) General Creek; f) Trout Creek; and g) Incline Creek. The wet channel for the General Creek in Figure 30e is only located in the main stream and the total wetted channel length is 14.6 km. The corresponding wet channel density is 0.76 km/km$^2$, which is the smallest among all the study watersheds. This indicated a dry condition during the LiDAR survey dates as shown by the streamflow exceedance probability of 95% in Table 2. The total wetted channel length in the Trout Creek watershed shown in Figure 30f is 28.8 km and the wet channel density is 1.51 km/km$^2$; the streamflow exceedance probability is 54%. The Incline Creek watershed has two main tributaries, and there are two streamflow gage stations in the watershed (Figure 30g). One gage (#10336700) is located at the watershed outlet with a drainage area of 17.3 km$^2$ and the other (#103366993) is located on one of the main tributaries with a drainage area of 7.4 km$^2$. The wet channel density is

2.15 km/km$^2$ for the catchment and 2.73 km/km$^2$ for the subcatchment; and the streamflow exceedance probabilities are 66% and 74%, respectively. This small discrepancy is due to the spatial heterogeneity of land cover, i.e., the subcatchment is a natural area but the downstream area of the catchment is developed.

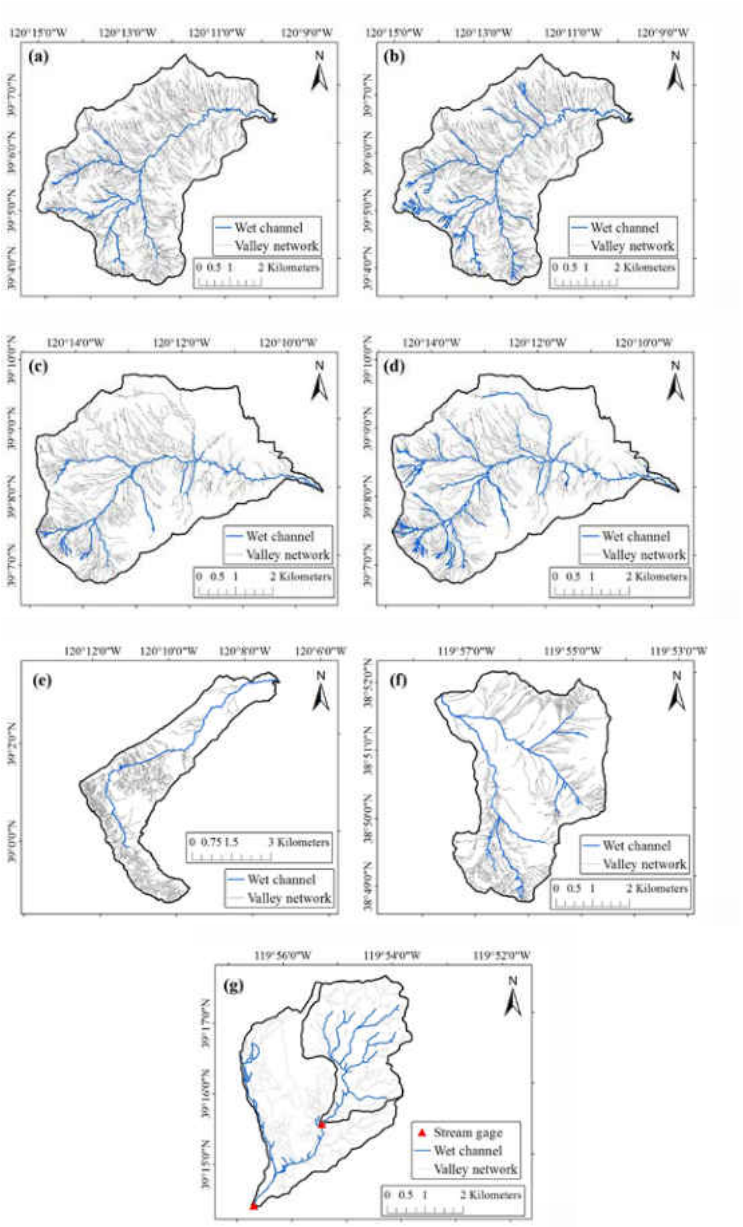


Figure 30. Connected wet channel (after deleting isolated wet channel segments) and valley network based on LiDAR data for Blackwood Creek watershed in 2010 (a) and 2012 (b), Ward Creek watershed in 2010 (c) and 2012 (d), General Creek watershed in 2010 (e), Trout

## 3.5 Discussion

In order to validate the extracted wet channel networks, the relationship between wetted channel length and streamflow is analyzed. The availability of two LiDAR surveys for Blackwood Creek and Ward Creek watersheds (Table 2) provided an opportunity to study wet channel dynamics. Figure 31a shows wetted channel length from LiDAR data versus streamflow for these two watersheds. Generally, the wetted channel length decreases with decreasing streamflow for a given watershed, but the decreasing rate of streamflow is higher than that of wetted channel length. For the Blackwood Creek and the Ward Creek watersheds, the wetted channel length shrunk to almost half from 2012 to 2010 LiDAR surveys; while streamflow decreased to 20% in both watersheds.

Wetted channel lengths are generally highly correlated with streamflow, and power-law relationships are usually identified to represent the relationship [Gregory and Walling, 1968; Godsey and Kirchner, 2014]. The power-law relationship is typically identified using multiple data points within the watershed which requires multiple snapshots of wetted channel length. It is reasonable to assume a similarity of wetted channel length and discharge relationship for the five study watersheds since they are all in close proximity to Lake Tahoe with similar hydro-geomorphologic conditions. The climate aridity index, defined as the ratio between mean annual potential evaporation to precipitation [Budyko, 1971], ranged from 1 to 1.6 for the five watersheds. The relation between wetted channel length and discharge during recession periods for all the six stream gages are plotted in Figure 31b. A power-law relationship, $L = (73.0 \pm 1.2)\, Q^{0.44\pm0.09}$ (or $Q \propto L^{2.38\pm0.48}$) is the best fit to the data with $R^2 = 0.80$ (Figure 31b). Godsey and Kirchner [2014] compiled the values of

scaling exponent for 11 catchments in the literature, and the reported values ranged from 0.042 to 0.688. The scaling exponent of the power-law relationship (i.e., 0.44±0.09) is within the range of reported values from fieldwork in other regions.

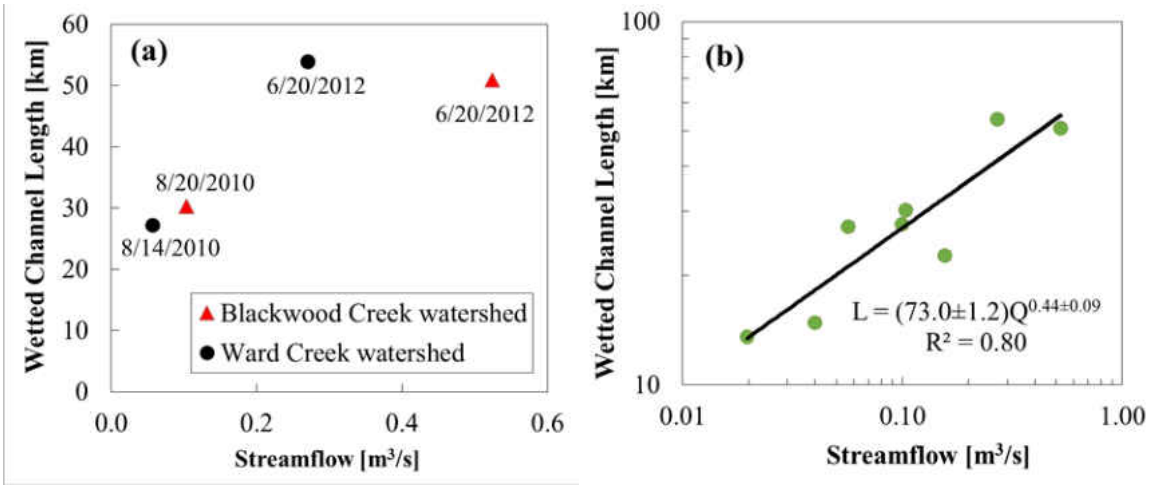


Figure 31. (a) Identified wetted channel length and measured streamflow in the Blackwood Creek watershed (red triangle) and Ward Creek watershed (black circle). (b) Relationship between wetted channel length and streamflow across all the study watersheds.

It should be noted that the scaling exponents in watersheds with varying geologic, topographic and climatic characteristics are quite different [Godsey and Kirchner, 2014], and that the wetted channel length and streamflow in a watershed are not observed to be a one-to-one relationship due to the spatial heterogeneity of runoff generation. Stream network expansion and contraction are related to the local watershed characteristics including the amount and spatial pattern of rainfall, antecedent moisture contents, vegetation, rock type, and topography [Morgan, 1972; Day, 1978; Gurnell, 1978; Goulsbra et al., 2014]. The exponent of the power relationship may vary with wet/dry seasons [Blyth and Rodda, 1973; Wigington et al., 2005] and rising/recession limbs [Roberts and Archibold, 1978]. Given a

unique streamflow, the wetted channel length during the rising limb of the hydrograph can be different from that during a recession limb in that the relative contribution of surface runoff and base flow can vary greatly. Thus, the relationship from Figure 31b may be only applicable at the recession limbs through June to August for the study watersheds.

Although LiDAR data provides high resolution information regarding channels for relatively extensive areas, it is usually limited to one snapshot obtained every five years or more. Alternatively, the temporal dynamics of wet channels can be monitored by implementing various sensors such as soil-moisture sensors which can provide time series of channel wetness. However, their application is spatially restricted due to the high installation cost throughout large watersheds and the difficulty of accessing to some areas. There is an opportunity for coupling these two sources of data in order to mitigate their limitations. The integration of continuous wetness monitoring with ground-based sensors and the extracted wet channels by LiDAR at the watershed scale will advance the knowledge of temporal dynamics of stream network.

This method can be applied to areas where the wet channels are at least partially exposed. This limitation is mainly due to the inability of the current LiDAR technology to record sufficient returns from underneath dense canopy, especially in cases where the area is covered by the vegetative species Abies, which significantly blocks the LiDAR beam. Snow covered areas during winter can also increase the uncertainty of the results. The method presented here is for wet channel extraction but is not recommended for detecting wet surfaces on steep hillslopes, especially in humid regions. The method is also spatially constrained within valley boundaries delineated by a filtered LiDAR-based DEM. Moreover,

wet surfaces on hillslopes usually do not create detectable edges in the intensity map since they cover a relatively extensive area and the transition from wet to dry is gradual. Consequently, wet hillslopes cannot yet be mapped by the edge detection method presented in Section 3.4. The absence of strong edges around wet vegetation automatically prevents the clustering algorithm from classifying them as wet pixels.

One of the main concerns regarding wet channel extraction from LiDAR intensity returns, is the disconnection in wet channel network due to missing and low quality intensity data. The quality of LiDAR data is affected by the condition of the site and also the type of LiDAR system. Development of new LiDAR systems will enhance the quality of LiDAR intensity data, leading to more accurate wet channel network extraction. The proposed method for identifying wet channels can be applied to other watersheds with varying climatic and topographic gradients. Field surveys on wet channels can proceed simultaneously with a LiDAR survey. However, we acknowledge that the NIR LiDAR signal is not able to penetrate water to measure the wet channel bed morphology. Instead, the green LiDAR signal can penetrate water surface and the LiDAR returns can provide water depth information, which can be combined with the intensity of NIR LiDAR to enhance the accuracy of wet channel network mapping.

## 3.6 Conclusions

The temporal dynamics of stream networks are of great importance in understanding the hydrologic processes such as hydrograph recession. The study of stream network dynamics is constrained by lack of temporal high-resolution observations on wet channel

network especially in non-perennial streams. LiDAR provides an opportunity for mapping wet channel networks because of the topographic and intensity information delivered with high spatial resolution. Here, a systematic method is developed for mapping wet channel networks based on LiDAR data. Wet channels are extracted by integrating the topographic information (i.e., flow direction grid and valley network) and the identified wet pixels by intensity of ground returns. The frequency distribution of intensity return is utilized to identify two thresholds representing wet, transition and dry surface. Edge detection in digital images is used to accurately map the wet channels that are located within transition zone based on their intensity return. The proposed method is applied to extract wet channel networks in five watersheds in the Lake Tahoe area.

The intensity threshold derived from the PDF of intensity return for differentiating wet and dry pixels vary both spatially (from watershed to watershed) and temporally (for the same watershed in different times). The differences of LiDAR sensors, variations in path length resulting from the altitude changes, scan angle, surface specularity, atmospheric conditions, and the soil moisture conditions can potentially explain the variation of intensity thresholds.

A power-law relationship between wetted channel length and streamflow is derived to validate the extracted wet channel networks. A power-law relationship, $Q \propto L^{2.38\pm0.48}$ is the best fit to the data. The uncertainty regarding the wetted channel length is mainly due to the vegetation coverage, mismatch between the valley network (extracted from topographic DEM) and intensity map, and the uncertainty of the clustering approach. Using the percentage of manually added length (described in Section 3.6) to the total length of the wet

channel network as a proxy for the uncertainty in the results indicates that the missing data in the LiDAR intensity maps introduced an uncertainty of approximately 15% into the total length of wet channels.

Future enhancements to this work are contingent upon the acquisition of reliable field observations that are obtained within days or hours of the LiDAR acquisition. These data would be of great benefit to the hydrologic remote sensing research community as a whole, extending beyond LiDAR into other types of optical, multispectral and synthetic aperture radar imagery.

# CHAPTER 4: RE-VISITING THE DEPENDENCE OF DRAINAGE DENSITY ON CLIMATE AND DRAINAGE AREA BY LIDAR DATA

Drainage network is an important geomorphologic and hydrologic feature which significantly controls runoff generation. Drainage network is composed of unchannelized valleys and channels [*Dietrich et al.*, 1993b]. At valley heads, flow changes from unconfined sheet flow on the hillslope to confined flow in valley [Montgomery and Dietrich, 1989; Moglen et al., 1998]. Localized confined flow dominates in valleys as a result of convergent topography with positive curvature [*Howard*, 1994]. Drainage density ($D_d$), defined as the ratio of the total valley length in a watershed to the drainage area [*Horton*, 1932b; 1945b], quantitatively represents the efficiency of the drainage basin and controls the runoff response at the catchment scale [Rinaldo et al., 1991; Rodriguez-Iturbe et al., 2009; Biswal and Marani, 2010; Mutzner et al., 2013; Godsey and Kirchner, 2014; Ghosh et al., 2016]. Watersheds with higher drainage density usually produce a higher peak flow and sediment load [Dunne and Leopold, 1978]. Di Lazzaro et al. [2015] demonstrated that spatial heterogeneity of drainage density within watersheds affects surface and subsurface runoff.

Drainage density is controlled by various factors including climate, lithology, vegetation, and topography [*Melton*, 1957; *Carlston*, 1963; *Montgomery and Dietrich*, 1988; *Sangireddy et al.*, 2016b]. Gregory and Gardiner [1975] indicated that drainage densities in arid regions have higher variability compared with humid areas due to the seasonal variation of climate. By analyzing watersheds in arid regions including Arizona, New Mexico, Colorado

and Utah, Melton [1957] identified a negative correlation between drainage density and precipitation effectiveness PE index, which is defined as 10 multiplied by the summation of ratios between monthly average precipitation and evaporation [Thornthwaite, 1931]. Madduma Bandara [1974] presented a positive correlation between drainage density and PE index for humid watersheds in Sri Lanka. Combining the data from Melton [1957] and Madduma Bandara [1974], a U-shaped relationship between drainage density and PE index was introduced [Abrahams, 1984] and has been explained by the trade-off between the resistive force of vegetation and the erosive force of runoff [Abrahams, 1984; Istanbulluoglu and Bras, 2005; Collins and Bras, 2010].

It has also been reported that drainage area affects drainage density [Gregory and Walling, 1973]. Based on the reported data in the literature, Pethick [1975] presented a power relationship, $D_d \propto A^{-0.337}$, which indicates that drainage density ($D_d$) decreases with drainage area ($A$). The exponent of the power relationship varies with environmental characteristics such as climate, vegetation, and geology [Gardiner et al., 1977; Richards, 1978]. Since drainage density is controlled by both watershed properties and climate, the dependence of drainage density on drainage area may vary from humid to arid regions.

In this study, high resolution topographic data from Light Detection and Ranging (LiDAR) in 120 watersheds across the United States are utilized to extract accurate valley networks and re-visit the relationship between drainage density and climate as well as drainage area. The objectives of this chapter include: (i) re-visiting the U-shaped relationship between drainage density and climate; and (ii) interpreting the impact of drainage area on drainage density. The remaining of the chapter is organized as follows. The study sites and

methods are introduced in Sections 2 and 3. Section 4 presents the results in terms of the relationship between drainage density and long-term climate as well as drainage area, followed by the discussion in Section 5. Section 6 summarizers and concludes the findings.

## 4.1 Study Sites

The study sites are selected based on the LiDAR availability and minimal human impacts such as land use change, reservoir, and road construction. The Center for LiDAR Information, Coordination and Knowledge (CLICK, http://lidar.cr.usgs.gov) provides data tiled by USGS Quarter Quadrangles in LAS and ASCII formats [Stoker et al., 2006]. The blue area in Figure 32a shows the LiDAR data availability in the CLICK website; and the red dots highlight the 120 sites selected for this study, located in 17 states with various climate conditions. The point cloud data of ground returns from LiDAR are processed to derive 1 m Digital Elevation Models (DEMs) using QCoherent software LP360 for ArcGIS.

Climatic data including potential evaporation and precipitation are processed for exploring the relationship between climate and drainage density. Potential evaporation is a function of several meteorological variables such as wind speed, humidity, radiation, and air temperature [Mcvicar et al., 2012]. In this study monthly potential evaporation data with a spatial resolution of 8 km is obtained from Zhang et al. [2010]. This data was computed by the Priestly-Taylor method [Priestley and Taylor, 1972], and has been used for long-term and seasonal water balance analysis [Wang and Hejazi, 2011; Chen et al., 2013]. Mean annual precipitation during 1981-2010 is computed based on the parameter-elevation regressions on independent slopes model (PRISM) data with a spatial resolution of 4 km [Daly et al.,

1994]. Mean annual potential evaporation and precipitation are spatially averaged over each study watershed.

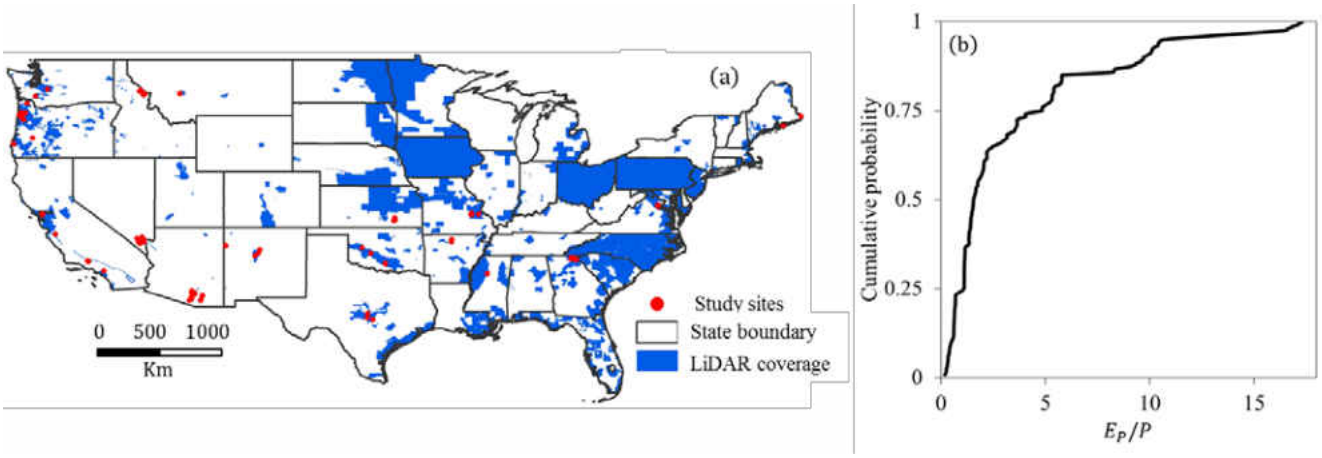


Figure 32. (a) The locations of the study sites and the LiDAR data availability across United States; and (b) the cumulative probability distribution of the climate aridity index ($E_P/P$) in the study sites.

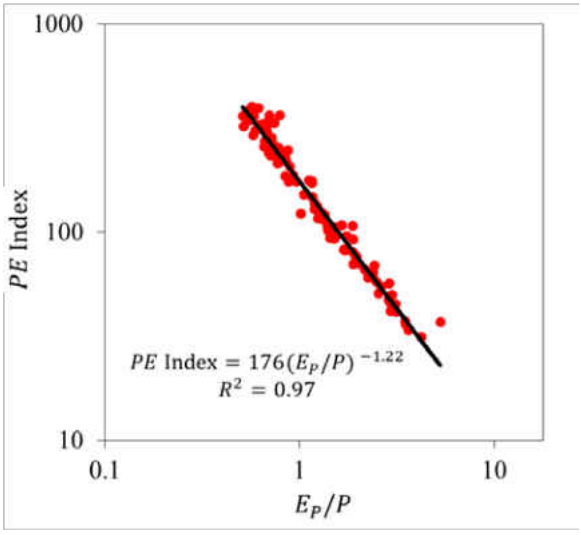


Figure 33. The relationship between PE index and climate aridity index ($E_P/P$) using the data provided by *Wang and Wu* [2013b] after removing the outliers.

## 4.2 Methods

### 4.2.1 Drainage network extraction

LiDAR provides high resolution topographic data which facilitates extracting topographic features such as drainage networks accurately [*Passalacqua et al.*, 2010b; *Clubb et al.*, 2014; *Hooshyar et al.*, 2015]. In this study, valley networks are delineated using a curvature-based method developed by *Hooshyar et al.* [2016b]. The method first filters the DEM using Perona-Malik nonlinear diffusive filter [*Perona and Malik*, 1990] and then calculates the contour curvature given as equation (1). After removing the sinks using *O'callaghan and Mark* [1984b]'s method, the flow direction grid from $D_\infty$ [*Tarboton*, 1997b] is adjusted by incorporating the local curvature. Afterwards, the terrain is objectively segmented into valley and ridge patches, where patches are defined as the local maximums or minimums in the curvature grid. To do so, a segmentation curvature threshold is calculated in the way that maximum separation in the terrain (maximum number of patches) is achieved. Afterwards, the non-valley and non-ridge patches are removed systematically using Otsu [1975]'s method leading to the valley and ridge skeletons. Consequently, the valley skeleton is thinned to a 1-pixel wide valley line by checking the existence of a ridge patch between two intersecting valleys. For valley extraction, the method requires two user-defined parameters including the time of forward diffusion ($T_F$) for filtering and the connecting threshold ($C_T$), which are set to 50 and 20 m for all the watershed in this study. *Hooshyar et al.* [2016b] examined the performance of the method in three watersheds and compared the results with the state-of-the-art methods.

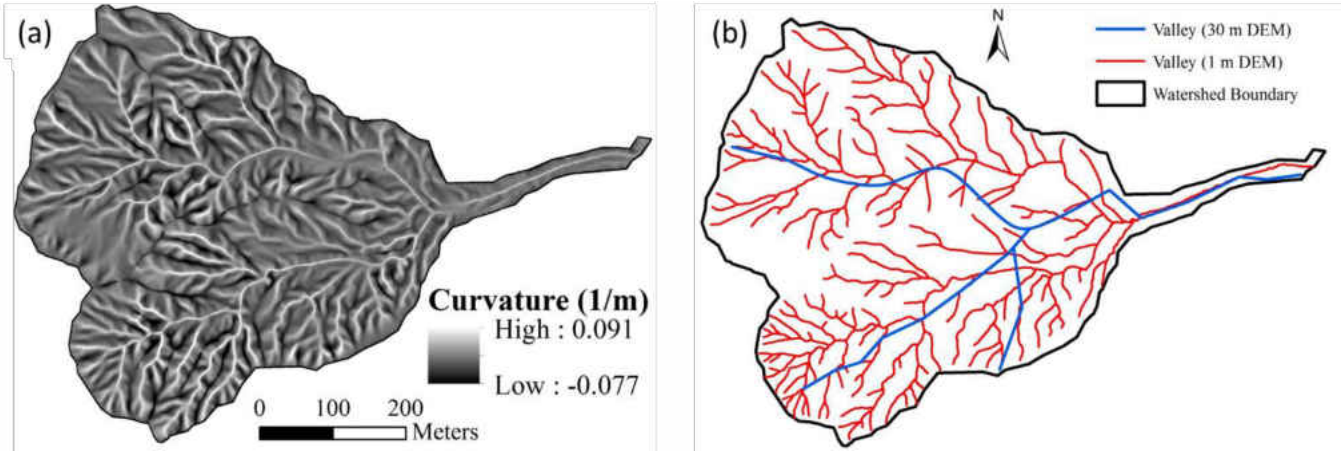


Figure 34. (a) The contour curvature computed from the filtered DEM; and (b) the extracted valley network from 1 m and 30 m DEMs in the Isleta Drain watershed located in New Mexico.

Drainage density ($D_d$) is computed as the ratio of the total valley length to the total drainage area. Drainage density has the dimension of $L^{-1}$ and is scale dependent. *Sangireddy et al.* [2016b] introduced dimensionless drainage density index as the ratio of the total area of convergent pixels (the area of valley skeleton) and the drainage area. Here, the input DEMs have the same resolution (1 m); therefore, using the traditional definition of drainage density does not introduce any systematic error in the results.

### 4.2.2 Climate aridity index

Climate aridity index, defined as the ratio of mean annual potential evaporation ($E_P$) to precipitation ($P$), is used as the indicator of long-term climate. Climate aridity index ($E_P/P$) is the first order control on the partitioning of mean annual precipitation into evaporation and runoff [*Budyko*, 1971]. Climate aridity index describes most of variability of runoff coefficient, which is closely correlated with drainage density [Sankarasubramanian and Vogel, 2002] and is related to the perennial stream density through the Budyko

framework [*Wang and Wu*, 2013b]. Climate aridity index also reflects the vegetation cover as it is strongly correlated with the Normalized Difference Vegetation Index (NDVI) [Voepel et al., 2011]. Climate aridity index objectively categorizes watersheds into arid and humid; the watersheds with $E_P/P < 1$ are classified as energy-limited or humid and the watersheds with $E_P/P > 1$ are referred to as water-limited or arid.

The climate aridity index in the study sites ranges from 0.18 to 17.3 and Figure 32b shows its cumulative probability distribution. Melton [1957] and Madduma Bandara [1974] used PE index to quantify the long-term climate for studying climate controls on drainage density. PE index is defined as 10 multiplied by the summation of ratios between monthly average precipitation and evaporation [Thornthwaite, 1931]. In this study, PE index in Melton [1957] and Madduma Bandara [1974] is converted to climate aridity index using the data provided by *Wang and Wu* [2013b] after removing the outliers (Figure 33). The obtained climate aridity index in Madduma Bandara [1974]'s watersheds varies from 0.53 to 1.8 and from 1.9 to 9.1 in Melton [1957]'s watersheds.

## 4.3 Results

The valley networks for all the study watersheds are extracted using 1 m LiDAR-based DEMs. As a demonstration, Figure 34a shows the curvature grid computed from the filtered DEM in the Isleta Drain watershed; and Figure 34b shows the corresponding valley network.

### 4.3.1 Drainage density and climate

Figure 35a shows the drainage density and climate aridity index of the watersheds in this study overlaid with the reported data by Melton [1957] and Madduma Bandara [1974]. In our study sites, the drainage density varies from 3.8 km/km$^2$ to 43.5 km/km$^2$. The drainage density in Madduma Bandara [1974]'s watersheds varies from 2.7 km/km$^2$ to 113 km/km$^2$ and from 2.6 km/km$^2$ to 14.5 km/km$^2$ in Melton [1957]'s watersheds.

The relationship between drainage density and climate aridity index from this study shows a strong increasing trend in arid regions ($E_P/P > 1$) with $p = 3.9e - 11$, where $p$ denotes the p-value of the least-squared linear regression. However, the trend in humid regions ($E_P/P \leq 1$) is not significant ($p = 0.49$), which is in contrast with the decreasing trend observed in Madduma Bandara [1974].

The trends are further analyzed using the Mann-Kendall test [Mann, 1945; Kendall, 1975] which quantifies the significance of a trend through a normalized statistic, z-value. A high positive z-value indicates strong increasing trend; while, a small negative z-value corresponds to strong decreasing trend. Table 4 shows the results of the Mann-Kendall test in arid ($E_P/P > 1$) and humid ($E_P/P \leq 1$) watersheds. A statistically significant increasing trend is detected in arid watersheds; whereas, no trend exists in the humid regions.

Table 4. Trend analysis based on the Mann-Kendall test for arid and humid watersheds.

| | Number of data | p-value | z-value | Trend (95% significance) |
|---|---|---|---|---|
| **Arid watersheds ($E_P/P > 1$)** | 91 | 1.4e-11 | 6.7 | **Increasing** |
| **Humid watersheds ($E_P/P \leq 1$)** | 29 | 0.38 | -0.88 | **No trend** |

As shown in Figure 35a, although the extracted drainage densities match the data from Madduma Bandara [1974]; they are relatively higher than those from Melton [1957]. This can be attributed to the difference in map scales and methods used to extract drainage networks in the previous studies. The drainage networks by Melton [1957] were delineated from the topographic maps with the scale of 1:24,000, equivalent to the nominal spatial resolution of 30 m [Kosovich et al., 2008], using the contour crenulation method. Some watersheds in Arizona were mapped through field survey. The drainage networks from Madduma Bandara [1974] were obtained from field work, aerial photograph, and maps with the scale of 1:12,672l; therefore, they correspond to relatively smaller scale than those from Melton [1957].

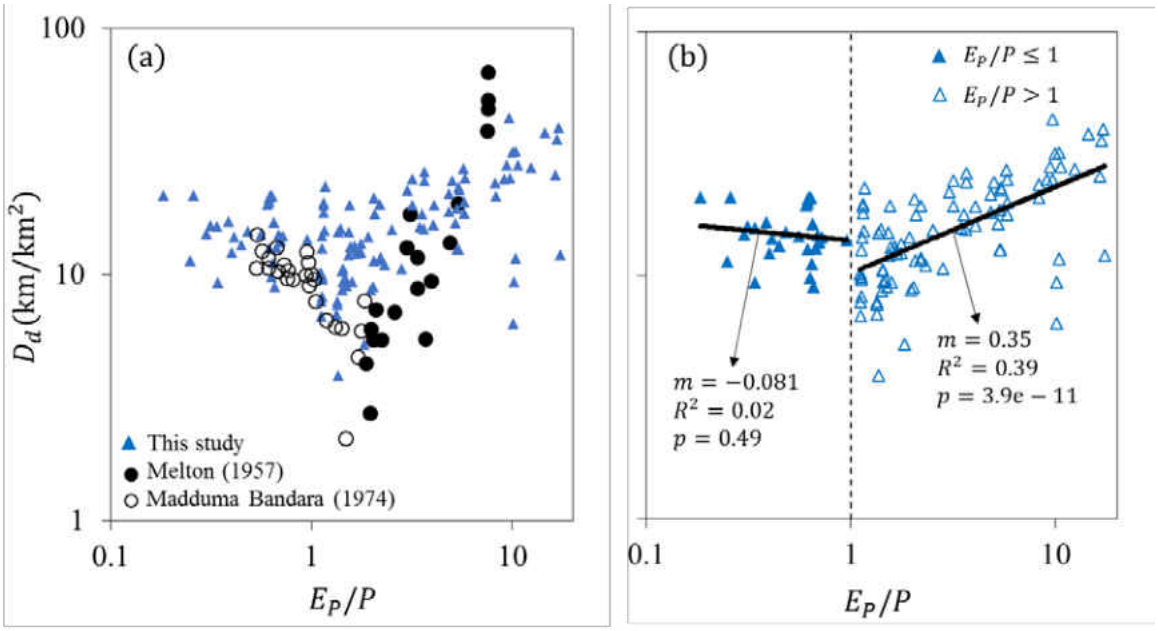


Figure 35. The relationship between drainage density ($D_d$) and climate aridity index ($E_P/P$); (a) the data from Melton [1957], Madduma Bandara [1974], and this study. (b) The correlation analysis of drainage density and climate aridity index in the study watersheds. The least-squares regression line, slope ($m$), R-squared ($R^2$), and p-value ($p$) are shown. For $E_P/P > 1$ (arid regions), a significant increasing trend is observed; whereas, the trend in humid regions ($E_P/P \geq 1$) is not significant.

The extracted drainage network from coarse topographic maps deviates significantly from the correspondingly observed one in the field [Morisawa, 1957; Schneider, 1961]. To demonstrate the effect of DEM resolution on the variation of the drainage density, 1 m DEMs for some of the study watersheds are resampled to 30 m DEMs. 20 watersheds with $E_P/P$ less than 6 and drainage area larger than 0.2 km$^2$ are randomly selected. As an example, Figure 34b shows the extracted valley network from 1 m and 30 m DEMs for the Isleta Drain watershed in New Mexico. As shown in Figure 36a, drainage densities from 1 m DEMs are higher than those from 30 m DEMs. This suggests that the underestimation of drainage

network due to the coarse resolution of the maps may be the reason of the difference between drainage densities from this study and Melton [1957].

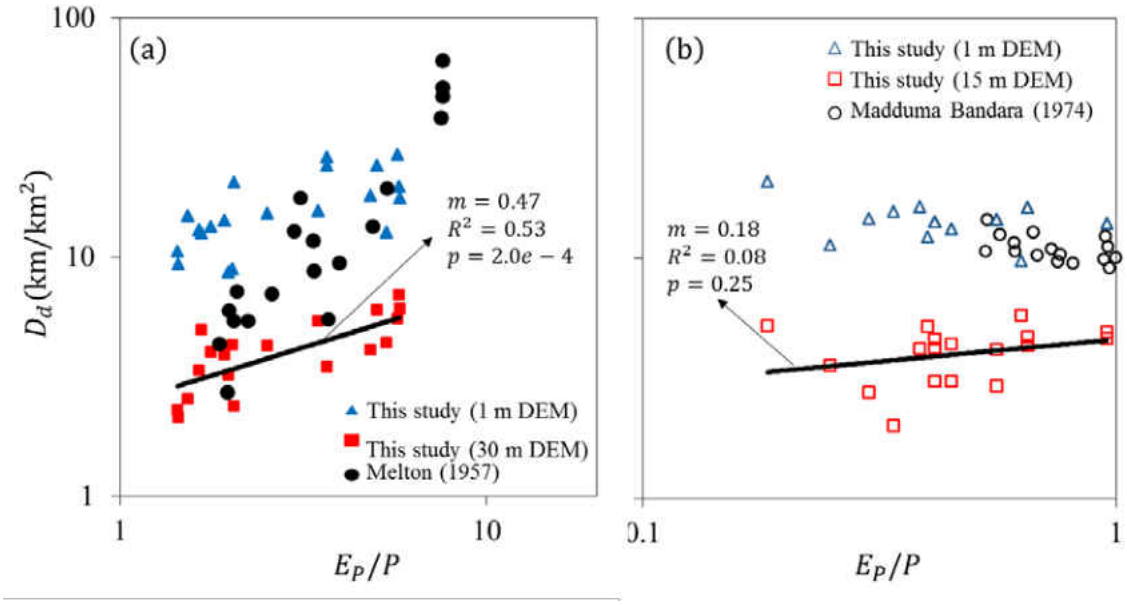


Figure 36. Drainage density ($D_d$) derived from LiDAR-based 1 m DEMs compared with (a) the resampled 30 m DEMs and Melton [1957]'s data; and (b) the resampled 15 m DEMs and Madduma Bandara [1974]'s data. The least-squares regression line to data from resampled DEMS and the corresponding slope (m), R-squared ($R^2$), and p-value (p) are shown.

For $E_P/P \geq 7$, the drainage densities from Melton [1957] are higher than those in this study (Figure 35a). These six watersheds from Melton [1957] are located in Arizona; two within the Chinle watershed in Cameron and four within Saguaro National Monument in Tucson. The valley networks in these six watersheds were mapped by field survey: the two catchments in the Chinle watershed by Schumm [1956] and the other four by Melton [1957]. These watersheds are relatively small with drainage areas between 0.001 to 0.006 km$^2$; whereas, the drainage area of our study sites with $E_P/P \geq 7$ are relatively larger and the average drainage area is 0.40 km$^2$. The small drainage area of the watersheds from Melton

[1957] may contribute to their relatively high drainage density, since the drainage density has a negative correlation with area in arid climate as will be discussed in Section 4.2.

To understand the effect of the spatial resolution on the drainage density trend in the humid climate, 18 watersheds with $E_P/P$ less than 1 and drainage area larger than 0.4 km$^2$ are selected randomly from the study watersheds. LiDAR-based 1 m DEMs for the selected watersheds are resampled to 15 m DEMs. This is approximately equal to the spatial resolution of the topographic maps used by Madduma Bandara [1974]; however, field work and aerial photograph as well were used to delineate the drainage networks by Madduma Bandara [1974]. As shown in Figure 36b, drainage densities from 15 m DEMs are lower than those from 1 m DEMs and regardless of the resolution, they do not present a decreasing trend as observed in Madduma Bandara [1974].

The correlation between drainage density and mean annual precipitation (P) is investigated as shown in Figure 37. *Sangireddy et al.* [2016b] reported significant decreasing when $P \leq P_T$ and increasing trends when $P > P_T$, where $P_T$ is visually detected as $1050\ ^{\mathrm{mm}}/_{\mathrm{yr}}$. Similar pattern is observed in this study as shown in Figure 37a; although, the increasing trend for $P > P_T$ is not significant. The magnitude of $P_T$, which is visually identified as $1050\ ^{mm}/_{yr}$ in *Sangireddy et al.* [2016b], affects the significance of the detected trend. Table 5 shows the trend slope (m) and p-value (p) for different values of $P_T$. To eliminate the need for $P_T$, the data is objectively divided into arid and humid based on $E_P/P$ as shown in Figure 37b. The data in arid regions show a strong decreasing trend ($p = 8.7e-10$); however, no trend is observed in humid watersheds ($p = 0.54$).

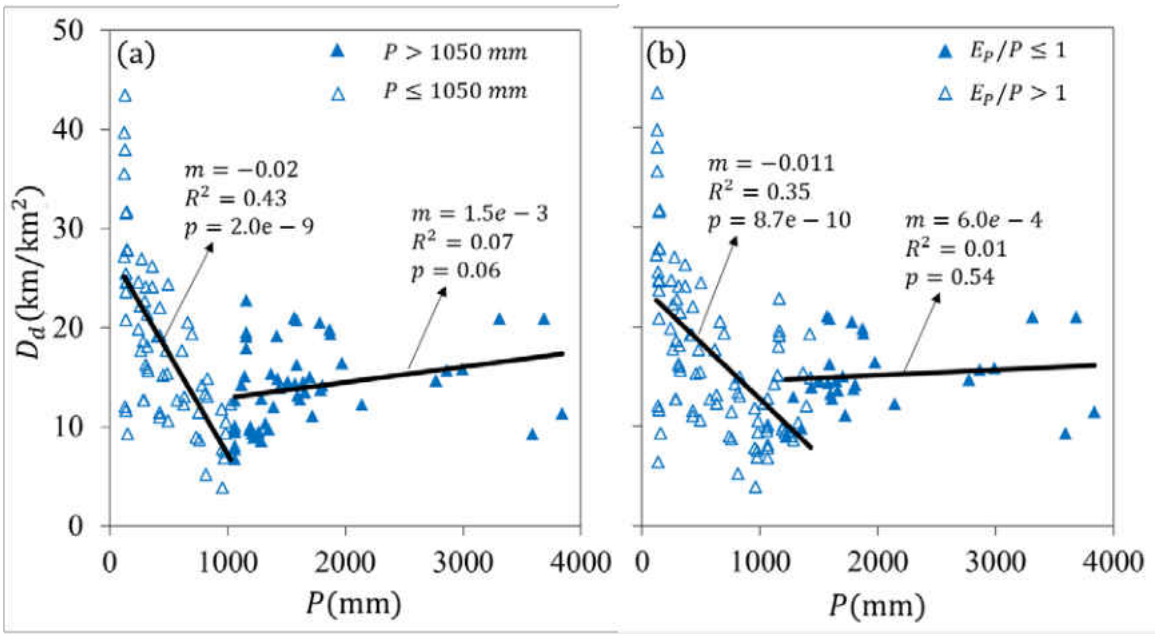


Figure 37. Drainage density ($D_d$) versus mean annual precipitation ($P$) after dividing the data into arid and humid based on (a) $P$ with $P_T = 1050\ ^{mm}/_{yr}$, and (b) climate aridity index ($E_P/P$). The least-squares regression lines, slopes ($m$), R-squared ($R^2$), and p-value ($p$) are shown.

Table 5. The slope ($m$) and p-value ($p$) of the least-squares regression line fitted to the data points with $P > P_T$ for different values of $P_T$

| $P_T$ ($mm$) | $m$ | $p$ |
|---|---|---|
| 1050 | 1.55e-6 | 0.06 |
| 1100 | 7.70e-7 | 0.35 |
| 1150 | 7.99e-7 | 0.36 |

### 4.3.2 Drainage density and drainage area

Here the relationship between drainage density and drainage area is studied. The average drainage area in our data set is 1.20 $km^2$, with a minimum of 0.04 $km^2$ and a maximum of 3.5 $km^2$. The drainage area ranges from 0.0002 $km^2$ to 14.14 $km^2$ in Melton [1957]'s watersheds, and from 0.85 $km^2$ to 4.82 $km^2$ in Madduma Bandara [1974]'s watersheds. To investigate the climate effects on the relationship between drainage density and drainage area, the study watersheds are categorized into humid ($E_P/P < 1$); and arid ($E_P/P \geq 1$). Figure 38 plots the relationship between drainage density and drainage area for arid (Figure 38a) and humid (Figure 38b) watersheds in this study, watersheds in the arid climate from Melton [1957] (Figure 38c), and watersheds in the humid climate from Madduma Bandara [1974] (Figure 38d).

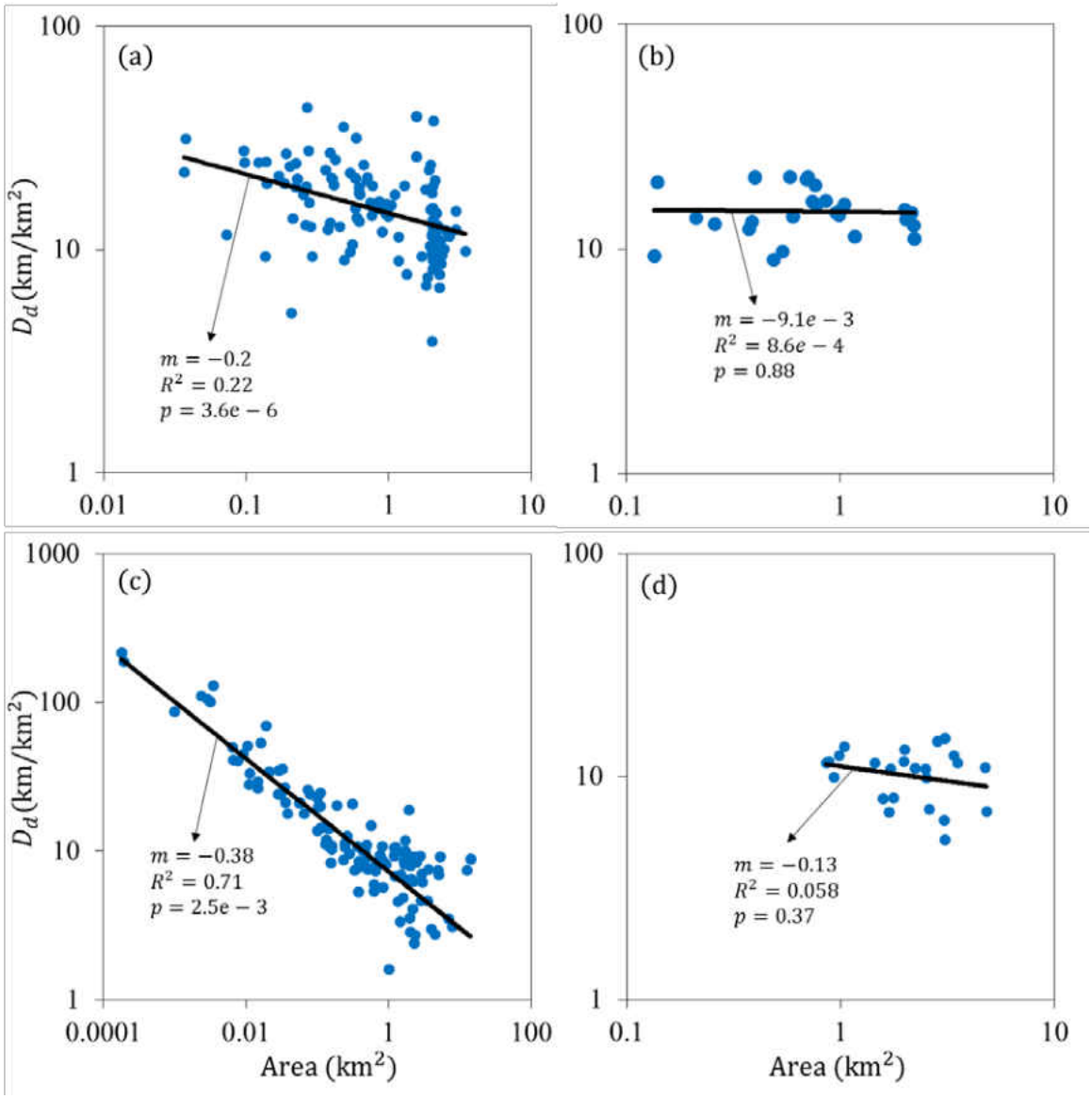


Figure 38. The relationship between drainage density ($D_d$) and drainage area for (a) arid and (b) humid watersheds in this study, (c) watersheds in the arid climate from Melton [1957] , and (c) watersheds in the humid climate from Madduma Bandara [1974]. The least-squares regression line, slope ($m$), R-squared ($R^2$), and p-value ($p$) are shown.

There is a strong negative correlation between drainage density and drainage area in arid watersheds based on Melton [1957]'s and this study's data sets. However, in humid regions the relationship from Madduma Bandara [1974]'s and this study's data does not show a significant correlation.

## 4.4 Discussion

### 4.4.1 Drainage density and climate

For $E_P/P \leq 1$, the drainage density versus climate aridity index by Madduma Bandara [1974] follow a decreasing trend; whereas, such a declining trend does not exist for the watersheds in this study. The decreasing trend by Madduma Bandara [1974] continues until $E_P/P$ approaches to ~1.8. The drainage density also shows a significant decreasing trend with precipitation in arid climate; although, no strong trend was observed in humid regions. This discrepancy can be explained by the land cover in Madduma Bandara [1974]'s watersheds. It is well-known that land use changes, such as agricultural activities, are also major human activities with substantial impacts on landscape [Gregory and Walling, 1968; Montgomery and Dietrich, 1992]. Vegetation cover controls the resistance against the erosive force of runoff [Abrahams, 1984; Collins and Bras, 2010]. As climate becomes more humid, vegetation gets more dense and the erodibility reduces due to the higher resistance by vegetation [Moglen et al., 1998]. In Madduma Bandara [1974]'s watersheds the natural land cover has been consistently removed due to tea plantation over a 100 year period [Madduma Bandara, 1974], therefore, the same vegetation cover exists in different climates leading to the same resistance against erosive force of runoff. Given this circumstance, when

climate aridity index increases (i.e., less precipitation), the erosive force drops while the resistance is constant. This condition results in decreasing drainage density as climate aridity index increases.

### 4.4.2 Drainage density and drainage area

The drainage density has a decreasing trend with drainage area in arid regions; however, no trend is observed in humid regions. Similar pattern exists in Melton [1957]'s Madduma Bandara [1974]'s data. This pattern indicates that the channels are more uniformly distributed across watershed in humid regions compared with arid watersheds. This is confirmed by analyzing the distribution of drainage density in watersheds. 30 watersheds with different values of climate aridity index are selected randomly in our study sites, and each watershed is divided into 3~8 subwatersheds. The maximum stream order of the subwatersheds is greater than 3 and the range of subwatershed area is 0.01~2.93 $km^2$. Figure 39a shows the average, minimum and maximum drainage density of subwatersheds with different drainage areas in the selected 30 study sites. Generally, the variation of drainage density in humid regions is smaller than arid regions. Standard deviation of drainage density ($\sigma_{D_d}$) of subwatersheds in each study site increases with climate aridity index as shown in Figure 39b.

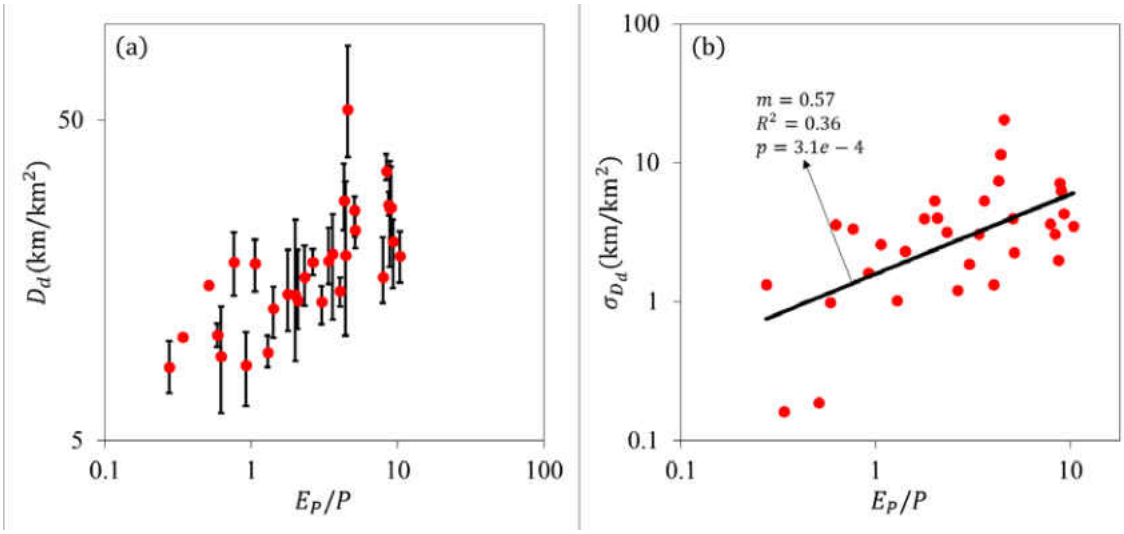


Figure 39. The relationship between drainage density ($D_d$) and climate aridity index ($E_P/P$): (a) Average, minimum and maximum of drainage density from subwatersheds with different drainage area in the selected 30 study sites; and (b) The standard deviation of drainage density ($\sigma_{D_d}$) of subwatersheds in each study site versus climate aridity index.

## 4.5 Conclusion

Technological advancements and the availability of accurate climate data have provided the opportunity to investigate long-lasting questions in hydrology and geomorphology. The drainage networks have been studied extensively in past decades; however, our understanding in some extent is formed by low quality and limited data regarding the land surface and climate. In this study the dependence of drainage density on climate and drainage area was re-visited using publicly available high resolution topographic and climate data.

120 watersheds with natural conditions were selected based on the LiDAR data availability and the drainage network were automatically delineated from 1 m DEMs. There are different definitions for valley in the literature; therefore, the valley networks in Melton [1957], Madduma Bandara [1974], and this study may have been extracted based on different definitions. However, the proposed valley delineation method is reasonably similar to the one used by Melton [1957] and Madduma Bandara [1974], since it utilizes the contour curvature to quantify the convergence, i.e., similar to the tradition contour crenulation method.

The relationship between drainage density and climate aridity index, defined as the ratio of the mean annual potential evaporation to the mean annual precipitation, in the data from Melton [1957] and Madduma Bandara [1974] has a U-shape; however, our result showed decreasing trend in arid regions, which is consistent with the observations in other studies, and no trend in humid watersheds. The increasing trend observed in humid watersheds by Madduma Bandara [1974] can be explained considering the specific vegetation cover in that area. Those watersheds have been modified by extensive human interferences and the natural vegetation has been eliminated due to tea plantation. Therefore, the erosive force increases as the climate gets more humid while the resistance due to vegetation cover remains constant which increases the drainage density. Our finding suggests that the erosive force and the resistance due to vegetation reach an equilibrium in humid regions and the change in climate conditions does not systematically impact the drainage network. Whereas, in arid region, the increase in resistive force of vegetation dominates the escalation of erosive force of runoff which leads to a decreasing trend in

drainage density. Our finding also suggests that natural drainage networks in arid regions are more sensitive to the change in long-term climate conditions compared with the watersheds located in humid regions. This is vitally important for quantifying the climate change impact on natural hydrologic systems and man-made infrastructures [*Alirezaei et al.*, 2017] and influences our understanding of the formation of drainage networks and the response of hydrologic systems to climate change.

The relation between drainage density and drainage area was also investigated and the result showed a negative correlation in arid regions; whereas, no trend was observed in humid watersheds. This pattern indicates that the drainage density is uniformly distributed in humid regions which was also confirmed by investigating the variation of standard deviation of drainage density with climate aridity index.

# CHAPTER 5: HYDROLOGIC CONTROLS ON CHANNEL JUNCTION ANGLE

Channels emerge on landscapes as a result of flow forming concentrated erosion paths [*Horton*, 1945a; *Smith and Bretherton*, 1972; *Dietrich et al.*, 1993b]. In particular, when the surface resistance to erosion enforced by overland flow [*Dunne*, 1980; *Dietrich and Dunne*, 1993; *Hooshyar and Wang*, 2016] during rainfall events [*Hooshyar and Wang*, 2016], groundwater seepage [*Dunne*, 1990; *Abrams et al.*, 2009a], or shallow land sliding [*Dietrich et al.*, 1992a] is exceeded, channels begin to initiate. These erosional processes form drainage networks with branched structure which have been studied for decades [*Horton*, 1945a; *Leopold*, 1971; *Pelletier and Turcotte*, 2000; *Rodríguez-Iturbe and Rinaldo*, 2001; *Perron et al.*, 2012; *Hooshyar et al.*, 2017]. Junction angle is one of the main characteristics of drainage network related to basin dissection and network orientation [Howard, 1990] and has been shown to be correlated with other properties such as slope and discharge at the junction [*Horton*, 1932a; 1945a; *Howard*, 1971a; b; *Roy*, 1983].

*Horton* [1932a] proposed the first quantitative model for predicting the angle between the overland flow on the hillslope and the stream by relating it to the ratio of the main stream's gradient to that of the hillslope. *Horton* [1945a] utilized the same concept for predicting the angle between a major stream and a tributary. Despite its capability to capture the dependency of slope and junction angle [Lubowe, 1964], the Hortonian model is mathematically deficient as it predicts the angle of two streams with the same slope as zero

[*Howard*, 1971b]. To resolve this issue, *Howard* [1971b] generalized the Hortonian model by dividing the junction into two sub-junctions with respect to the axial prolongation of the main stream and used the Hortonian model to calculate the angle of sub-junctions. He further quantified the angle based on the discharge by relating the slope and discharge through a power function. In addition, *Howard* [1971b] proposed a new model based on the minimum power losses which gives the angle as a function of the discharge and slope. Roy [1983] revealed the optimality basis of the Hortonian model and its modified form by *Howard* [1971b] and showed that the Hortonian model is a special case of a general solution developed based on the minimum power losses. He also generalized the model using other optimality criteria and presented the angles based on the relative size of the tributaries. The discussed models typically require specific information about the tributaries (e.g., their slopes and relative size) in addition to the exponents of the power relationships between discharge and various variables such as slope, velocity, width and/or depth. Therefore, they do not provide the characteristic branching angles of specific flow regimes in the network.

*Devauchelle et al.* [2012a] studied the branching angle of channels formed by groundwater seepage and observed the angle as $\approx 72°$. This specific angle was found to be the stable growth direction enforced by flow from groundwater table represented by an infinite Laplacian field [*Devauchelle et al.*, 2012a; *Petroff et al.*, 2013]. The prediction by *Devauchelle et al.* [2012a] is general for the groundwater fed channels since it does not require any other information, e.g., slope and area.

In this study, we investigate the branching angles of natural drainage networks in 120 catchments across the United States and the observations are explained using the Optimal

Channel Network (OCN) concept [Rinaldo et al., 1992; Rodriguez‐Iturbe et al., 1992; Rodríguez‐Iturbe et al., 1992; Rodríguez-Iturbe and Rinaldo, 2001]. The junction angles are quantitatively related to the exponent of the slope-area curve through a mathematical optimization in a fan-shaped junction geometry. The model predicts a characteristic angle for each scaling regime in the slope-area curve solely based on the scaling exponent. The theoretical findings show reasonable agreements with the observations from 14,771 junctions in the study catchments.

The remaining of the chapter is organized as follows. Section 2 provides information about the study sites. The methods, including the drainage network extraction, junction angle calculation and the derivation of optimal junction angle, are presented in Section 3. The results and the physical explanation of the observation are provided in Section 4. Section 5 summarizes and concludes the chapter.

## 5.1 Data set

In this study, 120 catchments in the United States were selected based on the LiDAR data availability and minimal human impacts on the land surface. The LiDAR point cloud were downloaded from a USGS public data base and processed to derive 1 m Digital Elevation Model (DEM) using ArcGIS. Figure 40 shows the locations of the study catchments which are distributed over 17 states. The drainage area of the catchments ranges from 0.04 $km^2$ to 3.5 $km^2$ with the average of 1.2 $km^2$. The mean annual precipitation varies from 123 $mm \cdot yr^{-1}$ to 3838 $mm \cdot yr^{-1}$, representing a wide range of climatic conditions.

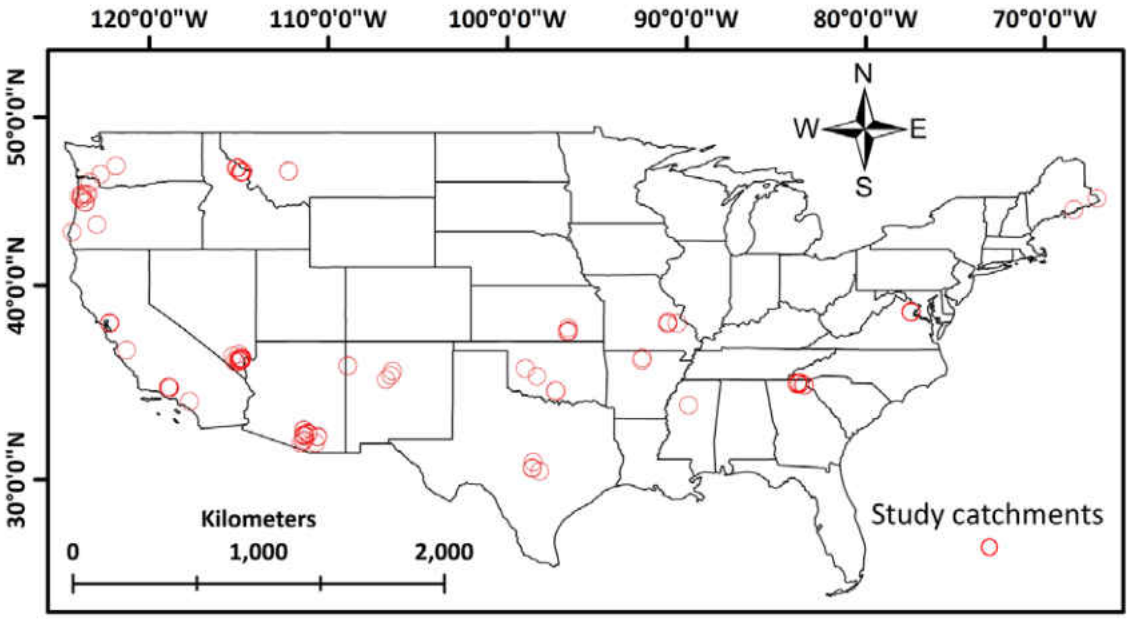


Figure 40. The locations of the 120 study catchments in the United Sates.

## 5.2 Methods

### 5.2.1 Valley network extraction

The drainage networks were extracted from 1 m LiDAR-based DEM using a curvature-based method proposed by *Hooshyar et al.* [2016b]. This method utilizes the Perona-Malik nonlinear diffusive filter [*Perona and Malik*, 1990] to smooth the DEM. The contour curvature is calculated from the filtered DEM and is used to objectively segment the terrain into valley and ridge patches, which are defined as the local maximums or minimums in the curvature grid. Using Otsu [1975]'s method, the non-valley and non-ridge patches are detected and filtered systematically to obtain the valley and ridge skeletons. Consequently, 1-pixel-wide valley lines are achieved by checking the existence of a ridge patch between two intersecting valleys. The method utilizes curvature-adjusted flow direction by modifying

the $D_\infty$-based [*Tarboton*, 1997a] flow direction grid which is calculated from the filled DEM using *O'callaghan and Mark* [1984a]'s method. The flow directions are rotated toward the pixel with higher local curvature (more convergent) which enhance the accuracy of the method to detect the valley path. The method requires two user-defined parameters for valley extraction including the time of forward diffusion ($T_F$) for filtering and the connecting threshold ($C_T$) which are set to 50 and 20 m, respectively. The contributing area and slope are used throughout the chapter to study the branching angle distribution and are calculated from the curvature-adjusted flow direction grid from the $D_\infty$ method [*Hooshyar et al.*, 2016b].

### 5.2.2 Junction angle calculation

Having the 1-pixel-wide valley network, the junctions are detected as the pixels with more than one immediate upstream pixels. Figure 41 shows four examples of junctions in a catchment located in northern Georgia. Intersecting valleys do not follow a linear path in most cases as shown in Figure 41; therefore, a linear function is fitted to the portion of the intersecting valleys with the length $L_f$ (measured from the junction). The branching angle is estimated as the angle between the fitted lines (Figure 41). Various values of $L_f$, ranging from 10 m to 30 m, are tested for each intersecting valley, and the one with the best linear fit to the valley (i.e., highest $R^2$), denoted by $L_f{}^*$, is used for calculating the angle.

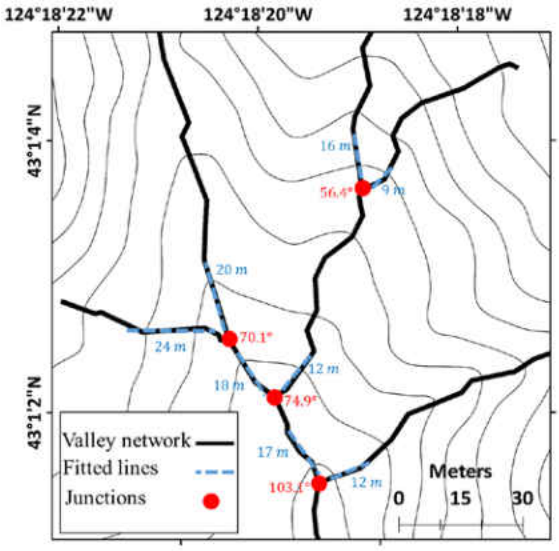


Figure 41. Junction examples in a catchment located in northern Georgia. The junctions are marked by red dots and the dashed-blue lines represent the fitted lines. The length ($L_f{}^*$) of the fitted line with the highest $R^2$ and the calculated angle at each junction are shown in blue and red texts, respectively.

## 5.3 Optimal junction angle

Several studies have characterized the landscape evolution as an optimization problem [Howard, 1990; Rigon et al., 1993; Rinaldo et al., 2014]. In particular, the Optimal Channel Network (OCN) [Rinaldo et al., 1992; Rodriguez - Iturbe et al., 1992; Rodríguez - Iturbe et al., 1992; Rigon et al., 1993; Rodríguez-Iturbe and Rinaldo, 2001; Rinaldo et al., 2014; Abed-Elmdoust et al., 2016] approach indicates that the natural channel configurations emerge in a way that the total energy dissipation is minimized. The energy dissipation rate $E_i$ for any link $i$ of the network, i.e., a channel segment with no junction in the middle, can be written as [Yang and Song, 1979]:

$$E_i = g(\rho Q_i + M_i) S_i L_i \tag{22}$$

where $g$ is gravitational acceleration and $\rho$ is water density. $Q_i$, $M_i$, $S_i$ and $L_i$ are the water discharge, sediment discharge, the average slope, and length along the link $i$. In natural drainage networks, $M_i$ is relatively small compared with $\rho Q_i$; therefore equation (22) can be expressed as:

$$E_i \propto Q_i S_i L_i \quad . \tag{23}$$

Assuming $Q_i \propto A_i$ and using the slope-area relationship $S_i \propto {A_i}^{-m}$, where $A_i$ is the contributing area at the end of link $i$, and $m$ is the exponent of the slope-area curve [Montgomery and Dietrich, 1988] which varies for debris-flow-dominated and alluvial channels [*Montgomery and Foufoula-Georgiou*, 1993] , equation (23) leads to:

$$E_i \propto L_i {A_i}^{\gamma} \tag{24}$$

where $\gamma = 1 - m$. The exponent $\gamma$ characterizes mechanics of erosional processes and ranges between zero and unity [Rodríguez-Iturbe and Rinaldo, 2001; Rinaldo et al., 2014].

Based on the OCN approach, the channel networks are obtained by minimizing total energy dissipation; therefore, they can be described using the following optimization problem:

$$min \sum_{i \in I} L_i {A_i}^{\gamma} \tag{25}$$

where I is the set of all the links in the network.

Figure 42a shows a schematic example of a 1st-order junction with angle denoted by α. The vertical and horizontal dimensions (representing basin shape) of the junction are denoted by $X$ and $Y$ and the distance of the junction from the upper bound (representing basin drainage divide) is given by $x$. Using a similar setup, Leopold [1971] argued that the Y-

shaped junctions, observed in the natural landscapes, create smaller total length and are more efficient in terms of water and sediment transport compared to T-shaped ($x = 0$) or V-shaped ($x = X$) ones. Figure 42b shows an extension of Figure 42a in terms of the contributing area and the length of the upstream ($A_u$ and $L_u$) and downstream links ($A_d$ and $L_d$). $\beta$ is the junction angle between downstream link and the neighboring tributary. For this plan view geometry, for simplification, it is assumed that the channels have equal distance from the confining ridges and the upper bound of the domain has a circular shape.

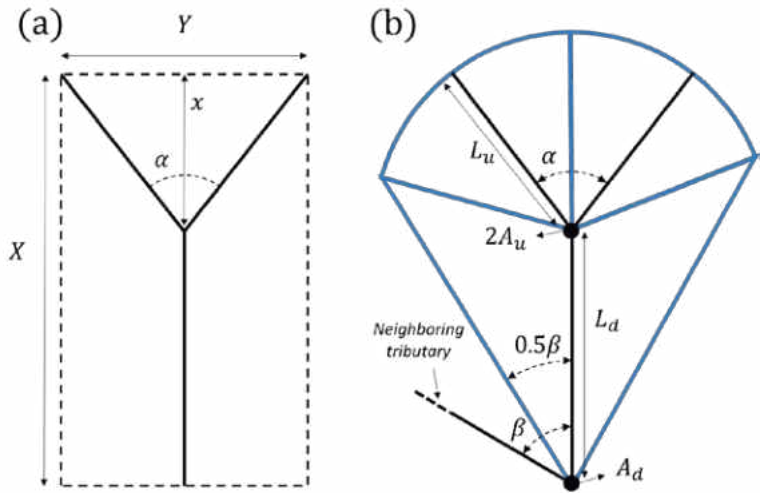


Figure 42. (a) A symmetric junction with the vertical and horizontal dimensions denoted by $X$ and $Y$. (b) The contributing area and the length of the upstream ($A_u$ and $L_u$) and downstream reaches ($A_d$ and $L_d$). The junction angle is denoted as $\alpha$, and $\beta$ represents the junction angle between downstream link and the channel within the neighbouring tributary.

Given X, Y and assuming constant total contributing area (area confined by the blue lines in Figure 42b), the optimal angle is the one yielding the minimum energy dissipation rate. Based on the setup given in Figure 42b, one can write the total energy function as:

$$E(\alpha, X, Y) \propto 2L_u \boldsymbol{A_u}^{\gamma} + L_d \boldsymbol{A_d}^{\gamma} \quad (26)$$

where $\boldsymbol{A_u}$ and $\boldsymbol{A_d}$ are normalized $A_u$ and $A_d$ by the total contributing area, since the total catchment area is assumed to be a constant. $L_u$, $A_u$, $L_d$, and $A_d$ can be expressed as functions of $\alpha$, $X$ and/or $Y$:

$$L_u = \frac{Y}{2} csc \frac{\alpha}{2} \tag{27}$$

$$A_u = \alpha \frac{Y^2}{8} csc^2 \frac{\alpha}{2} \tag{28}$$

$$L_d = X - \frac{Y}{2} cot \frac{\alpha}{2} \tag{29}$$

$$A_d = \alpha \frac{Y^2}{4} csc^2 \frac{\alpha}{2} + XY \cos \frac{\alpha}{2} - \frac{Y^2}{2} \cos^2 \frac{\alpha}{2} \csc \frac{\alpha}{2} \tag{30}$$

α is given as a function of x and Y (Figure 42a):

$$\alpha = 2 \cot^{-1} \frac{2x}{Y} \tag{31}$$

The optimal junction angle is denoted as $\hat{\alpha}$, which can be calculated as a function of $\gamma$ and $r = \frac{X}{Y}$ by setting $\frac{dE}{d\alpha}(\alpha = \hat{\alpha}) = 0$. This leads to:

$$\frac{1}{2} csc \frac{\hat{\alpha}}{2} cot \frac{\hat{\alpha}}{2} \left(2 + \frac{4}{\hat{\alpha}} r \sin \frac{\hat{\alpha}}{2} \sin \hat{\alpha} - \frac{2}{\hat{\alpha}} \cos \frac{\hat{\alpha}}{2} \sin \hat{\alpha}\right)^{-\gamma} - \gamma \, csc \frac{\hat{\alpha}}{2} \left(2 + \frac{4}{\hat{\alpha}} r \sin \frac{\hat{\alpha}}{2} \sin \hat{\alpha} - \frac{2}{\hat{\alpha}} \cos \frac{\hat{\alpha}}{2} \sin \hat{\alpha}\right)^{-\gamma-1} \left\{\left[\left(\frac{2r\hat{\alpha}+2}{\hat{\alpha}^2}\right) \cos \frac{\hat{\alpha}}{2} + \left(\frac{\hat{\alpha}-4r}{\hat{\alpha}^2}\right) \sin \frac{\hat{\alpha}}{2}\right] \sin \hat{\alpha} + \left(\frac{4r}{\hat{\alpha}} \sin \frac{\hat{\alpha}}{2} - \frac{2}{\hat{\alpha}} \cos \frac{\hat{\alpha}}{2}\right) \cos \hat{\alpha}\right\} + \frac{1}{4} \csc^2 \frac{\hat{\alpha}}{2} = 0 \tag{32}$$

Figure 43a shows $\hat{\alpha}$ for different values of $r$ and $\gamma$. For a given value of $r$, increasing $\gamma$ results in wider angle, suggesting that the junction angle decreases with increasing $\gamma$.

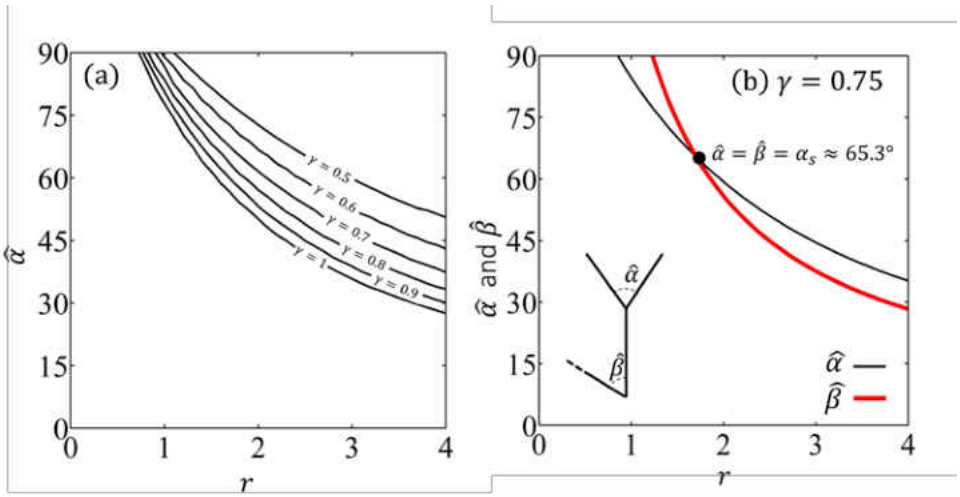


Figure 43. (a) The optimal junction angle $\hat{\alpha}$ for various values of $\gamma$ and $r$; (b) The optimal angle ($\hat{\alpha}$) and the downstream angle ($\hat{\beta}$) when $\gamma = 0.75$. Two curves intersect at $\hat{\alpha} = \hat{\beta} \approx 65.3°$. The intersection is denoted by $\alpha_s$. This indicates that if $\gamma = 0.75$, the stable branching angle would be $\alpha_s = 65.3°$.

As shown in Figure 42b, β is the junction angle between the downstream link and the channel within the neighboring tributary. Assuming that the flow separation line (ridge) is located at an equal distance from both channels, $\beta$ can be expressed as a function of $\alpha$ and $r$:

$$\beta = 2\sin^{-1}\left\{\frac{1}{2}\csc\frac{\alpha}{2}\sin\alpha\left[\left(\frac{1}{2}\csc\frac{\alpha}{2}\right)^2 + \left(r - \frac{1}{2}\cot\frac{\alpha}{2}\right)^2 + 2\left(\frac{1}{2}\csc\frac{\alpha}{2}\right)\left(r - \frac{1}{2}\cot\frac{\alpha}{2}\right)\cos\alpha\right]^{-\frac{1}{2}}\right\} \qquad (33)$$

Defining $\hat{\beta}$ as the downstream angle corresponding to optimal angle $\hat{\alpha}$, $\hat{\beta}$ can be expressed as a function of $r$ and $\gamma$ similar to $\hat{\alpha}$ by substituting $\hat{\alpha}$ from equation (32) into equation (33). As an example, Figure 43b shows $\hat{\alpha}$ and $\hat{\beta}$ for different $r$ when $\gamma = 0.75$. If both upstream and downstream junctions have similar hydrologic and geomorphologic conditions, one can expect $\hat{\alpha} = \hat{\beta}$ for a homogeneous landscape. For $\gamma = 0.75$ the two curves in Figure 43b intersect at $\hat{\alpha} = \hat{\beta} \approx 65.3°$. This suggests that if $\gamma = 0.75$, the stable branching

angle would be $\alpha_s = 65.3°$ and for any given γ (equivalently m $= 1 -$ γ), one can find the specific branching angle. Figure 44 shows the relationship between $\alpha_s$ and $m = 1 - \gamma$. Higher values of $m$ correspond to alluvial channels where the branching angle is relatively larger than the debris-flow-dominated channels.

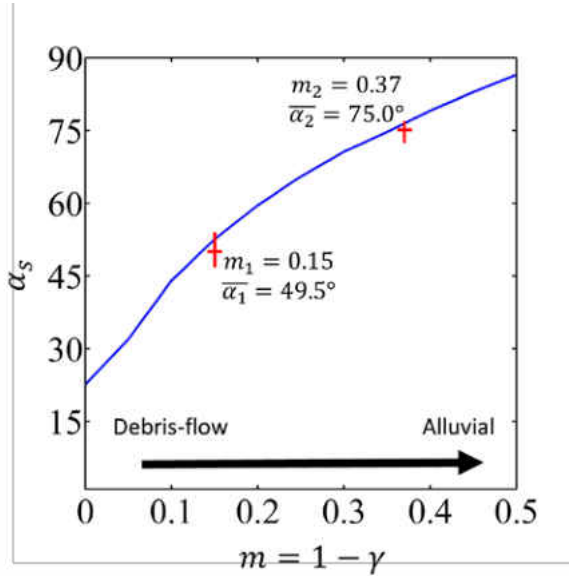


Figure 44. $\alpha_s$ for different values of $m = 1 - \gamma$, where $m$ is the exponent of slope-area relationship ($S \propto A^{-m}$). The crosses represent the characteristic angles for debris-flow dominated and fluvial regimes based on the observations in the study catchments. The vertical line at each point correspond to the range of the characteristic angles quantified using different approaches (GMM, angle-area curve and slope-area curve; see section 4.1) and reflects the uncertainty.

## 5.4 Results and discussions

In total, there were 14,771 junctions in the 120 study catchments. Figure 45 shows an example of the extracted valley network and the computed junction angles in a catchment located in northern Georgia. As mentioned in Section 3.2, linear functions were fitted to a portion of valley line with the length $L_f{}^*$ and were used to calculate the branching angle. $L_f{}^*$

is the length, ranging from 10 m to 30 m, that results in the highest $R^2$ value and was calculated for each intersecting valley. The mean and the standard deviation of ${L_f}^*$ are 20.2 m and 7.6 m, respectively; whereas, the mean and the standard deviation of $R^2$ for the linear fits for ${L_f}^*$ are 0.92 and 0.11, respectively.

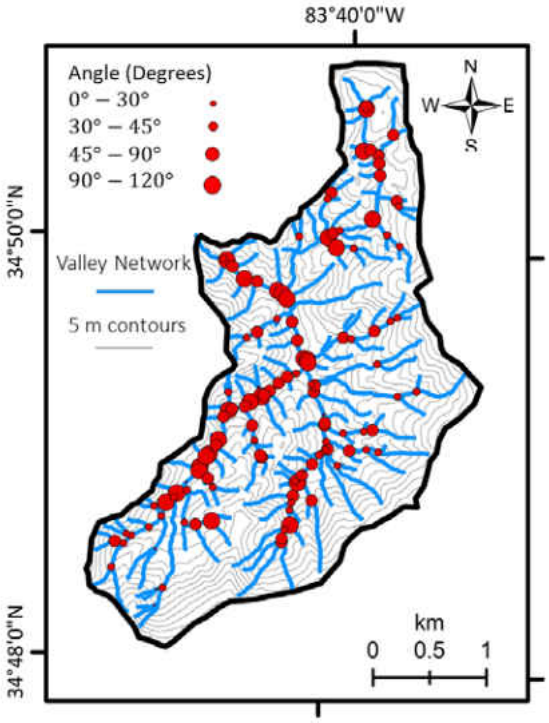


Figure 45. The valley network and the junction angles for a drainage network located in northern Georgia, United States.

### 5.4.1 Observations

From the extracted drainage networks, the branching angles in the study sites were measured as $61.8° \mp 27.1°$ (average $\mp$ one standard deviation). Figure 46a shows the probability distribution function (PDF) of the observed junction angle ($\alpha_{obs}$) using a bin size

of 5°. The PDF is right-skewed with a skewness of $S_k = 0.27$. This may be due to the multi-modal behavior of the PDF where each mode represents the angle distribution corresponding to a specific physical condition. Assuming that modes are normally distributed, as observed by *Devauchelle et al.* [2012a] for groundwater-fed channels, one can represents the PDF in Figure 46a as a Gaussian Mixture Model (GMM). Figure 46b shows the extracted modes of the original PDF using the Expectation-Maximization (EM) algorithm [*Moon*, 1996b]. The extracted modes exhibit the averages of 47.0° and 76.6° with the standard deviations of 24.5°and 22.4°, respectively.

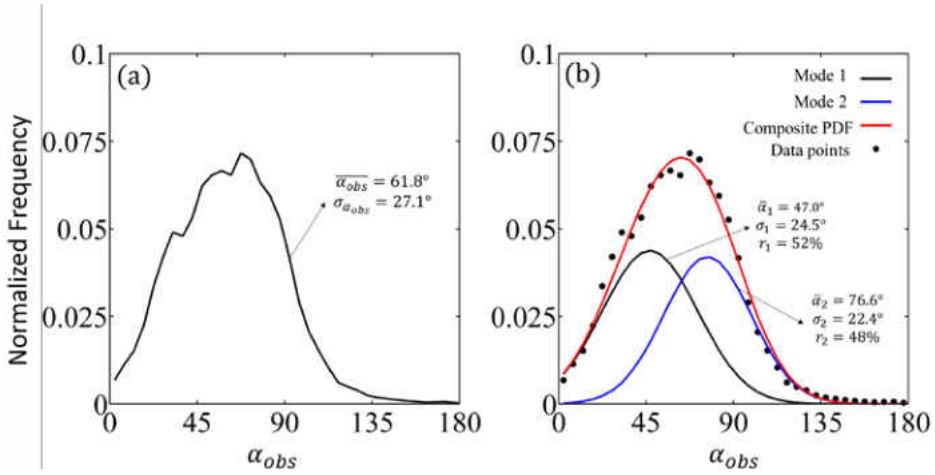


Figure 46. (a) The PDF of the observed junction angle ($\alpha_{obs}$) using a bin size of 5°. (b) The decomposed PDFs from (a) using the Expectation-Maximization algorithm. The extracted modes exhibit the averages of 47.0°and 76.6° with the standard deviations of 24.5°and 22.4°, respectively.

The relationship between the observed junction angle ($\alpha_{obs}$) and the contributing area to the end of the intersecting valleys (A) is shown in Figure 47. As can be seen from this figure, for large contributing area, i.e., higher order channels located downstream of the catchments, the angle is observed to be around 75.8°. At the other end, the junctions with

small contributing area and located higher up in the catchments, are found to branch in a relatively smaller angle (≈ 54.0°).

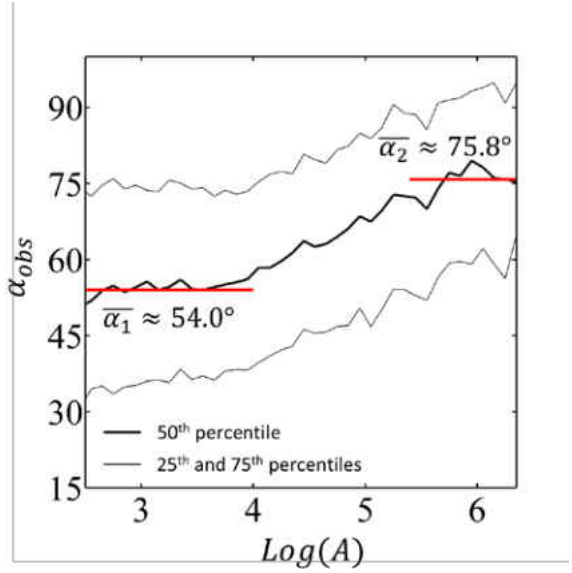


Figure 47. The observed junction angle ($\alpha_{obs}$) versus the contributing area ($A$). The curves represent 25$^{th}$ , 50$^{th}$ and 75$^{th}$ percentiles, respectively. The junction angle starts from 54.0° (the average of the 50$^{th}$ percentile for $2.5 \leq Log(A) \leq 3.9$) for small contributing area and approaches to 75.8° (the average of the 50$^{th}$ percentile for $5.5 \leq \text{Log(A)} \leq 6.4$), where the transitions are visually identified.

Figure 48a shows the slope-area curve in the study sites. A is the contributing area to the end of the valley, and $S$ is the average slope along the valley defined as the relief divided by the length. The slope-area curve exhibits log-log linear relationships and in fact has two scaling regimes with the exponents $m_1 = 0.15$ and $m_2 = 0.37$, where $S \propto A^{-m}$, and the transition occurs at $A_T = 10^{3.9}$ m$^2$. The exponents and the transitional area threshold are objectively extracted by maximizing the product of $R^2$ for two linear fits. The first scaling regime is attributed to the debris-flow-dominated [*Montgomery and Foufoula-Georgiou*, 1993; *Singh et al.*, 2015] which is the main flow regime near the channel heads; and the

second one corresponds to the fluvial regime. The angles are divided into two groups based on the area threshold extracted from the slope-area curve ($A_T = 10^{3.9}$ m$^2$). The angle PDFs for the two groups are shown in Figure 48b, and the peaks for the two groups are at ≈ 47.5° and ≈ 72.5°.

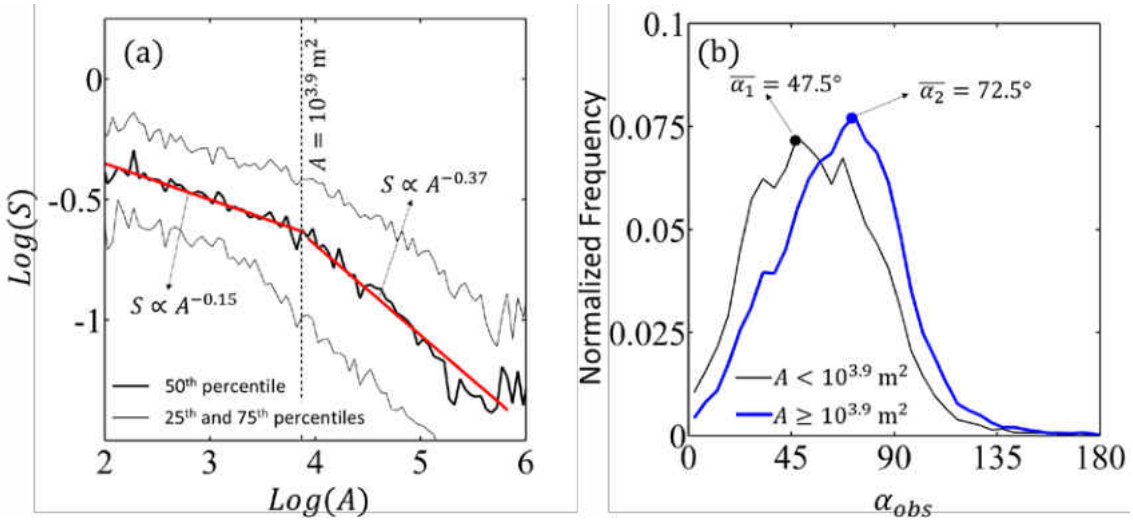


Figure 48. (a) The slope-area curve for the study sites. The curve exhibits log-log linear relationships with the exponents $m_1 = 0.15$ and $m_2 = 0.37$. The transition occurs at $A_T = 10^{3.9}$ m$^2$. (b) The junction angle distributions for $A < A_T$ and $A \geq A_T$.

### 5.4.2 Explanation based on minimum energy dissipation

Figures 7b, 8 and 9b clearly indicate that the junction angles in the study catchments have two distinct modes which may correspond to specific geomorphologic conditions. Based on the concept of minimum energy dissipation, the junction angle varies with the exponent of the slope-area curve (Figure 5). Here, we hypothesize that the two observed modes in the angle distribution are attributed to the two scaling regimes in the slope-area curve. The first mode corresponds to those junctions located upstream of the catchments

and attributes to the debris-flow dominated regime with a scaling exponent of $m_1 = 0.15$. The second mode is related to the fluvial regime with $m_2 = 0.37$. There is uncertainty in evaluating the characteristic angles. Table 6 summarizes the identified angles associated with the two modes by the three methods: GMM (Figure 7b), angle-area curve (Figure 8), and slope-area curve (Figure 9b). The average angles of modes over the three methods are $\overline{\alpha_1} \approx 49.5°$ and $\overline{\alpha_2} \approx 75.5°$, which are used as the best estimations of the characteristic angles associated with the two modes.

Table 6. The characteristic angles extracted from three methods.

| | **Mode 1 Debris-flow dominated** | **Mode 2 Fluvial regime** |
|---|---|---|
| **GMM** | 47.0° | 76.6° |
| **Angle-area curve** | 54.0° | 75.8° |
| **Slope-area curve** | 47.5° | 72.5° |
| **Average** | 49.5° | 75.0° |
| **Max** | 54° | 76.6° |
| **Min** | 47° | 72.5° |

In order to verify the derived relationship between junction angle and $m$, the two modes are added to the $\alpha_s \sim m$ curve shown in Figure 5. The first mode is located at $m_1 = 0.15$ and $\overline{\alpha_1} \approx 49.5°$ and corresponds to the debris-dominated-flow channels as discussed before. The second mode is attributed to the fluvial regime with $m_1 = 0.37$ and $\overline{\alpha_1} \approx 75.0°$. The maximums and minimums at each point are also shown as the vertical lines to visualize the uncertainty. Both points are close to the $\alpha_s \sim m$ curve which indicates that the modes in the angle distribution may be attributed to the scaling regimes characterized by the slope-area curve.

## 5.5 Conclusion

Networks with branching structure are common in different areas such as social networks [*Hajibagheri et al.*, 2013; *Hajibagheri et al.*, 2016], energy systems [*Alirezaei et al.*, 2016], infrastructures [*Madani and Hooshyar*, 2014; *Madani et al.*, 2014], and hydrology in form of natural drainage networks. Drainage networks are important hydrologic and geomorphologic features which have been studied extensively in past decades. The branching angle directly controls the topology of these networks and holds important information on the underlying physical mechanisms that form the drainage network. In this study, the junction angle of 120 catchments in the United States with the total of 14,771 junctions was studied. Investigating the variation of angles in the study catchments revealed the existence of two distinct characteristic angles.

The observed angles were linked to the scaling exponents of the slope-area curve through the theory of Optimal Channel Network (OCN) or minimum energy dissipation. To do so, an optimization was formulated for a fan-shaped junction geometry and the optimal angle was calculated by minimizing the energy dissipation rate on the network link. The optimization led to a relationship between junction angles and the scaling exponent of the slope-area curve which showed reasonable agreement with the observations. This indicates that the flow regimes, characterized by the slope-area curve as debris-flow dominated or fluvial, have distinct signatures on the network topology and junction angles.

The plan view geometry, used for formulating the optimization, assumes that the channels have equal distance from the confining ridges and the upper bound of the domain has a circular shape. Although, this fan-shaped geometry is common in natural drainage

networks, there also exist catchments with other shapes and often highly asymmetric. The connection between the catchment's shape and asymmetry on the branching angle will be the topic of future research. The proposed optimization framework is based on the assumption $Q \propto A$ which has been argued to be reasonable for runoff due to overland flow rather than groundwater seepage.

# CONCLUSION

Drainage network is an important geomorphologic and hydrologic feature which significantly controls runoff generation and is vitally important for practical water resource management. Consisting of valleys and channels [*Montgomery and Foufoula-Georgiou*, 1993], drainage networks can be characterized by drainage density ($D_d$) which is defined as the ratio of the total length of channels in a watershed to its drainage area [*Horton*, 1932b; 1945b] and has been a topic of significant research for past several decades. From geomorphologic perspective, the transition from valley to channel (i.e., channel heads) in drainage network can be quantified via various thresholds, for e.g., upslope area and curvature. From hydrologic perspective, channels are categorized as perennial, intermittent, and ephemeral streams based on the flow durations. Perennial streams flow for the most of the time during normal years and are maintained by groundwater discharge. Intermittent (i.e. seasonal) streams flow during certain times of the year receiving water from surface sources such as melting snow or from groundwater sources such as springs. Lastly, ephemeral streams flow only in direct response to precipitation without continuous surface flow [Meinzer, 1923]. A longstanding question is whether these hydrologically characterized channels leave distinctive signatures on topology and geomorphology of the networks. Understanding the impacts of climate and hydrology on geomorphology and topology of drainage networks is essential for predicting the evolution of land surface.

The first step to study the drainage networks is accurately extract them from DEMs. Here, the basic definitions of channels and valleys were used to identify them in high-

resolution DEMs. Valleys are defined as convergent topography in the landscape, and the convergence is naturally associated with positive contour curvature. An automatically derived curvature threshold was proposed to differentiate significant convergence, significant divergence, and insignificant features. Significant convergent cells form a valley skeleton and significant divergent cells define ridge patches. With the valley skeleton and ridge patches extracted, the valley network was generated by removing valley tributaries that are not confined by at least one ridge patch. Channels are generally surrounded by well-defined banks that have a distinct signature in the contours. A new method was proposed to automatically extract channel heads based on the clustering of contours, utilizing the information derived from the entire cross-section. The similarity-based clustering method eliminates the need for a spatially constant channel initiation threshold. The proposed method was able to capture the spatial variation of channel initiation curvature threshold.

The temporal dynamics of stream networks are vitally important for understanding hydrologic processes including surface water and groundwater interaction and hydrograph recession. A systematic method was developed to map wet channel networks by integrating elevation and signal intensity of ground returns. The signal intensity thresholds for identifying wet pixels were extracted from frequency distributions of intensity return within the convergent topography extent using a Gaussian mixture model. A power-law relationship between streamflow and wetted channel length during recession periods was derived.

In a pioneer work, Abrahams [1984] proposed a U-shaped relationship between drainage density and climate aridity index, defined as the ratio of the mean annual potential

evaporation to the mean annual precipitation. However, our result showed an increasing trend in arid regions, which is consistent with the observations in other studies, and no trend in humid watersheds. The decreasing trend observed in humid watersheds by Madduma Bandara [1974] can be explained considering the specific vegetation cover in that area. Those watersheds have been modified by extensive human interferences and the natural vegetation has been eliminated due to tea plantation. Therefore, the erosive force increases as the climate gets more humid while the resistance due to vegetation cover remains constant which increases the drainage density. Our finding suggests that the erosive force and the resistance due to vegetation reach an equilibrium in humid regions and the change in climate conditions does not systematically impact the drainage network. Whereas, in arid region, the increase in resistive force of vegetation dominates the escalation of erosive force of runoff which leads to a decreasing trend in drainage density. Our finding also suggests that natural drainage networks in arid regions are more sensitive to the change in long-term climate conditions compared with the watersheds located in humid regions. In a broader sense, this influence our understanding of the formation of drainage networks and the response of hydrologic systems to climate change.

The formation and growth of river channels and their network evolution are governed by the erosional and depositional processes operating on the landscape due to movement of groundwater [*Dunne*, 1990; *Abrams et al.*, 2009b] and/or surface runoff [*Horton*, 1945b; *Dunne*, 1990]. Recent research has shown groundwater flow controls on channel junction angles [*Devauchelle et al.*, 2012b]; however, the role of surface runoff is still not clear. Surface runoff dominated channels receive water from sources such as melting

snow or overland flow during rainfall events [Levick et al., 2008]. Based on channel networks extracted from 1 m DEMs of 120 catchments with minimal human impacts across the United States, we showed that the junction angles have two modes with $\overline{\alpha_1} \approx 49.5°$ and $\overline{\alpha_2} \approx 75.0°$. The latter is close to the branching angle of the groundwater fed channels ($\alpha_g \approx 72°$) [*Devauchelle et al.*, 2012b]. The observed angles were physically explained as the optimal angles that result in minimum energy dissipation and were linked to the exponent characterizing slope-area curve [Montgomery and Dietrich, 1988]. These findings enable us to understand the geomorphologic signature of hydrologic processes on drainage networks and develop more refined landscape evolution models.

# REFERENCES


Abed-Elmdoust, A., M. A. Miri, and A. Singh (2016), Reorganization of river networks under changing spatiotemporal precipitation patterns: An optimal channel network approach, *Water Resour. Res.*, *52*, In press, doi: 10.1002/2015WR018391.

Abrahams, A. D. (1984), Channel networks: a geomorphological perspective, *Water Resources Research*, *20*(2), 161-188, doi: 10.1029/wr020i002p00161

Abrams, D. M., A. E. Lobkovsky, A. P. Petroff, K. M. Straub, B. McElroy, D. C. Mohrig, A. Kudrolli, and D. H. Rothman (2009a), Growth laws for channel networks incised by groundwater flow, *Nat. Geosci.*, *2*(3), 193-196.

Abrams, D. M., A. E. Lobkovsky, A. P. Petroff, K. M. Straub, B. McElroy, D. C. Mohrig, A. Kudrolli, and D. H. Rothman (2009b), Growth laws for channel networks incised by groundwater flow, *Nature Geoscience*, *2*(3), 193-196.

Acuña, V., T. Datry, J. Marshall, D. Barceló, C. Dahm, A. Ginebreda, G. McGregor, S. Sabater, K. Tockner, and M. Palmer (2014), Why should we care about temporary waterways, *Science*, *343*(6175), 1080-1081, doi: 10.1126/science.1246666.

Alirezaei, M., M. Noori, and O. Tatari (2016), Getting to net zero energy building: Investigating the role of vehicle to home technology, *Energy and Buildings*, *130*, 465-476, doi: http://doi.org/10.1016/j.enbuild.2016.08.044.

Alirezaei, M., N. Onat, O. Tatari, and M. Abdel-Aty (2017), The Climate Change-Road Safety-Economy Nexus: A System Dynamics Approach to Understanding Complex Interdependencies, *Systems*, *5*(1), 6.

Antonarakis, A., K. S. Richards, and J. Brasington (2008), Object-based land cover classification using airborne LiDAR, *Remote Sensing of Environment*, *112*(6), 2988-2998.

Band, L. E. (1986), Topographic Partition of Watersheds with Digital Elevation Models, *Water Resources Research*, *22*(1), 15-24, doi: 10.1029/WR022i001p00015.

Beeson, P., D. Miller, and C. Duffy (2011), Identifying ephemeral and perennial stream reaches using apparent thermal inertia of an ungauged basin in Central New Mexico, *Geocarto International*, *26*(3), 183-194, doi: 10.1080/10106049.2011.553290

Beven, K., and M. J. Kirkby (1979), A physically based, variable contributing area model of basin hydrology/Un modèle à base physique de zone d'appel variable de l'hydrologie du bassin versant, *Hydrological Sciences Journal*, *24*(1), 43-69.

Biswal, B., and M. Marani (2010), Geomorphological origin of recession curves, *Geophysical Research Letters*, *37*(24), doi: 10.1029/2010gl045415

Blyth, K., and J. Rodda (1973), A stream length study, *Water Resources Research*, *9*(5), 1454-1461, doi: 10.1029/wr009i005p01454

Bowen, Z. H., and R. G. Waltermire (2002), Evaluation of light detection and ranging (LiDAR) for measuring RWER corridor topography, *Journal of the American Water Resources Association*, *38*(1), doi: 10.1111/j.1752-1688.2002.tb01532.x

Brzank, A., C. Heipke, J. Goepfert, and U. Soergel (2008), Aspects of generating precise digital terrain models in the Wadden Sea from lidar–water classification and structure line extraction, *ISPRS Journal of Photogrammetry and Remote Sensing*, *63*(5), 510-528, doi: 10.1016/j.isprsjprs.2008.02.002.

Budyko, M. I. (1971), *Climate and life*, Academic Press, New York.

Camporese, M., C. Paniconi, M. Putti, and S. Orlandini (2010), Surface - subsurface flow modeling with path - based runoff routing, boundary condition - based coupling, and assimilation of multisource observation data, *Water Resources Research*, *46*(2), doi: 10.1029/2008wr007536

Canny, J. (1986), A computational approach to edge detection, *Pattern Analysis and Machine Intelligence, IEEE Transactions on*(6), 679-698, doi: 10.1016/b978-0-08-051581-6.50024-6

Carlston, C. W. (1963), *Drainage density and streamflow*, US Geological Survey Professional Paper 422-C, Washington, DC.

Chen, X., N. Alimohammadi, and D. Wang (2013), Modeling interannual variability of seasonal evaporation and storage change based on the extended Budyko framework, *Water Resources Research*, *49*(9), 6067-6078.

Clubb, F. J., S. M. Mudd, D. T. Milodowski, M. D. Hurst, and L. J. Slater (2014), Objective extraction of channel heads from high-resolution topographic data, *Water Resources Research*, *50*(5), 4283-4304, doi: 10.1002/2013WR015167.

Coats, R. N., and C. R. Goldman (2001), Patterns of nitrogen transport in streams of the Lake Tahoe Basin, California - Nevada, *Water Resources Research*, *37*(2), 405-415, doi: 10.1029/2000wr900219

Collins, D., and R. Bras (2010), Climatic and ecological controls of equilibrium drainage density, relief, and channel concavity in dry lands, *Water Resources Research*, *46*(4).

Daly, C., R. P. Neilson, and D. L. Phillips (1994), A statistical-topographic model for mapping climatological precipitation over mountainous terrain, *Journal of Applied Meteorology*, *33*(2), 140-158.

Day, D. (1978), Drainage density changes during rainfall, *Earth Surface Processes*, *3*(3), 319-326, doi: 10.1002/esp.3290030310

Dettinger, M. D. (2013), Projections and downscaling of 21st century temperatures, precipitation, radiative fluxes and winds for the Southwestern US, with focus on Lake Tahoe, *Climatic Change*, *116*(1), 17-33, doi: 10.1007/s10584-012-0501-x

Devauchelle, O., A. P. Petroff, H. F. Seybold, and D. H. Rothman (2012a), Ramification of stream networks, *Proc. Natl. Acad. Sci. U.S.A.*, *109*(51), 20832-20836.

Devauchelle, O., A. P. Petroff, H. F. Seybold, and D. H. Rothman (2012b), Ramification of stream networks, *Proceedings of the National Academy of Sciences*, *109*(51), 20832-20836.

Di Lazzaro, M., A. Zarlenga, and E. Volpi (2015), Hydrological effects of within-catchment heterogeneity of drainage density, *Advances in Water Resources*, *76*, 157-167.

Dietrich, W. E., and T. Dunne (1993), The channel head, in *Channel network hydrology*, edited by K. Beven and M. Kirby, pp. 175-219, John Wiley and Sons, New Jersey, U.S.A.

Dietrich, W. E., S. Reneau, and C. Wilson (1987), Overview: Zero-order basins and problems of drainage density, sediment transport and hillslope morphology, *IAHS-AISH publication*(165), 27-37.

Dietrich, W. E., C. J. Wilson, D. R. Montgomery, and J. McKean (1993a), Analysis of erosion thresholds, channel networks, and landscape morphology using a digital terrain model, *The Journal of Geology*, 259-278.

Dietrich, W. E., C. J. Wilson, D. R. Montgomery, and J. McKean (1993b), Analysis of erosion thresholds, channel networks, and landscape morphology using a digital terrain model, *J. Geol.*, 259-278.

Dietrich, W. E., C. J. Wilson, D. R. Montgomery, J. McKean, and R. Bauer (1992a), Erosion thresholds and land surface morphology, *Geol.*, *20*(8), 675-679.

Dietrich, W. E., C. J. Wilson, D. R. Montgomery, J. McKean, and R. Bauer (1992b), Erosion thresholds and land surface morphology, *Geology*, *20*(8), 675-679.

Do, C. B., and S. Batzoglou (2008), What is the expectation maximization algorithm?, *Nature biotechnology*, *26*(8), 897-900, doi: 10.1038/nbt1406

Dunne, T. (1980), Formation and controls of channel networks, *Prog. in Phys. Geogr.*, *4*(2), 211-239.

Dunne, T. (1990), *Hydrology, mechanics and geomorphic implications of erosion by subsurface flow*, 1-28 pp., Geological Society of America.

Dunne, T., and L. Leopold (1978), Water in environment planning, edited, Freeman, San Francisco.

Evans, I. (1979), An integrated system of terrain analysis and slope mapping. Final Report (Report 6) on Grant DA-ERO-591-73-G0040, *Statistical Characterization of Altitude Matrices by Computer*.

Gardiner, V., K. Gregory, and D. Walling (1977), Further notes on the drainage density-basin area relationship, *Area*, *9*(2), 117-121.

Genc, L., S. Smith, and B. Dewitt (2005), Using satellite imagery and LIDAR data to corroborate an adjudicated ordinary high water line, *International journal of remote sensing*, *26*(17), 3683-3693, doi: 10.1080/01431160500165922

Ghosh, D. K., D. Wang, and T. Zhu (2016), On the transition of base flow recession from early stage to late stage, *Advances in Water Resources*, *88*, 8-13.

Godsey, S., and J. Kirchner (2014), Dynamic, discontinuous stream networks: hydrologically driven variations in active drainage density, flowing channels and stream order, *Hydrological Processes*, *28*(23), 5791-5803, doi: 10.1002/hyp.10310

Goulsbra, C., M. Evans, and J. Lindsay (2014), Temporary streams in a peatland catchment: pattern, timing, and controls on stream network expansion and contraction, *Earth Surface Processes and Landforms*, *39*(6), 790-803, doi: 10.1002/esp.3533.

Gregory, K., and D. Walling (1968), The variation of drainage density within a catchment, *Hydrological Sciences Journal*, *13*(2), 61-68, doi: 10.1080/02626666809493583.

Gregory, K., and V. Gardiner (1975), Drainage density and climate, *Zeitschrift fur Geomorphologie*, *19*(3), 287-298.

Gregory, K. J., and D. E. Walling (1973), *Drainage basin form and process: A geomorphological approach*, John Wiley and Sons, New York.

Gurnell, A. (1978), The dynamics of a drainage network, *Nordic Hydrology*, *9*(5), 293-306.

Hajibagheri, A., A. Hamzeh, and G. Sukthankar (2013), Modeling information diffusion and community membership using stochastic optimization, paper presented at 2013 IEEE/ACM International Conference on Advances in Social Networks Analysis and Mining (ASONAM 2013), 25-28 Aug. 2013, doi: 10.1145/2492517.2492545.

Hajibagheri, A., G. Sukthankar, and K. Lakkaraju (2016), Leveraging Network Dynamics for Improved Link Prediction, in *Social, Cultural, and Behavioral Modeling: 9th International Conference, SBP-BRiMS 2016, Washington, DC, USA, June 28 - July 1, 2016, Proceedings*, edited by K. S. Xu, D. Reitter, D. Lee and N. Osgood, pp. 142-151, Springer International Publishing, Cham, doi: 10.1007/978-3-319-39931-7_14.

Hilldale, R. C., and D. Raff (2008), Assessing the ability of airborne LiDAR to map river bathymetry, *Earth Surface Processes and Landforms*, *33*(5), 773-783, doi: 10.1002/esp.1575

Höfle, B., M. Vetter, N. Pfeifer, G. Mandlburger, and J. Stötter (2009), Water surface mapping from airborne laser scanning using signal intensity and elevation data, *Earth Surface Processes and Landforms*, *34*(12), 1635-1649, doi: 10.1002/esp.1853

Hooshyar, M., and D. Wang (2016), An analytical solution of Richards' equation providing the physical basis of SCS curve number method and its proportionality relationship, *Water Resources Research*, *52*(8), 6611-6620.

Hooshyar, M., A. Singh, and D. Wang (2017), Hydrologic controls on junction angle of river networks, *Water Resources Research*, 00.

Hooshyar, M., S. Kim, D. Wang, and S. C. Medeiros (2015), Wet channel network extraction by integrating LiDAR intensity and elevation data, *Water Resources Research*, *51*(12), 10029-10046.

Hooshyar, M., S. C. Medeiros, D. Wang, and S. C. Hagen (2016a), A Dual EnKF for Estimating Water Level, Bottom Roughness, and Bathymetry in a 1-D Hydrodynamic Model, *arXiv preprint arXiv:1607.00569*.

Hooshyar, M., D. Wang, S. Kim, S. C. Medeiros, and S. C. Hagen (2016b), Valley and channel networks extraction based on local topographic curvature and k-means clustering of contours, *Water Resources Research*, *52*, 8081–8102, doi: 10.1002/2015WR018479.

Hopkinson, C., N. Crasto, P. Marsh, D. Forbes, and L. Lesack (2011), Investigating the spatial distribution of water levels in the Mackenzie Delta using airborne LiDAR, *Hydrological Processes*, *25*(19), 2995-3011, doi: 10.1002/hyp.8167

Horn, B. K. P. (1987), Closed-form solution of absolute orientation using unit quaternions, *J. Opt. Soc. Am. A*, *4*(4), 629-642, doi: 10.1364/JOSAA.4.000629.

Horton, R. E. (1932a), Drainage‐basin characteristics, *EOS, Trans. Am. Geophys. Union*, *13*(1), 350-361.

Horton, R. E. (1932b), Drainage‐basin characteristics, *Eos, Transactions American Geophysical Union*, *13*(1), 350-361.

Horton, R. E. (1945a), Erosional development of streams and their drainage basins; hydrophysical approach to quantitative morphology, *Geol. Soc. Am. Bull.*, *56*(3), 275-370.

Horton, R. E. (1945b), Erosional development of streams and their drainage basins; hydrophysical approach to quantitative morphology, *Geological Society of America Bulletin*, *56*(3), 275-370.

Howard, A. D. (1971a), Simulation of Stream Networks by Headword Growth and Branching, *Geogr. Anal.*, *3*(1), 29-50.

Howard, A. D. (1971b), Optimal angles of stream junction: Geometric, stability to capture, and minimum power criteria, *Water Resour. Res.*, *7*(4), 863-873.

Howard, A. D. (1990), Theoretical model of optimal drainage networks, *Water Resour. Res.*, *26*(9), 2107-2117.

Howard, A. D. (1994), A detachment-limited model of drainage basin evolution, *Water Resources Research*, *30*(7), 2261-2285, doi: 10.1029/94WR00757.

Ijjasz-Vasquez, E. J., and R. L. Bras (1995), Scaling regimes of local slope versus contributing area in digital elevation models, *Geomorphology*, *12*(4), 299-311.

Istanbulluoglu, E., and R. L. Bras (2005), Vegetation - modulated landscape evolution: Effects of vegetation on landscape processes, drainage density, and topography, *Journal of Geophysical Research: Earth Surface*, *110*(F2).

Kendall, M. (1975), Rank Correlation Methods, Griffin, London.

Kollet, S. J., and R. M. Maxwell (2006), Integrated surface–groundwater flow modeling: A free-surface overland flow boundary condition in a parallel groundwater flow model, *Advances in Water Resources*, *29*(7), 945-958, doi: 10.1016/j.advwatres.2005.08.006

Kosovich, J. J., R. W. Schaffranek, M. A. Stewart, D. J. Nowacki, J. R. Degnan, G. J. Walsh, S. Flanagan, and R. C. Burruss (2008), *State of Florida 1: 24,000-and 1: 100,000-Scale Quadrangle Index Map, Highlighting Low-lying Areas Derived from USGS Digital Elevation Models*, US Department of the Interior, US Geological Survey.

Lang, M. W., and G. W. McCarty (2009), Lidar intensity for improved detection of inundation below the forest canopy, *Wetlands*, *29*(4), 1166-1178, doi: 10.1672/08-197.1

Lashermes, B., E. Foufoula-Georgiou, and W. E. Dietrich (2007), Channel network extraction from high resolution topography using wavelets, *Geophysical Research Letters*, *34*(23), L23S04, doi: 10.1029/2007GL031140.

Le, P. V., and P. Kumar (2014), Power law scaling of topographic depressions and their hydrologic connectivity, *Geophysical Research Letters*, *41*(5), 1553-1559, doi: 10.1002/2013gl059114

Leopold, L. B. (1971), Trees and streams: the efficiency of branching patterns, *J. Theor. Biol.*, *31*(2), 339-354.

Levick, L. R., D. C. Goodrich, M. Hernandez, J. Fonseca, D. J. Semmens, J. C. Stromberg, M. Tluczek, R. A. Leidy, M. Scianni, and D. P. Guertin (2008), *The ecological and hydrological significance of ephemeral and intermittent streams in the arid and semi-arid American southwest*, US Environmental Protection Agency, Office of Research and Development.

Lubowe, J. K. (1964), Stream junction angles in the dendritic drainage pattern, *Am. J. Sci.*, *262*(3), 325-339.

MacQueen, J. (1967), Some methods for classification and analysis of multivariate observations, paper presented at Proceedings of the Fifth Berkeley Symposium on

Mathematical Statistics and Probability, Volume 1: Statistics, University of California Press, Berkeley, Calif., 1967.

Madani, K., and M. Hooshyar (2014), A game theory–reinforcement learning (GT–RL) method to develop optimal operation policies for multi-operator reservoir systems, *Journal of Hydrology*, *519*, 732-742.

Madani, K., M. Hooshyar, S. Khatami, A. Alaeipour, and A. Moeini (2014), Nash-reinforcement learning (N-RL) for developing coordination strategies in non-transferable utility games, paper presented at Systems, Man and Cybernetics (SMC), 2014 IEEE International Conference on, IEEE.

Madduma Bandara, C. M. (1974), Drainage density and effective precipitation, *Journal of Hydrology*, *21*(2), 187-190.

Magirl, C. S., R. H. Webb, and P. G. Griffiths (2005), Changes in the water surface profile of the Colorado River in Grand Canyon, Arizona, between 1923 and 2000, *Water resources research*, *41*(5), doi: 10.1029/2003wr002519

Mallat, S. G. (1989), A theory for multiresolution signal decomposition: the wavelet representation, *Pattern Analysis and Machine Intelligence, IEEE Transactions on*, *11*(7), 674-693.

Mallet, C., and F. Bretar (2009), Full-waveform topographic lidar: State-of-the-art, *ISPRS Journal of photogrammetry and remote sensing*, *64*(1), 1-16, doi: 10.1016/j.isprsjprs.2008.09.007

Mann, H. B. (1945), Nonparametric Tests Against Trend, *Econometrica*, *13*(3), 245-259.

Marks, K., and P. Bates (2000), Integration of high-resolution topographic data with floodplain flow models, *Hydrological Processes*, *14*(11-12), 2109-2122, doi: 10.1002/1099-1085(20000815/30)14:11/12<2109::aid-hyp58>3.3.co;2-t

McFeeters, S. (1996), The use of the Normalized Difference Water Index (NDWI) in the delineation of open water features, *International journal of remote sensing*, *17*(7), 1425-1432, doi: 10.1080/01431169608948714

McGuire, L. A., J. D. Pelletier, and J. J. Roering (2014), Development of topographic asymmetry: Insights from dated cinder cones in the western United States, *Journal of Geophysical Research: Earth Surface*, *119*(8), 1725-1750, doi: 10.1002/2014jf003081.

McVicar, T. R., M. L. Roderick, R. J. Donohue, L. T. Li, T. G. Van Niel, A. Thomas, J. Grieser, D. Jhajharia, Y. Himri, and N. M. Mahowald (2012), Global review and synthesis of trends in observed terrestrial near-surface wind speeds: Implications for evaporation, *Journal of Hydrology*, *416*, 182-205.

Meinzer, O. E. (1923), Outline of ground-water hydrology, with definitions, US Govt. Print. Off.

Melton, M. A. (1957), An analysis of the relations among elements of climate, surface properties, and geomorphology, edited, Columbia University, Department of Geology, New York.

Mitasova, H., and J. Hofierka (1993), Interpolation by regularized spline with tension: II. Application to terrain modeling and surface geometry analysis, *Mathematical Geology*, *25*(6), 657-669.

Moglen, G. E., E. A. B. Eltahir, and R. L. Bras (1998), On the sensitivity of drainage density to climate change, *Water Resources Research*, *34*(4), 855-862.

Montgomery, D. R., and W. E. Dietrich (1988), Where do channels begin?, *Nature*, *336*(6196), 232-234.

Montgomery, D. R., and W. E. Dietrich (1989), Source areas, drainage density, and channel initiation, *Water Resources Research*, *25*(8), 1907-1918, doi: 10.1029/WR025i008p01907.

Montgomery, D. R., and W. E. Dietrich (1992), Channel initiation and the problem of landscape scale, *Science*, *255*(5046), 826.

Montgomery, D. R., and E. Foufoula-Georgiou (1993), Channel network source representation using digital elevation models, *Water Resources Research*, *29*(12), 3925-3934.

Moon, T. K. (1996a), The expectation-maximization algorithm, *Signal processing magazine, IEEE*, *13*(6), 47-60, doi: 10.1109/79.543975

Moon, T. K. (1996b), The expectation-maximization algorithm, *IEEE Signal Processing Mag.*, *13*(6), 47-60.

Morgan, R. (1972), Observations on factors affecting the behaviour of a first-order stream, *Transactions of the Institute of British Geographers*, 171-185, doi: 10.2307/621547

Morisawa, M. (1957), Accuracy of determination of stream lengths from topographic maps, *Eos, Transactions American Geophysical Union*, *38*(1), 86-88.

Mutzner, R., E. Bertuzzo, P. Tarolli, S. V. Weijs, L. Nicotina, S. Ceola, N. Tomasic, I. Rodriguez-Iturbe, M. B. Parlange, and A. Rinaldo (2013), Geomorphic signatures on Brutsaert base flow recession analysis, *Water Resources Research*, *49*(9), 5462-5472.

O'Callaghan, J. F., and D. M. Mark (1984a), The extraction of drainage networks from digital elevation data, *Comput. Vision Graphics Image Process.*, *28*(3), 323-344.

O'Callaghan, J. F., and D. M. Mark (1984b), The extraction of drainage networks from digital elevation data, *Computer Vision, Graphics, and Image Processing*, *28*(3), 323-344, doi: http://dx.doi.org/10.1016/S0734-189X(84)80011-0.

Orlandini, S., and G. Moretti (2009), Determination of surface flow paths from gridded elevation data, *Water resources research*, *45*(3), doi: 10.1029/2008wr007099

Orlandini, S., P. Tarolli, G. Moretti, and G. Dalla Fontana (2011), On the prediction of channel heads in a complex alpine terrain using gridded elevation data, *Water Resources Research*, *47*(2), W02538, doi: 10.1029/2010WR009648.

Otsu, N. (1975), A threshold selection method from gray-level histograms, *Automatica*, *11*(285-296), 23-27.

Passalacqua, P., and E. Foufoula-Georgiou (2015), Comment on "Objective extraction of channel heads from high-resolution topographic data" by Fiona J. Clubb et al, *Water Resources Research*, *51*(2), 1372-1376, doi: 10.1002/2014WR016412.

Passalacqua, P., P. Tarolli, and E. Foufoula‐Georgiou (2010a), Testing space‐scale methodologies for automatic geomorphic feature extraction from lidar in a complex mountainous landscape, *Water resources research*, *46*(11).

Passalacqua, P., P. Belmont, and E. Foufoula‐Georgiou (2012), Automatic geomorphic feature extraction from lidar in flat and engineered landscapes, *Water Resources Research*, *48*(3).

Passalacqua, P., T. Do Trung, E. Foufoula-Georgiou, G. Sapiro, and W. E. Dietrich (2010b), A geometric framework for channel network extraction from lidar: Nonlinear diffusion and geodesic paths, *Journal of Geophysical Research: Earth Surface*, *115*(F1), F01002, doi: 10.1029/2009JF001254.

Peckham, S. D. (1995), Self-similarity in the three-dimensional geometry and dynamics of large river basins, University of Colorado.

Pelletier, J. D. (2013), A robust, two-parameter method for the extraction of drainage networks from high-resolution digital elevation models (DEMs): Evaluation using synthetic and real-world DEMs, *Water Resources Research*, *49*(1), 75-89, doi: 10.1029/2012WR012452.

Pelletier, J. D., and D. L. Turcotte (2000), Shapes of river networks and leaves: are they statistically similar?, *Phil. Trans. R. Soc. B*, *355*(1394), 307-311.

Perona, P., and J. Malik (1990), Scale-space and edge detection using anisotropic diffusion, *Pattern Analysis and Machine Intelligence, IEEE Transactions on*, *12*(7), 629-639, doi: 10.1109/34.56205.

Perona, P., T. Shiota, and J. Malik (1994), Anisotropic diffusion, in *Geometry-driven diffusion in computer vision*, edited, pp. 73-92, Springer, doi: 10.1007/978-94-017-1699-4

Perron, J. T., P. W. Richardson, K. L. Ferrier, and M. Lapôtre (2012), The root of branching river networks, *Nature*, *492*(7427), 100-103.

Pethick, J. (1975), A note on the drainage density-basin area relationship, *In: Area, Institute of British Geographers*, *7*(3).

Petroff, A. P., O. Devauchelle, H. Seybold, and D. H. Rothman (2013), Bifurcation dynamics of natural drainage networks, *Phil. Trans. R. Soc. A*, *371*(2004), 20120365.

Press, W. H., S. A. Teukolsky, W. T. Vetterling, and B. P. Flannery (2007), *Numerical Recipes 3rd Edition: The Art of Scientific Computing*, 1256 pp., Cambridge University Press.

Priestley, C., and R. Taylor (1972), On the assessment of surface heat flux and evaporation using large-scale parameters, *Monthly weather review*, *100*(2), 81-92.

Qin, C., A. X. Zhu, T. Pei, B. Li, C. Zhou, and L. Yang (2007), An adaptive approach to selecting a flow ‐ partition exponent for a multiple ‐ flow ‐ direction algorithm, *International Journal of Geographical Information Science*, *21*(4), 443-458.

Quinn, P., K. Beven, P. Chevallier, and O. Planchon (1991), The prediction of hillslope flow paths for distributed hydrological modelling using digital terrain models, *Hydrological processes*, *5*(1), 59-79.

Rasmussen, C. E. (1999), The infinite Gaussian mixture model, paper presented at NIPS.

Richards, K. S. (1978), Yet more notes on the drainage density-basin area relationship, *Area*, *10*(5), 344-348.

Rigon, R., A. Rinaldo, I. Rodriguez-Iturbe, R. L. Bras, and E. Ijjasz-Vasquez (1993), Optimal channel networks: A framework for the study of river basin morphology, *Water Resour. Res.*, *29*(6), 1635-1646.

Rinaldo, A., A. Marani, and R. Rigon (1991), Geomorphological dispersion, *Water Resources Research*, *27*(4), 513-525.

Rinaldo, A., R. Rigon, J. R. Banavar, A. Maritan, and I. Rodriguez-Iturbe (2014), Evolution and selection of river networks: Statics, dynamics, and complexity, *Proc. Natl. Acad. Sci. U.S.A.*, *111*(7), 2417-2424.

Rinaldo, A., I. Rodriguez‐Iturbe, R. Rigon, R. L. Bras, E. Ijjasz‐Vasquez, and A. Marani (1992), Minimum energy and fractal structures of drainage networks, *Water Resour. Res.*, *28*(9), 2183-2195.

Roberts, M. C., and O. Archibold (1978), Variation of drainage density in a small british columbia watershed, edited, Wiley Online Library.

Rodriguez-Iturbe, I., R. Muneepeerakul, E. Bertuzzo, S. A. Levin, and A. Rinaldo (2009), River networks as ecological corridors: A complex systems perspective for integrating hydrologic, geomorphologic, and ecologic dynamics, *Water Resources Research*, *45*(1).

Rodríguez-Iturbe, I., and A. Rinaldo (2001), *Fractal river basins: chance and self-organization*, Cambridge University Press, Cambridge, England.

Rodriguez‐Iturbe, I., A. Rinaldo, R. Rigon, R. L. Bras, E. Ijjasz‐Vasquez, and A. Marani (1992), Fractal structures as least energy patterns: The case of river networks, *Geophys. Res. Lett.*, *19*(9), 889-892.

Rodríguez‐Iturbe, I., A. Rinaldo, R. Rigon, R. L. Bras, A. Marani, and E. Ijjász‐Vásquez (1992), Energy dissipation, runoff production, and the three‐dimensional structure of river basins, *Water Resour. Res.*, *28*(4), 1095-1103.

Roy, A. G. (1983), Optimal Angular Geometry Models of River Branching, *Geogr. Anal.*, *15*(2), 87-96.

Sangireddy, H., C. P. Stark, A. Kladzyk, and P. Passalacqua (2016a), GeoNet: An open source software for the automatic and objective extraction of channel heads, channel network, and channel morphology from high resolution topography data, *Environmental Modelling & Software*, *83*, 58-73, doi: http://dx.doi.org/10.1016/j.envsoft.2016.04.026.

Sangireddy, H., R. A. Carothers, C. P. Stark, and P. Passalacqua (2016b), Controls of climate, topography, vegetation, and lithology on drainage density extracted from high resolution topography data, *Journal of Hydrology*, *537*, 271-282.

Sankarasubramanian, A., and R. M. Vogel (2002), Comment on the paper: "Basin hydrologic response relations to distributed physiographic descriptors and climate", *Journal of Hydrology*, *263*(1), 257-261.

Schneider, W. J. (1961), A note on the accuracy of drainage densities computed from topographic maps, *Journal of Geophysical Research*, *66*(10), 3617-3618.

Schumm, S. A. (1956), Evolution of drainage systems and slopes in badlands at Perth Amboy, New Jersey, *Geological society of America bulletin*, *67*(5), 597-646.

Singh, A., L. Reinhardt, and E. Foufoula-Georgiou (2015), Landscape reorganization under changing climatic forcing: Results from an experimental landscape, *Water Resour. Res.*, *51*(6), 4320-4337.

Smeeckaert, J., C. Mallet, N. David, N. Chehata, and A. Ferraz (2013), Large-scale classification of water areas using airborne topographic lidar data, *Remote Sensing of Environment*, *138*, 134-148, doi: 10.1016/j.rse.2013.07.004

Smith, T. R., and F. P. Bretherton (1972), Stability and the conservation of mass in drainage basin evolution, *Water Resour. Res.*, *8*(6), 1506-1529.

Smyth, P. (2000), Model selection for probabilistic clustering using cross-validated likelihood, *Statistics and Computing*, *10*(1), 63-72, doi: 10.1049/iet-spr.2009.0235

Sofia, G., P. Tarolli, F. Cazorzi, and G. Dalla Fontana (2011), An objective approach for feature extraction: distribution analysis and statistical descriptors for scale choice and channel network identification, *Hydrol. Earth Syst. Sci.*, *15*(5), 1387-1402, doi: 10.5194/hess-15-1387-2011.

Stanley, E. H., S. G. Fisher, and N. B. Grimm (1997), Ecosystem expansion and contraction in streams, *BioScience*, 427-435, doi: 10.2307/1313058

Stoker, J. M., S. K. Greenlee, D. B. Gesch, and J. C. Menig (2006), CLICK: The new USGS center for lidar information coordination and knowledge, *Photogrammetric Engineering and Remote Sensing*, *72*(6), 613-616.

Strahler, A. N. (1953), Revisions of Horton's quantitative factors in erosional terrain, *Trans. Am. Geophys. Union*, *34*, 345.

Suzuki, K., I. Horiba, and N. Sugie (2003), Linear-time connected-component labeling based on sequential local operations, *Computer Vision and Image Understanding*, *89*(1), 1-23.

Tarboton, D. G. (1997a), A new method for the determination of flow directions and upslope areas in grid digital elevation models, *Water Resour. Res.*, *33*(2), 309-319.

Tarboton, D. G. (1997b), A new method for the determination of flow directions and upslope areas in grid digital elevation models, *Water Resources Research*, *33*(2), 309-319, doi: 10.1029/96WR03137.

Tarboton, D. G., R. L. Bras, and I. Rodriguez-Iturbe (1991), On the extraction of channel networks from digital elevation data, *Hydrological Processes*, *5*(1), 81-100, doi: 10.1002/hyp.3360050107.

Tarboton, D. G., R. L. Bras, and I. Rodriguez-Iturbe (1992), A physical basis for drainage density, *Geomorphology*, *5*(1), 59-76, doi: http://dx.doi.org/10.1016/0169-555X(92)90058-V.

Tarolli, P., and G. Dalla Fontana (2009), Hillslope-to-valley transition morphology: New opportunities from high resolution DTMs, *Geomorphology*, *113*(1–2), 47-56, doi: http://dx.doi.org/10.1016/j.geomorph.2009.02.006.

Taylor, A. H., and R. M. Beaty (2005), Climatic influences on fire regimes in the northern Sierra Nevada mountains, Lake Tahoe Basin, Nevada, USA, *Journal of Biogeography*, *32*(3), 425-438, doi: 10.1111/j.1365-2699.2004.01208.x

Thornthwaite, C. W. (1931), The climates of North America: according to a new classification, *Geographical Review*, 633-655.

Voepel, H., B. Ruddell, R. Schumer, P. A. Troch, P. D. Brooks, A. Neal, M. Durcik, and M. Sivapalan (2011), Quantifying the role of climate and landscape characteristics on hydrologic partitioning and vegetation response, *Water Resources Research*, *47*(10).

Wang, D., and M. Hejazi (2011), Quantifying the relative contribution of the climate and direct human impacts on mean annual streamflow in the contiguous United States, *Water Resources Research*, *47*(10).

Wang, D., and L. Wu (2013a), Similarity of climate control on base flow and perennial stream density in the Budyko framework, *Hydrol. Earth Syst. Sci.*, *17*(1), 315-324, doi: 10.5194/hess-17-315-2013

Wang, D., and L. Wu (2013b), Similarity of climate control on base flow and perennial stream density in the Budyko framework, *Hydrology and Earth System Sciences*, *17*(1), 315-324.

Weickert, J. (1997), A review of nonlinear diffusion filtering, paper presented at International Conference on Scale-Space Theories in Computer Vision, Springer.

Weickert, J., and B. Benhamouda (1997), A semidiscrete nonlinear scale-space theory and its relation to the Perona—Malik paradox, in *Advances in computer vision*, edited, pp. 1-10, Springer.

Wigington, P., T. Moser, and D. Lindeman (2005), Stream network expansion: a riparian water quality factor, *Hydrological Processes*, *19*(8), 1715-1721, doi: 10.1002/hyp.5866

Willgoose, G., R. L. Bras, and I. Rodriguez‐Iturbe (1991), A coupled channel network growth and hillslope evolution model: 1. Theory, *Water Resources Research*, *27*(7), 1671-1684.

Wolfe, W., and G. Zissis (1985), The infrared handbook: , Environmental research institute of Michigan for the ofilce of naval research, department of the Navy, Washington, DC.

Work Jr, E. A., and D. S. Gilmer (1976), Utilization of satellite data for inventorying prairie ponds and lakes, *Photogrammetric Engineering and Remote Sensing*, *42*(5).

Wu, H., C. Liu, Y. Zhang, W. Sun, and W. Li (2013), Building a water feature extraction model by integrating aerial image and lidar point clouds, *International journal of remote sensing*, *34*(21), 7691-7705, doi: 10.1080/01431161.2013.823674.

Xu, H. (2006), Modification of normalised difference water index (NDWI) to enhance open water features in remotely sensed imagery, *International Journal of Remote Sensing*, *27*(14), 3025-3033, doi: 10.1080/01431160600589179.

Yang, C. T., and C. Song (1979), Theory of minimum rate of energy dissipation, *J. Hydraul. Eng.*, *105*(7), 769-784.

Yokoyama, R., M. Shirasawa, and R. J. Pike (2002), Visualizing topography by openness: a new application of image processing to digital elevation models, *Photogrammetric engineering and remote sensing*, *68*(3), 257-266.

Zhang, K., J. S. Kimball, R. R. Nemani, and S. W. Running (2010), A continuous satellite ‐ derived global record of land surface evapotranspiration from 1983 to 2006, *Water Resources Research*, *46*(9).

Zimmer, M. A., S. W. Bailey, K. J. McGuire, and T. D. Bullen (2013), Fine scale variations of surface water chemistry in an ephemeral to perennial drainage network, *Hydrological Processes*, *27*(24), 3438-3451, doi: 10.1002/hyp.9449.